5-2017

Sensitivity of VVER-1000 Spent Fuel Pin Nuclide Inventory to Operational Parameters

Nicholas Patrick Luciano
University of Tennessee, Knoxville, nluciano@vols.utk.edu

To the Graduate Council:

I am submitting herewith a dissertation written by Nicholas Patrick Luciano entitled "Sensitivity of VVER-1000 Spent Fuel Pin Nuclide Inventory to Operational Parameters." I have examined the final electronic copy of this dissertation for form and content and recommend that it be accepted in partial fulfillment of the requirements for the degree of Doctor of Philosophy, with a major in Nuclear Engineering.

G. Ivan Maldonado, Major Professor

We have read this dissertation and recommend its acceptance:

Ondej Chvala, Steve Skutnik, Anthony Mezzacappa

Accepted for the Council:
Dixie L. Thompson

Vice Provost and Dean of the Graduate School

(Original signatures are on file with official student records.)

Sensitivity of VVER-1000 Spent Fuel Pin Nuclide Inventory to Operational Parameters

A Dissertation Presented for the

Doctor of Philosophy

Degree

The University of Tennessee, Knoxville

Nicholas Patrick Luciano

May 2017

Dedication

For my family.

Acknowledgments

This work was supported by many.

First, I must thank my wife Jennifer Niedziela, without whom this would not have been possible. Jen, I love you and I will never be able thank you enough. To our kids, thank you for helping me appreciate the simplest moments in life.

To Mom, Dad, Jessi and Dustin, thank you for always supporting me. I hope always to be there for you.

Thanks to Dr. Maldonado, whose endless optimism and positivity has set an example for me. Thank you also for your guidance, insight, and wisdom.

Thanks to all the organizations and individuals who provided financial support for me during my graduate studies, including the University of Tennessee, Oak Ridge National Laboratory (ORNL), B&W mPower.

Abstract

Tools that can rapidly compute the isotopic composition of spent nuclear fuel (SNF) are useful for many reasons, including safety and security. Although tools exist to compute approximate isotopic compositions, detailed fuel composition requires reactor simulation that result from normal and off-normal operations. Reactor simulation is typically performed using nodal core simulators. These codes perform their calculations rapidly, but they may not compute isotopic composition.

The Russian designed VVER is a pressurized water reactor that uses hexagonal fuel assemblies with triangularly pitched fuel rods and annular pellets. The international expansion of VVER-1000 reactor technology has motivated a renewed interest in modeling and simulation of these reactors. One source for this operational data is a benchmark proposal of a Ukrainian nuclear power plant. This benchmark has served as a basis for development for improving modeling of the isotopic composition of SNF.

The objective of this work was to extend and improve depletion capabilities of NESTLE, a nodal core simulator, to accurately describe the nuclide inventory of SNF at the assembly and pin level using a hybrid macroscopic and microscopic depletion model. These isotopic inventories were verified by code to code comparison where possible. With these improved capabilities, an exploration of the detailed pin-level isotopic inventory to variations in operational parameters is enabled. This advance provides a powerful tool to assess the impact of excursions in operational conditions on the detailed SNF inventories.

Table of Contents

List of Tables

List of Figures

List of Abbreviations

ADF assembly discontinuity factor

API Application Program Interface

AER Atomic Energy Research

BOC beginning of cycle

BWR boiling water reactor

CASL Consortium for the Advanced Simulation of Light Water Reactors

CDF corner point discontinuity factor

CE continuous energy

DOE Department of Energy

EFPD effective full power day

ENDF evaluated nuclear data file

EOC end of cycle

EPRI Energy Power Research Institute

HEM homogenous equilibrium model

INL Idaho National Laboratory

ISFSI Independent spent fuel storage installation

LWR Light Water Reactor

NEM nodal expansion method

NEWT New ESC-based Weighting Transport

NEA Nuclear Energy Agency

NRC Nuclear Regulatory Commission

OECD Organization for Economic Cooperation and Development

ORNL Oak Ridge National Laboratory

PIE post irradiation examination

PPR pin power reconstruction

PWR pressurized water reactor

RMS root mean squared

SFCOMPO Spent Fuel Isotopic Composition Database

SNF spent nuclear fuel

SPND Self Powered Neutron Detetor

VVER *Vodo-Vodyanoi Energetichesky Reaktor* (Water-Moderated, Water-Cooled Power Reactor)

Chapter 1

Introduction

1.1 Spent Nuclear Fuel Analysis

The nuclide inventory of SNF is interesting for reasons of security, safety, and as a tool to validate methods of calculation. Nuclides of interest from SNF depend on the application. The safe storage and transportation of spent nuclear fuel is primarily dependent on shielding the radiation due to fission products. Criticality and heat dissipation are also safety concerns, driven by the presence of actinides and fission products. Security issues are focused on the accountancy of fissile material, but other radionuclides affect the desirability and detectability of the material. Validation of nuclear computer codes against real measurements is essential for understanding the utility and shortcomings of these codes. For these reasons and others, spent fuel is occasionally examined and the nuclide inventory is measured.

The state-owned nuclear-energy company, Rosatom, is quickly expanding the VVER-1000/1200 reactor technology with 9 reactors under construction in Russia and 29 reactors in various stages of planning and construction in more than a dozen countries. Over two-dozen VVER-1000 reactors are operational in Russia, Ukraine, Bulgaria, the Czech Republic, and China (2). A VVER-1000 unit was also recently commissioned in Iran, with additional units planned. Consequently, there is growing

interest by safeguards and nuclear non-proliferation agencies in the accurate modeling and simulation of these reactors and the fuel compositions that result from normal and off-normal operations, and in experimental validation of VVER-1000 spent nuclear fuel isotopic inventory calculations (3).

After its use in reactor cores, nuclear fuel cools for several years in a storage pool, after which post irradiation examination (PIE) can occur. PIE is a generic term that may include visual inspection, active and passive non-destructive examination using particle detectors, and destructive examination for isotopic analysis. Although difficult and expensive to conduct, destructive examination offers the most precise measurements of the nuclide composition of SNF.

1.1.1 Spent Nuclear Fuel Case Study: North Anna

It is worth considering a recent example where Light Water Reactor (LWR) SNF pins were selected for post-irradiation examination. The High Burnup Spent Fuel Data Project is a joint effort between the U.S. Department of Energy (DOE), Energy Power Research Institute (EPRI) and the Nuclear Regulatory Commission (NRC). The project seeks to understand potential degradation mechanisms that can affect SNF during storage and transport. Under the project, 32 high burnup SNF assemblies were loaded into a storage cask at the North Anna Nuclear Power Station Independent spent fuel storage installation (ISFSI), where temperatures and gas samples will be monitored. In addition, 25 similar fuel rods ("sister rods") were selected and shipped to the Oak Ridge National Laboratory (ORNL) where they will be examined and tested. The sister rods will be used to establish a baseline of data to which the ISFSI stored assemblies can be compared(4).

Many computations were performed prior to selecting the rods. Assemblies were modeled using SCALE TRITON under single-assembly (reflected boundary) conditions at several axial locations. These calculations did not account for the core effects present due to neighboring assemblies or other core-wide effects such as

flux tilts. The primary purpose of these calculations was to generate multi-group flux-weighted cross section libraries that could be used with the ORIGEN nuclide evolution code. Pin powers, as calculated by the North Anna plant computer, were input using the ORIGAMI interface, and the fuel pin depletions were calculated using ORIGEN (5).

Although calculations informed the rod selection decisions, engineering judgment ultimately determined which 25 rods were chosen. One issue with relying exclusively on the calculations was that the available operating data was limited; the assembly powers were known, but the axial powers were not. Other restrictions were due to practical limitations, such as the plant operators claim that assemblies located at the core periphery were unavailable. Some pin locations within an assembly were inaccessible because of mechanical restrictions, like the inability to remove the top nozzle. Pin selection was driven by primarily by concerns and interests of the project, specifically the examination of the structurally weakest pins. Pin-type variety was also a consideration. Pins of multiple fuel manufacturers were considered, as were pins that used one of four cladding types. In some cases, pins near guide tubes or burnable poison rods were selected and so were corresponding pins with similar burnup away from those locations. Because the primary purpose of the project is to determine the pins' mechanical properties under storage and transport conditions, no isotopic analyses of the used fuel are currently planned(6).

1.2 Problem Statement

To improve the calculation of the nuclide inventory of VVER-1000 spent nuclear fuel for security purposes, and in advanced preparation of a proposal to connect plant operational data with post irradiation examination measurements, an advanced depletion tool is proposed to study the sensitivity of spent VVER-1000 fuel nuclides to operational parameters over multiple fueling cycles. To achieve this goal, the following major milestones have been accomplished in this work:

- Model the first cycle of the AER VVER-1000 Benchmark including improved core reflector models
- Extend NESTLE's microscopic depletion capabilities
- Verify NESTLE results using a Monte Carlo calculation
- Calculate sensitivity of spent fuel nuclide inventory

Chapter 2 briefly reviews the techniques and codes used in this work. Chapter 3 presents the VVER-1000 reactor, including design, assembly construction, and available benchmark data. Chapter 3 also presents the results of extensive whole core modeling of the VVER-1000 to access pin level isotopics subject to variations in operational parameters. The modeling work included construction of a one-twelth symmetric core Monte Carlo model of the VVER-1000 reactor, NESTLE nodal core analysis using macroscopic cross sections, and an improved NESTLE microscopic cross section model to analyze fuel isotopics at the assembly level. Chapter 4 discusses the implementation of microscopic depletion in NESTLE, including extensions and improvements needed to accurately describe the nuclide inventory of SNF at the assembly and pin level. Chapter 5 discusses the implementation and verification of pin power reconstruction methods used in NESTLE, including benchmarking of the pin-power reconstruction methods against industry codes, and a study of these quantities on the VVER-1000. Chapter 5 also presents a discussion on the impact of precision errors to computing relevant pin power reconstruction (PPR) values. Chapter 6 develops a small Python code to perform a previously proposed methodology in order to improve calculation of discontinuity factors in the reactor reflectors. Chapter 6 also include several two dimensional models of test assemblies, and a study of impact of the two-dimensional discontinuity factors on the VVER-1000 reactor core model. Chapter 7 presents pin-level isotopic information obtained from realistic variation in operational parameters of the VVER-1000 core.

Chapter 2

Methods and Codes

2.1 Methods

The term *approximation* may have a negative connotation; the implication being that an approximate thing is somehow deficient or less than fully legitimate. But in truth, most useful insights in mathematics and physics are due to approximations. Approximations are a segregation of the strongest influences from the weakest, which allows the application of new techniques to otherwise intractable problems. When approximations work well, they enable faster and more accurate solutions. But when they fail, they can do so silently, giving little indication to their employers that they have contradicted their own assumptions. All approximations have an associated error, which will be unacceptably large under some set of conditions. Therefore, despite their utility, all approximations *must* eventually fail under some conditions. In nuclear reactor core analysis, the limitations of approximations are often described as *effects*. As several of these effects arise in the work proposed here, they are briefly described in the following sections.

2.1.1 Two-Step Procedure for Reactor Analysis

Nuclear reactor core analysis typically uses a collection of approximations in a process known as the *two-step procedure*. The two-step procedure couples detailed flux calculations in a limited region with more approximate flux calculations over a larger region. The detailed flux calculations account for spatial and energy heterogeneities on the fine scale, while the more approximate flux calculation is used on a coarse scale. To couple the fine scale to the coarse scale, the energy details of the cross sections are collapsed or condensed, and the geometric details across the region are homogenized. The lattice physics calculation occurs on the fine scale and accounts for the fuel pin heterogeneity, and the core physics calculation occurs on the coarse scale and accounts for the fuel assembly heterogeneity. By separating the problem into fine and coarse scales, the two-step procedure allows reasonably accurate analysis to be conducted quickly. It also allows the core geometry to be reconfigured without again performing the lattice calculation, which is especially important during core design when a search may explore many thousands of core configurations to find an optimal one.

The two-step procedure uses mulitgroup cross sections. Multigroup cross sections are formed by weighting the continuous energy cross sections with a flux spectrum. The *true* flux spectrum is actually one of the results of the calculation and is not known *a priori*. Therefore an approximate flux spectrum is assumed or calculated. This method is acceptable only if the final calculated flux spectrum is consistent with the assumed flux spectrum. When this assumption is violated, the result may include *spectral effects*.

Thermal Effects

Further approximations that simplify the core conditions also occur often during calculations. Conditions that are usually not known *a priori* are the temperatures, which can have a significant effect on the cross sections, the influence of neighboring

homogenized regions, which can have a significant effect on the flux, and the presence or absence of absorbing control rods and/or soluble poisons, which affect both the flux and the cross sections.

Thermal effects, including the cross section dependence on the fuel temperature and coolant temperature and density, are coupled to the heat produced in the fuel, which is itself coupled to the flux solution. To solve this coupled problem, an iterative technique may be employed where the cross sections at many various thermal conditions must be evaluated while converging to a solution. Solving exactly for these cross sections would require time consuming repetitions of the lattice physics calculation, so it is assumed that the cross section for any thermal condition can be approximated by functionalizing of a small number of cases or branches. The functionalization assumption is valid when the change in the cross section is relatively small. In other words, each branch case is a perturbation on the base case. Branch cases can be computed beforehand and in parallel such that they do not contribute significantly to the overall calculation wall clock time. If the core thermal conditions are indifferent to the core configuration (for example, when the power is so low that it causes no significant change in temperatures and densities), then no thermal approximation is required, and the need to calculate branch cases is eliminated.

Neighbor Effects

The influence of neighboring regions in the core, called the *neighbor effect*, can affect the flux spectrum of a homogenized region. Although the energy-group dependent flux by region is a major result of the core calculation, this calculation is predicated on cross sections that were homogenized with flux spectra from the lattice physics calculations. The homogenization process weights the group cross sections by the group fluxes. Therefore, validity of the cross sections is based on the assumption that the flux spectrum in a core region is not significantly different from the lattice flux spectrum. The neighbor effect can be large enough to violate this assumption. To mitigate the neighbor effect, cross sections can be homogenized with differing

adjacent regions present in a configuration called a *color set*. Lines of symmetry typically present within fuel lattice designs make good reflective boundary candidates for color set calculations and limit the overall spatial extent required. For known core configurations, color sets work well, but in design situations computing a large number of color sets is undesirable. Like branch cases, color sets can be calculated beforehand and in parallel, reducing the additional computational time required overall for core calculations. If there is no spatial variation in the core composition (strictly only true in infinite media, but sufficiently approximate over spatial scales that are large compared to the mean free path of the neutron), then no color set calculations are required.

Shim Effects

Shim effects are due to the presence or absence of control rods and soluble poisons. Shims directly alter the homogenized composition by adding moderating and absorbing nuclides, and (in most cases) displacing other nuclides such as those in the coolant. The addition and subtraction of these nuclides have (by design) a large impact on the flux magnitude and spectrum present in a region. Shim effects, like intranodal effects, are mitigated by altering the composition present during the lattice physics calculation. This is achieved by performing additional branch cases with soluble poison and control rods present and absent. Strong shims have such a large effect that they may be no longer considered perturbations to the base case. In these situations, an entire additional set of thermal condition branch cases may be required for when the shim is present and when it is removed, effectively doubling the number of branch cases required. Shim effects are essential to boiling water reactor analysis, but they are less important to the analysis of typical pressurized water reactors.

History Effects

Yet more approximations are made when evolving the material compositions over burnup steps. Before describing these approximations, it is important to note that branch cases are computed at each burnup step, but evolution from one burnup step to the next only occurs during the base case. Each branch case cannot be time-evolved independently because the number of lattice physics calculations would increase exponentially with each burnup step. Nonetheless, material compositions *should* evolve due to the neutron flux computed in the core calculation, which may be significantly different from the base case conditions because of thermal and shim effects. While these *history effects* only manifest themselves when the core region conditions are different than the lattice conditions, they are distinct from the aforementioned effects.

To demonstrate the distinction, consider a scenario where lattice branch case functionalization accurately approximates any thermal and shim condition at each time step t and time step $t + \Delta t$. In this case, the error due to the thermal and shim effects are negligible. In contrast, the error due to the history effect may be significant if during time interval Δt the computed flux is significantly different than the base case flux. The most obvious example of a history effect is the impact on a region's composition due to the time dependence of control rod insertion. The material composition of a region with the rod inserted must be significantly different after a long time from the material composition that would result over the same time interval with the rod withdrawn. To be concise, thermal and shim effects occur because intermediate cross sections cannot be approximated accurately at time t, but history effects occur because these intermediate cross section values cannot be accurately evolved to time $t + \Delta t$, even if they have been accurately approximated at time t. One technique for mitigating history effects is to use microscopic depletion instead of macroscopic depletion.

2.1.2 Depletion

All burnup calculation methods proceed quasi-staticly over a series of discrete time-steps. Each time-step includes two parts: a neutron transport calculation, followed by an evolution (transmutation, fission, and decay) calculation. With the initial composition specified, the process begins with a neutron transport calculation to evaluate fluxes and reaction rates for the static case. These results are then used to evolve the material compositions to the next time-step. Iterations of the transport-evolution calculations continue until all the depletion time-steps have been completed. A final transport calculation may be performed if EOC neutronic evaluations are required. The hybrid macro/microscopic depletion model has been implemented in modern nodal core simulators including Studsvik's SIMULATE (1). First developed for SIMULATE-4, the model is also implemented in the latest version of the code SIMULATE-5. The model tracks approximately 50 nuclides (17 actinides, 30 fission products, and a Gd/B burnable absorber) that are important to reactivity. Microscopic cross sections are functionalized according to important instantaneous and historical effects. The gadolinium isotopes ^{155}Gd, ^{156}Gd, and ^{157}Gd have been replaced by a pseudo-isotope because of the large self-shielding of gadolinium.

The SIMULATE-4 microscopic depletion model was verified against several numerical tests. In the first numerical test, the model was compared to a 2D CASMO-4 model and a macroscopic cross section SIMULATE-4 model of a typical BWR assembly. The model had a control rod removed for the first 10 GWd/MTU, then inserted for the next 10 GWd/MTU, then removed for the final 10 GWd/MTU for a total of 30 GWd/MTU. The 2D CASMO-4 model was used as the base for comparison. The microscopic depletion model significantly reduced errors in reactivity in comparison to the macroscopic model (see Figure 2.1). The second numerical test examined the accuracy of actinide nuclide tracking. The microscopic

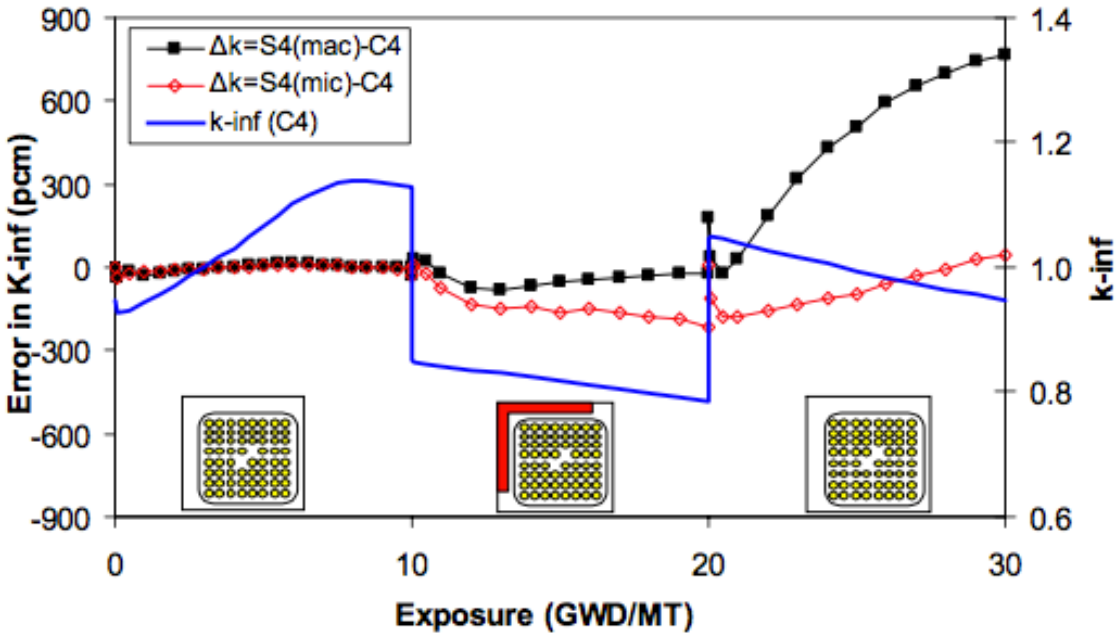

Figure 2.1: The impact of the shim and history effects on the microscopic depletion model of SIMULATE-4 from reference (1).

model was significantly more accurate compared with the macroscopic model. In the case of ^{239}Pu the macroscopic model had errors of approximately 2% and the microscopic model had errors of approximately 0.2% (see Figure 2.2).

The research and development division at Electricite de France (EDF) have also implemented a hybrid microscopic depletion model in their core code COCAGNE (7). The microscopic depletion model in COCAGNE has been used to perform improved core calculations accounting for historical effects. This model uses 20 heavy nuclides (^{234}U to ^{245}Cm) and 13 fission products, along with a pseudo-isotope that accounts for all other nuclides. A feature available in COCAGNE (also available with SIMULATE) is nodal submeshing at the pin cell level. Isotopic concentrations calculated by COCAGNE are of high quality (typically less than 0.5% as compared to the lattice code APOLLO2) because the the reconstructed pin flux is used as an input to the microscopic depletion solver.

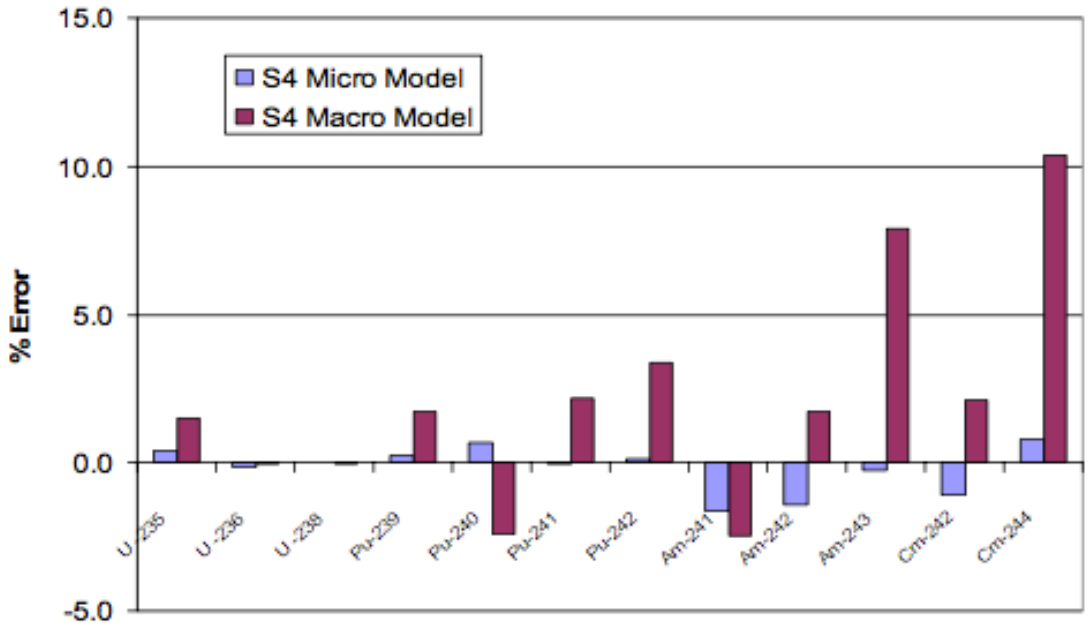

Figure 2.2: Comparison of the calculated error in nuclide concentrations using the microscopic and macroscopic depletion models in SIMULATE-4 from reference (1).

Studsvik Scandpower offers a commercial software product called *SNF* that estimates nuclide inventory with radiation and heat sources (8). This tool is used in conjunction with Studsvik's other products such as the GARDEL on-line core simulator. Comparisons with ORIGEN-ARP calculations show insignificant deviations for calculation of actinide heat sources for 100,000 years cooling time.

2.2 Codes

Several codes commonly employed in nuclear reactor modeling were used in this work. One important aspect was development of coupling mechanisms to allow output from one code to be automatically synthesized into input for other codes in the chain. Here each code and its role in the projects are briefly described.

2.2.1 KENO

The Monte Carlo code used in this work is SCALE/KENO-CE (9).This code is easily applied to analyze 2D lattice (assembly) models, which are typically evaluated using isothermal with reflective (infinite) boundary conditions.

Monte Carlo calculations are well suited to parallel computation, but codes behave differently with increased number of processors (CPUs). The scalability of a code is its ability to be computationally efficient with a greater number of processors.

SCALE, the comprehensive nuclear systems modeling and simulation suite developed at ORNL, includes the Monte Carlo code KENO-VI (10). SCALE/KENO applies a form of Doppler broadening, and a more accurate method is currently under development. It also supports time-dependent input for temperature, control rod, and boron concentration changes. KENO is capable of using either multigroup or continuous energy (CE) cross section libraries. CE cross sections use fewer approximations, and calculations that employ these libraries are usually considered reference solutions. Multigroup cross sections are more approximate, but they generally allow for faster calculations. In many applications, the results achieved with multigroup cross sections may approach the accuracy of those with CE (particularly for commercial reactors where methods for resonance cross section adjustments are well established). The primary limitation of KENO-VI is its speed. Parallel calculations with CE cross sections relatively new. In this research, multigroup libraries were used for scoping calculations, and continuous energy libraries were used for high fidelity calculations.

Within SCALE depletion sequences, KENO uses the ORIGEN code, the modern version of ORNL point depletion module that supports modern nuclear data and source methods and is used worldwide. ORIGEN uses a matrix exponential method to solve the Bateman system of equations for long-lived nuclides, and it uses analytical Bateman solutions for the short-lived nuclides. Short-lived nuclides lead to large diagonal elements in the matrix exponential, consequently ORIGEN's primary

method of solution is based on truncated Taylor series with scaling and squaring, which treats short-lived nuclides separately. The most recent release of ORIGEN (in SCALE 6.2) includes an alternative method of solution using a Chebyshev rational approximation method (CRAM) solver with similar execution times and increased numerical precision. All KENO-VI calculations were performed using continuous energy ENDF/B-VII.0 cross-section data.

2.2.2 NESTLE

NESTLE is a three-dimensional few-group diffusion core simulator that employs the nodal expansion method (NEM). First developed at North Carolina State University and in collaboration with Idaho National Laboratory (INL) and ORNL, NESTLE is currently developed and maintained at the University of Tennessee (UT), Knoxville. At UT, NESTLE has been significantly modernized and broadly applied to model a wide variety of reactors, including pressurized water reactors (PWRs), boiling water reactors (BWRs), small modular reactors, CANDU reactors, fluoride-cooled high temperature reactors, and recently the VVER (11). Used in the commercial industry for core design and optimization, diffusion codes are much faster than Monte Carlo codes. For example, NESTLE can compute a single burnup state point for the entire core in seconds as opposed to the hours or days frequently required for a comparable Monte Carlo calculation. Furthermore, NESTLE includes thermal cross section feedback effects using built-in hydrodynamic and fuel temperature models, which are generally absent in equivalent Monte Carlo calculations.

NESTLE achieves its computational speed by interpolating cross sections based on pre-computed perturbation cases (branches) generated from a lattice code based on the operating conditions of the reactor. The lattice code computes fluxes and depleted nuclide compositions accounting for heterogeneities on the fuel rod and assembly level. Lattice codes usually limit the geometric domain of the calculation by assuming identical neighboring assemblies by using reflective boundary conditions.

For each fuel lattice assembly design used in the core, a matrix of perturbation cases is computed at each depletion time step. These perturbation cases include potential variations in fuel temperature, coolant temperature, coolant density, soluble poison concentration, and rod state (in or out). NESTLE is indifferent to the lattice code used, but for this study the SCALE TRITON was used. NESTLE uses a standard cross section library interface format and can use precomputed data from many different lattice codes.

A recent developmental feature being added to the NESTLE code, which can invoke the latest version of the SCALE code's ORIGEN API module at any selected spatial region for detailed isotopic tracking, was tested in preparation for this work(12; 13). ORIGEN API is a collection of APIs and constitutes a rewrite of ORIGENs data container classes into object-oriented C++ with FORTRAN bindings, which effectively facilitates calling ORIGEN as a standalone program from within another program, such as NESTLE. Therefore, using this NESTLE depletion option, the isotopic concentrations within an individually selected fuel pin can be tracked from the beginning through the end of a cycle using the spatial and time-dependent neutronic flux and thermal-hydraulic conditions developed using the full-core 3D operational features of the NESTLE simulation. The most recent NESTLE developments have restored and improved upon capabilities implemented by Galloway (12). Specifically, NESTLE now interfaces with the modern ORIGEN API, a result of the recent major refactor to the ORIGEN code architecture (13). NESTLE is now more robust in computing depletion materials, enabling greater flexibility in the number and type of materials to be depleted. With these improvements, depletion analysis in NESTLE with ORIGEN is faster and much more seamless than in its previous implementation.

2.2.3 Lattice Physics

SCALE TRITON

For this study, the SCALE/TRITON lattice physics and depletion code was used to generate the libraries and data needed by NESTLE. SCALE/TRITON couples the 2D discrete ordinates code NEWT to perform the multigroup transport calculations and the depletion code ORIGEN to calculate the time dependent nuclide compositions. For each fuel lattice at each depletion step and for each perturbation case, the macroscopic cross sections are collapsed in energy (from 252 groups to two groups) and spatially homogenized (over the lattice region) using cross section weighting that preserves the reaction rates in the region. These two-group cross sections, along with other auxiliary data, are used as input for the NESTLE core calculations.

NEWT

Also part of the SCALE package, NEWT is a neutron transport solver, which provides two-dimensional, unstructured-mesh, discrete ordinates solution for multigroup neutron transport calculations(14).

Two significant changes to were made to the source code of the 2D transport code NEWT in SCALEv6.2b4. The first change was made so that the corner point discontinuity factor (CDF)s could be be computed for the hexagonal lattices. The second change was made so that the nuclide microscopic cross sections would be output for use as input to NESTLE.

Chapter 3

VVER-1000 Core Modeling

This chapter discusses high fidelity Monte Carlo simulations that consider the spatial- and time-dependent thermal-hydraulic features of the fuel and moderator regions of an actual VVER-1000 reactor core, and to quantify the impact of applying these operationally representative localized conditions upon the accuracy of predicted SNF isotopic inventories. High fidelity within the context of this work is defined as the combination of an accurate neutron transport solution with minimal approximations in both spatial and energy resolution, an accurate fuel depletion model that accounts for all isotopes that are generated in the fuel by reactor irradiation, plus some reasonable approach to account for local- and time-dependent thermal-hydraulic conditions, or feedback.

3.1 The VVER-1000 Reactor

The Russian designed VVER is a pressurized water reactor that uses hexagonal fuel assemblies with triangularly pitched fuel rods and annular pellets. They are hydrodynamically similar to the PWRs operated in the United States despite these differences in design. Two types of VVER power plants have been built and operated, the VVER-440 with two 220 MWe generators, and the VVER-1000 with a single 1000

MWe generator. A third generation, the VVER-1200, is currently under construction at two locations in Russsia. Although the VVER-1200 includes a slight increase in fuel length and core power, the overall core design is nearly identical to the VVER-1000.

Recent VVER-1000 experimental isotopic assay data from the Russian Balakovo-2 and -3 and Kalinin nuclear plants were compiled into the OECD/NEA benchmark database of spent nuclear fuel (3; 15). The Spent Fuel Isotopic Composition Database (SFCOMPO) database is a utility provided by the Organization for Economic Cooperation and Development (OECD)/Nuclear Energy Agency (NEA) in partnership with ORNL(16).

3.2 AER VVER-1000 Khmelnitsky-2 Benchmark

One source for VVER-1000 operational data is a collaboration between a German industrial contractor (TÜV SÜD Industrie Service GmbH) and a Ukrainian research center (State Scientific and Technical Centre for Nuclear and Radiation Safety of Ukraine). These institutions produced a series of benchmark proposals through the AER Symposia on VVER Reactor Physics and Reactor Safety. The authors, T. Lötsch, V. Khalimonchuk, and A. Kuchin, first presented the AER VVER-1000 benchmark proposal at the 2009 AER symposium proposal, and they have continued to provide corrections and updates at subsequent symposia (17; 18; 19).

The stated goal of the AER VVER-1000 benchmark project is "to estimate the range of applicability and the uncertainties of the packages of codes and data libraries used... in the framework of safety related assessments and evaluation for VVER-1000 reactors in Ukraine." Although the AER VVER-1000 benchmark documents do not explicitly state the source of the plant data, a supplementary publication (20) and private communications by T. Lötsch confirm that the design and operational details of the AER benchmark correspond to the Khmelnitsky-2 nuclear power plant in Ukraine, which began commercial operation in 2005.

The AER VVER-1000 benchmark documents describe four complete fuel loading cycles, beginning with an initial core. Starting with an initial core is useful for modeling purposes because all the fuel loaded in the core is fresh, which means that no assumptions are needed to characterize the isotopic compositions of fuel assemblies from previous cycles. Initial cores typically have a shorter cycle length and lower enrichment assemblies are used to shape the power distribution.

The AER VVER-1000 benchmark documents include detailed fuel assembly and core design information. The geometry and initial nuclide composition of fuel rods, fuel lattices, control rods, burnable absorber rods, stiffening plates, spacer grids, reflector regions, and other components are detailed in the reports. The following important plant operational data are also included in the AER VVER-1000 benchmark documents:

- Control rod bank insertion
- Operational power
- Coolant flow
- Soluble boron concentration
- Coolant inlet temperature

The actual values of those parameters are reported approximately once for each day of operation. The AER VVER-1000 benchmark includes modeling results for 2D lattice (single assembly) and core calculations. Also included are the depletion calculations of nine fuel nuclides in the lattice models. The nuclides include: ^{235}U, ^{238}U, ^{239}Pu, ^{240}Pu, ^{241}Pu, ^{155}Gd, ^{157}Gd, ^{135}Xe, and ^{149}Sm. The benchmark reports the measured and calculated critical soluble boron concentration throughout the depletion (called the boron letdown), which is a global core property useful for verifying the full core model.

3.3 VVER-1000 Modeling

In a large 3D core, the current generation of Monte Carlo neutron transport calculations can provide high accuracy flux solutions using continuous energy (CE) cross sections and explicit fuel rod geometries. An accurate depiction of the neutron flux field is fundamental for accurate isotopic depletion calculations (within the accuracy of the underlying nuclear data). While highly respected mainstream Monte Carlo codes using a continuous-energy treatment such as SCALE KENO(10), MCNP(21), and SERPENT(22; 23) all include isotopic depletion options, these codes do not automatically calculate or apply the changing thermal conditions for the fuel and moderator (thermal-hydraulic feedback) iteratively. These conditions include a continuous and broad range of spatial- and time-dependent power and temperature distributions over the course of reactor's operation. These varying temperatures in turn influence the neutron cross sections and material properties (i.e., water density) and therefore alter the flux solution and isotopic depletion. Instead, these codes are more commonly used with spatially isothermal conditions or fixed temperatures assigned to specific material regions in the models. Generally, this information must be made available from full core calculations performed by the reactor operator. However, when modeling a reactor from a non-cooperative state (or even just verifying declarations from a cooperative one), such information may not be available. The thermal-hydraulic conditions vary with time and play an important role in the evolution of nuclide compositions in a reactor fuel. Therefore, the ability of Monte Carlo to accurately represent the geometry in 3D is not sufficient because the current class of these codes does not account for the thermal-hydraulic conditions. Full-core three- dimensional (3D) detailed pin-by-pin Monte Carlo models that deplete over an entire fuel cycle (even with fixed temperatures) remain largely intractable today using typical computing resources (without tens of thousands of processors). Thus, the grand challenge of high fidelity full core modeling using realistic thermal-hydraulic

conditions and minimal assumptions continues to be a widely pursued longer-term activity. In fact, it is a focal point of high-profile US DOE sponsored research efforts such as the Consortium for the Advanced Simulation of Light Water Reactors (CASL).

Presented herein is an alternate and tractable approach to the full core modeling problem via a hybrid, deterministic/stochastic method herein developed to achieve two goals: first, to determine realistic spatial- and time- dependent thermal-hydraulic conditions of a Ukrainian VVER-1000 reactor under actual operational conditions by using the NESTLE nodal-diffusion three-dimensional (3D) simulator(11) of the type used in commercial LWR core design, and second to apply time- and assembly-averaged axial profiles of moderator and fuel temperatures to a high-fidelity MCNP 3D model of a fuel assembly to estimate the impact of temperature profiles upon the isotopic inventory of VVER-1000 fuel assemblies. Accordingly, a full-core (3D) NESTLE model of the VVER-1000 Khmelnitsky Unit 2 core was created and favorably validated against benchmark data published by the AER Symposia on VVER Reactor Physics(17; 18; 19). The NESTLE model employs pre-calculated lattice physics data from SCALE's transport-based TRITON/NEWT modules to account for localized effects on cross sections. Actual plant data (power level, control rod positions, coolant flow, and boron concentration) were input for 335 operational data points during a ten-month initial cycle. Core reactivity and the critical boron concentration were closely predicted by the NESTLE core-follow calculation, giving good indication that the computed temperatures were realistic and representative of the actual core operation (see Figure 3.7).

The AER benchmark also supplied computed reactivity and isotopic content from three lattice code suites for comparison. Thus, high fidelity Monte Carlo lattice (2D) models using KENO, MCNP with VESTA (24), and SERPENT were constructed to analyze the nuclide composition of VVER-1000 SNF. Nuclide composition results for fuel assemblies were found to be in close agreement with the benchmark reported values (see Figure 3.1). This project developed full core VVER-1000 models with Monte Carlo codes using local thermal- hydraulic conditions

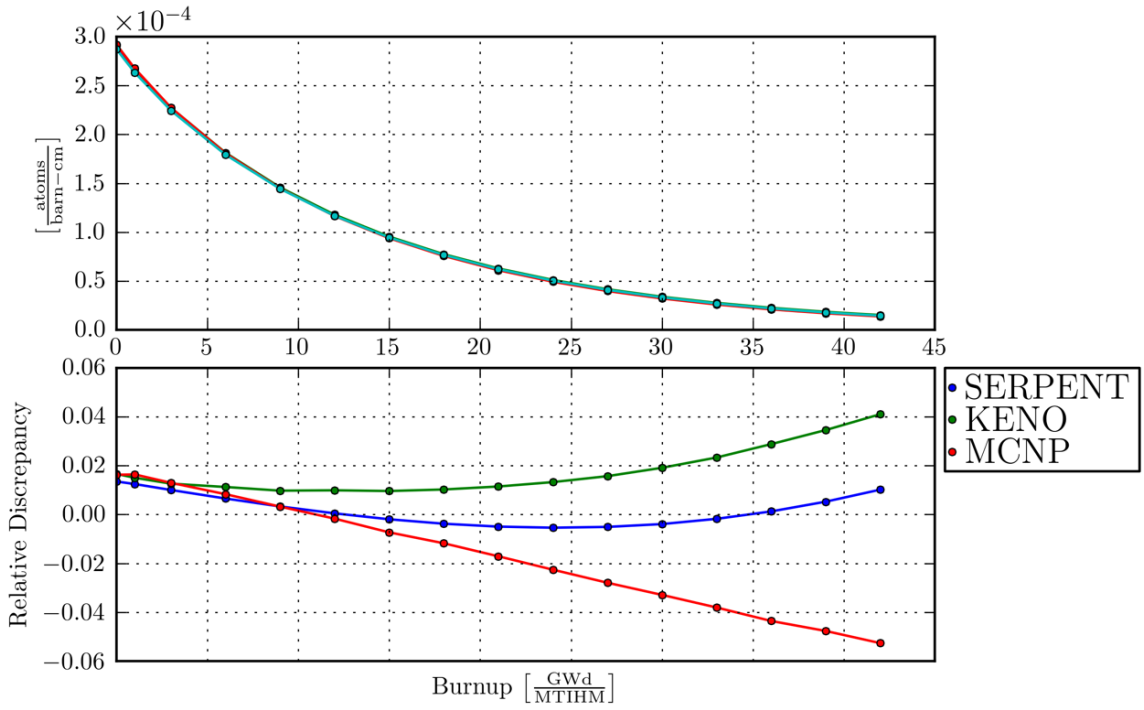

Figure 3.1: Relative discrepancies from benchmark average ^{235}U concentrations for the 13au lattice.

as determined by the NESTLE core calculations and full core depletion. However, the complexity of these models was ultimately overwhelming and impractical based on current code capabilities and typical computing resources. Computational requirements are a major impediment to perform these full-core Monte Carlo calculations. Furthermore, and more importantly, it was concluded that some of the features required to properly model localized temperatures are in large part still developmental or not yet available in currently available codes.

An alternate solution involves a recent feature that links the NESTLE code to the latest version of the ORIGEN Application Program Interface (API) to perform detailed isotopic depletion for any selected region. The ORIGEN API is available in the latest version of the SCALE version 6.2 nuclear systems analysis code package. This feature was tested in this project (12; 13). Using this NESTLE option, the isotopic concentrations were tracked within individual (or groups of) fuel pins within the same fuel assembly for comparison with MCNP assembly calculations. In this

simulation, no assumptions were made regarding the localized fuel and moderator temperatures. Thus NESTLE iteratively determined the appropriate spatial- and time-dependent thermal-hydraulic conditions that applied at each of 20 axial nodes in each of the 163 fuel assemblies in the full-core, for each of the 335 operational time steps available with the actual power, flow, control rod, and boron conditions specified by the benchmark. This calculation required an initial SCALE/TRITON depletion run that established cross section values for the selected pin within the assembly.

These results demonstrate the availability of a powerful yet tractable computational option that can be used to calculate ORIGEN-determined pin-level isotopic concentrations for an arbitrarily selected number of axial sections while at the same time accounting for the appropriate thermal-hydraulic feedback computed based on actual whole-core calculations and operational data. Consequently, continued research and development of this option is recommended for the modeling and simulation of SNF isotopic concentrations at a fuel pin level. The rest of this chapter expands on this introduction, including a summary of some of the lessons learned.

3.4 Localized Thermal-Hydraulic Conditions in Monte Carlo Calculations

Variations in fuel and coolant temperatures are typically not included in Monte Carlo-based depletion calculations, not because they are negligible, but because they require explicit thermal-hydraulic models that further compound already taxing computation requirements. Local fuel and coolant temperatures are driven by the spatially dependent specific power, and those temperatures in turn affect the neutron flux, creating a thermal feedback effect. Thermal feedback effects are calculated by solving for the flux and temperatures iteratively. For reactor core models, it is impractical to use Monte Carlo methods to compute thermal feedback directly. Many iterations are required to determine the temperatures, and Monte Carlo methods

require relatively large calculation times on the order of CPU-hours. Thus, to include thermal feedback effects for practical core analysis, fuel and coolant temperatures must be computed at this time by alternate methods.

Computation of fuel and coolant temperatures is accomplished using the NESTLE 3D nodal diffusion core simulator that includes thermal-hydraulic feedback. In contrast to Monte Carlo methods, NESTLE can solve the reactor core flux in a few CPU seconds(11). A typical nodal core simulator such as NESTLE uses few-group nodal neutron diffusion theory to quickly evaluate neutron fluxes and relative power distributions. As the flux solutions in the core approach convergence, the cross sections are updated using a thermal-hydraulic solver such as the homogenous equilibrium model (HEM), which more than adequately solves the mass, momentum, and energy equations for pressurized water reactors (PWRs) and updates fuel and moderator temperatures until these and the flux solution converge. This approach represents what is typically used to design and operate commercial nuclear reactor cores today.

A nodal core simulator can quickly evaluate neutron fluxes and material temperatures using few energy groups (typically only two for LWRs), and by averaging the depleted fuel compositions over large regions or "nodes". The nodalized configuration, which could contain assembly-sized radial regions with 20 or more axial regions, is treated with the nodal core simulator to calculate fuel and moderator temperatures with a precision that is adequate to calculate core characteristics such as thermal and reactivity margins for the purposes of reactor performance and fuel management. In order to produce more accurate nuclide compositions with a Monte Carlo neutronics and depletion model, this project investigated a hybrid approach that integrated high fidelity Monte Carlo transport codes with thermal-hydraulic properties of converged coolant and fuel temperatures from the NESTLE nodal core simulator. The underlying objective of this approach is to

apply dynamically calculated temperature distributions for any core operation from a nodal core simulator in a Monte Carlo depletion calculation to produce more accurate nuclide compositions than could be achieved by either method when used in isolation.

For this work, the SCALE/TRITON lattice physics and depletion code was used to generate the libraries and data needed by NESTLE. SCALE/TRITON couples the 2D discrete ordinates code NEWT to perform the multigroup transport calculations and the depletion code ORIGEN to calculate the time dependent nuclide compositions. For each fuel lattice at each depletion step and for each perturbation case, the macroscopic cross sections are collapsed in energy (from 238 groups to two groups) and spatially homogenized (over the lattice region) using cross section weighting that preserves the reaction rates in the region. These two-group cross sections, along with other auxiliary data, are used as input for the NESTLE core calculations.

3.5 Lattice Physics Analysis

The AER VVER-1000 Khmelnitsky-2 benchmark provided full descriptions of every individual 2D lattice (assembly) in the core, as well as computed reference lattice depletion results. Key attributes provided in the benchmark documentation for each lattice included reactivity (k_∞) trajectories and isotopic concentrations of key nuclides. This section describes the assembly calculations performed with the various Monte Carlo codes assessed in this report, and provides a comparison of the results for the AER benchmark. Furthermore, these assembly models were used by SCALE/TRITON to generate the 2- group energy-collapsed and assembly-homogenized cross section data and perturbation branches required by NESTLE.

The fuel assemblies in the AER VVER-1000 Khmelnitsky-2 benchmark are axially uniform in geometry and composition and therefore can be modeled with a single fuel lattice model. For the initial core, five assembly types are used. Common features to all assembly types are summarized in Table 3. Each assembly includes

312 UO_2 fuel pins composed of annular pellets, 18 guide tubes, and one central instrument tube, arranged on a 1.275 cm triangular pitch. Stiffening angle brackets are included at the 6 corners of the assembly. The lattice models are depleted at constant temperatures (fuel: 1005 K, other materials: 578 K), constant boron concentration (525 ppm), and constant power density (42.5 W/gU). Table 3.1 shows the assembly types used in the core for the first cycle. Fig. 3.2 shows the configuration of lattice assemblies 13au, 22au, 30av5, 39awu, and 390go.

Table 3.1: Lattice (assembly) types used in the VVER-1000 for the first cycle.

Designation	Number of Pins	Pin Enrichment (%)	Pin Gd_2O_3 (wt%)
13 au	312	1.30	0.0
22 au	312	2.20	0.0
30av5	303	2.99	0.0
39awu	243	4.0	0.0
	60	3.6	0.0
	9	3.3	5.0
390go	240	4.0	0.0
	60	3.6	0.0
	6	3.3	5.0

A single assembly can be modeled separately and used to verify the components of the larger whole core model. Single lattices are modeled by SCALE TRITION to produce macroscopic cross section data for NESTLE. The AER VVER-1000 benchmark includes calculated results for values of lattice k_∞ and nuclide compositions using three lattice codes: CASMO(25), HELIOS(26), and NESSEL. With five lattices, and nine nuclide concentrations computed using three codes, there are many data points for possible comparison in the benchmark. Results of lattice 39awu using SCALE/KENO-VI are shown in Figures 3.3 and 3.4. Lattice k_∞ and nuclide compositions were generally within 10% relative error of the AER VVER-1000 benchmark average and discrepancies were commensurate with

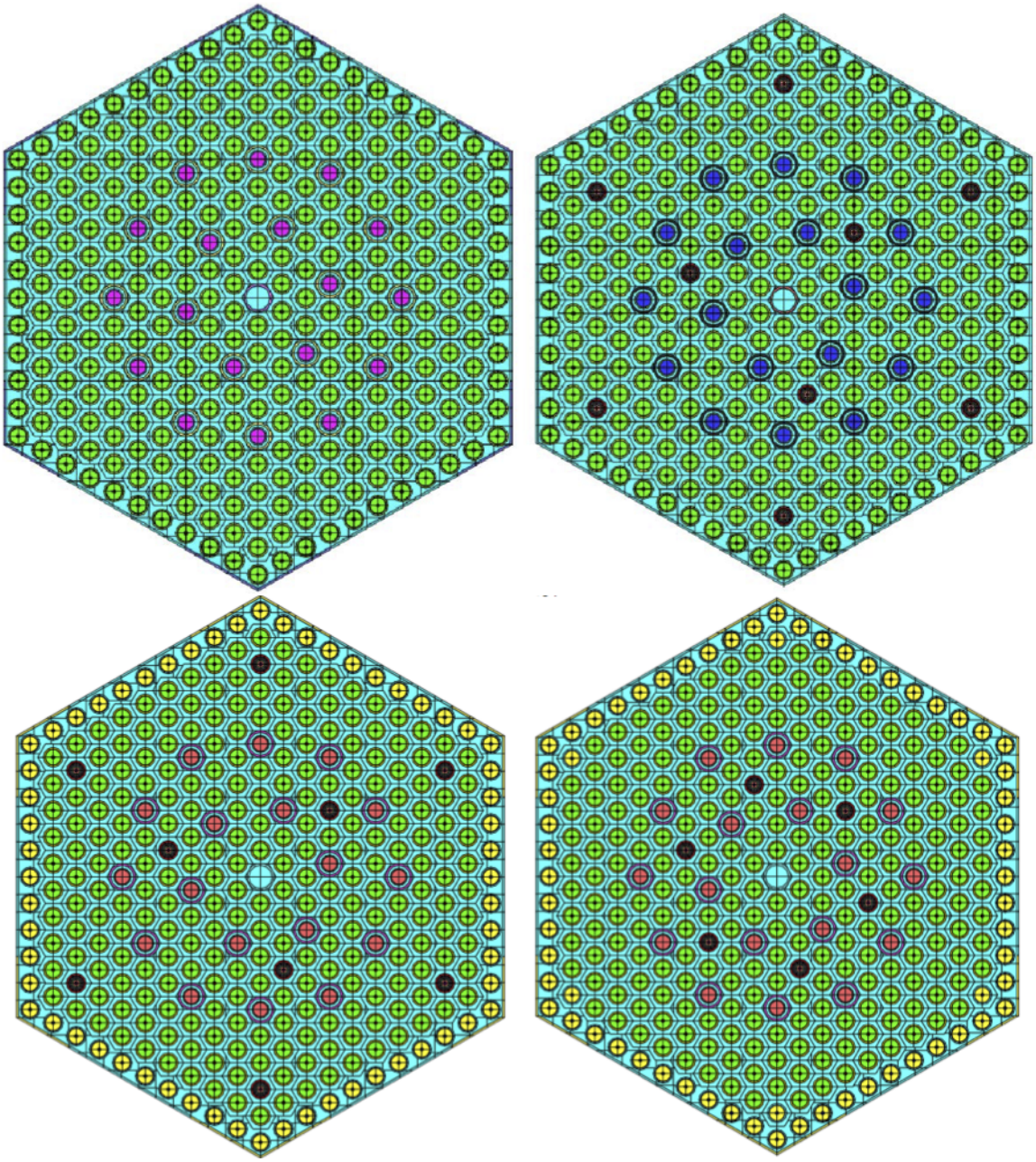

Figure 3.2: Lattices used in VVER full core modeling. [Top Left] 13au and 22au which have the same layout but differing enrichment. [Top Right] 30av5. [Bottom Left] 39awu. [Bottom Right] 390go.

VVER-1000 benchmark code calculations. It is worth noting that the NESSEL results appears to deviate significantly from the results of the other codes. The reason for this deviation is not know, but it does manifest in both the nuclide and k_∞ results.

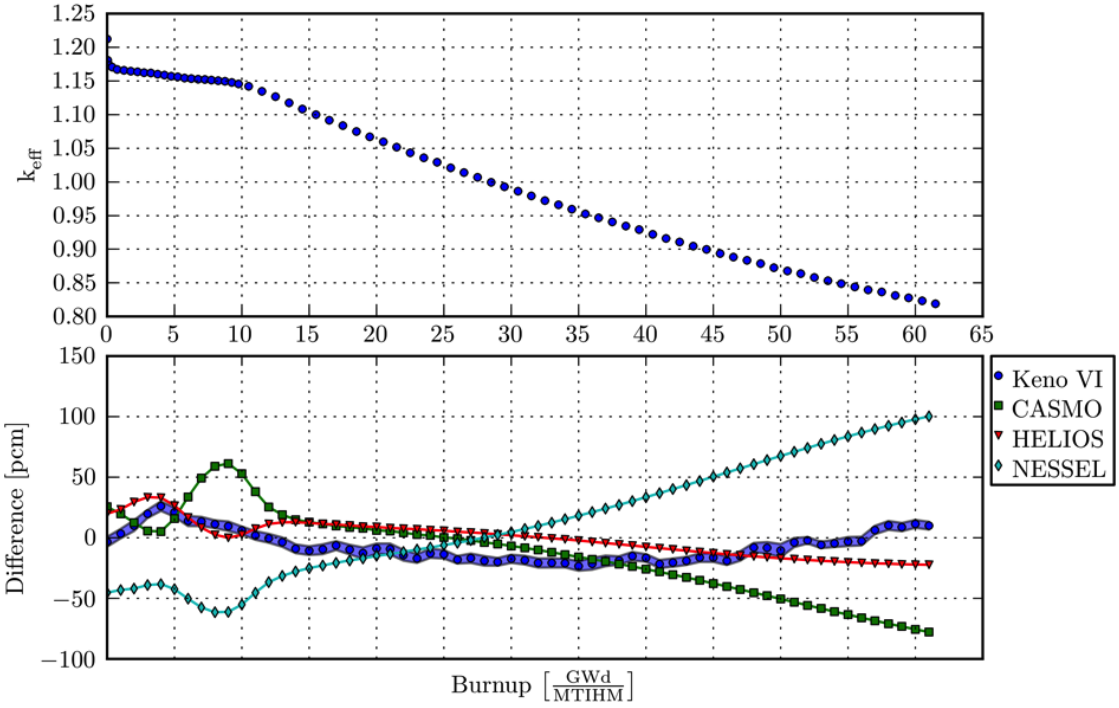

Figure 3.3: [Top] Lattice k_∞ for the 39awu lattice. [Bottom] Differences from the AER VVER-1000 benchmark average of three codes. The band around the KENO-VI results represents the standard error of the Monte Carlo calculation.

The motivation for using a nodal core simulator for spent fuel analysis is illustrated by Figure 3.5. Similar results were computed by the benchmark authors(20). This figure shows the thermal effect of moderator density on ^{239}Pu concentration, which can be greater than 10% at high burnup. In order to accurately model SNF nuclide composition precisely, a thermal calculation must be performed. Typical lattice physics tools do not perform these calculations. NESTLE quickly and accurately performs thermal feedback calculations using its cross section models. However, as will be shown in the next section, NESTLE's macroscopic cross section models are inadequate for detailed nuclide inventory calculation (in part due to the history effects). The current approach for accurate SNF modeling is to use the results of a thermal calculation as input into neutron transport codes in models that often do not account for intranodal effects.

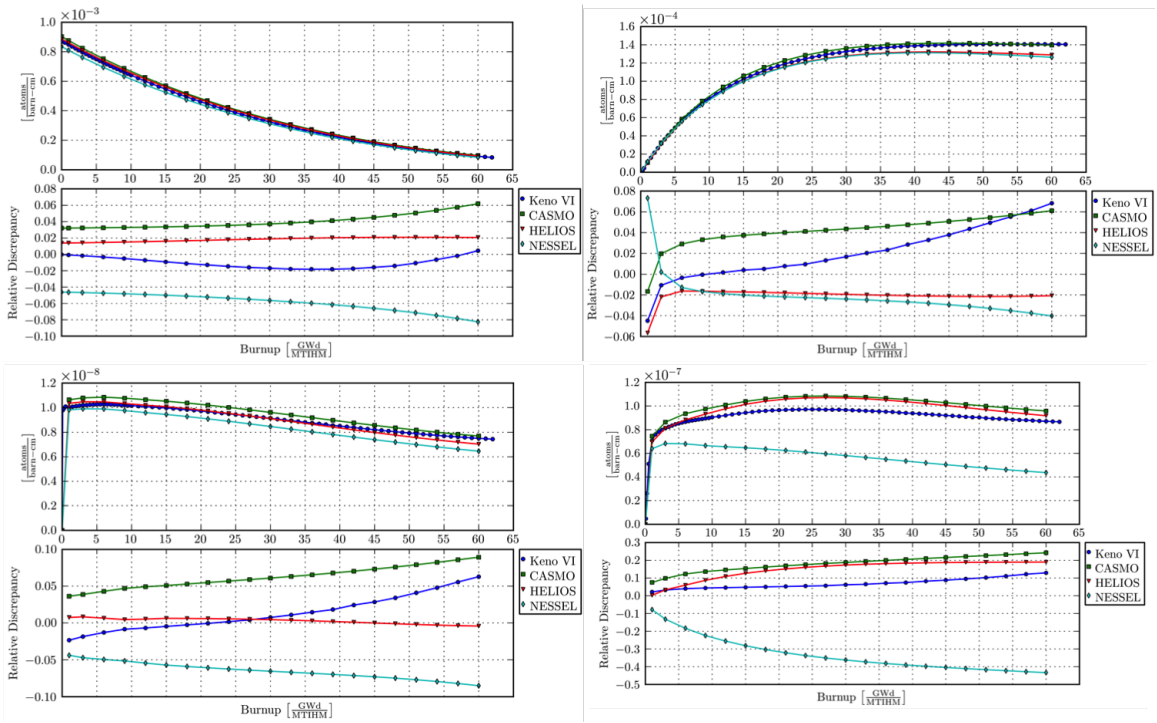

Figure 3.4: Nuclide compositions for the 39 awu lattice as calculated by KENO-VI compared to AER VVER-1000 benchmark reported values for ^{235}U [Top Left], ^{239}Pu [Top Right], ^{135}Xe [Bottom Right], ^{149}Sm [Bottom Right].

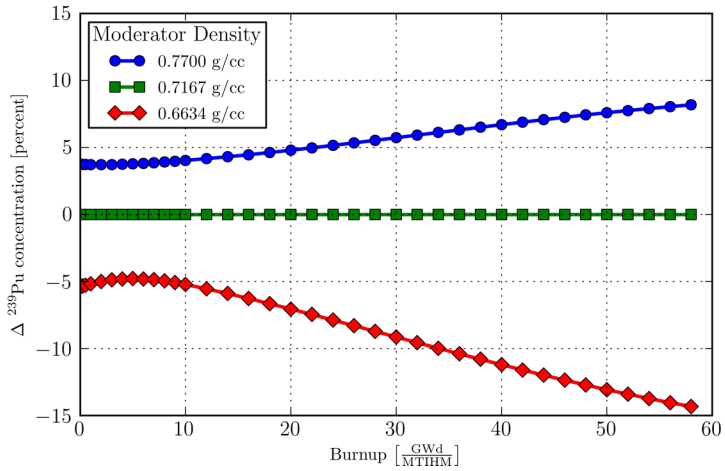

Figure 3.5: Effect of moderator density on the relative discrepancy of ^{239}Pu concentration in the 398Go lattice used in the AER VVER-1000 benchmark.

3.6 AER VVER-1000 Cycle 1 Core Follow

Cycle 1 of the AER VVER-1000 benchmark used five assembly types with five lattices and was modeled with NESTLE (11). Cycle 1 is an initial core, so some lattices use low enrichments (1.3%), and the core is only depleted to approximately 12 GWd/MTU over 311 days. The five lattices, along with axial and radial reflectors, were modeled using the TRITON module from the SCALEv6.2 code. Branch cases were modeled for fuel temperature, moderator density and temperature, soluble boron concentration and rod state. The homogenized two-group data were input into NESTLE, along with the cycle 1 operational data.

3.6.1 Whole Core Modeling with NESTLE

The core consists of 163 hexagonal fuel assemblies on a 23.48 cm triangular pitch. Table 3.2 shows the properties of the VVER-1000 benchmark core. The core loading pattern for cycle 1 is shown in Fig. 3.6.

Table 3.2: Properties of the cycle 1 AER VVER-1000 benchmark core.

Property	Value
Number of assemblies	
13au	48
22au	42
30av5	37
39awu	24
390go	12
Number of Assemblies with control rods	61
Control rod groups	10
Active fuel height [cm]	355.0
Thermal power [MW]	3000
Coolant inlet temperature [K]	563.15
Coolant outlet temperature [K]	592.75
Core pressure [MPa]	15.7

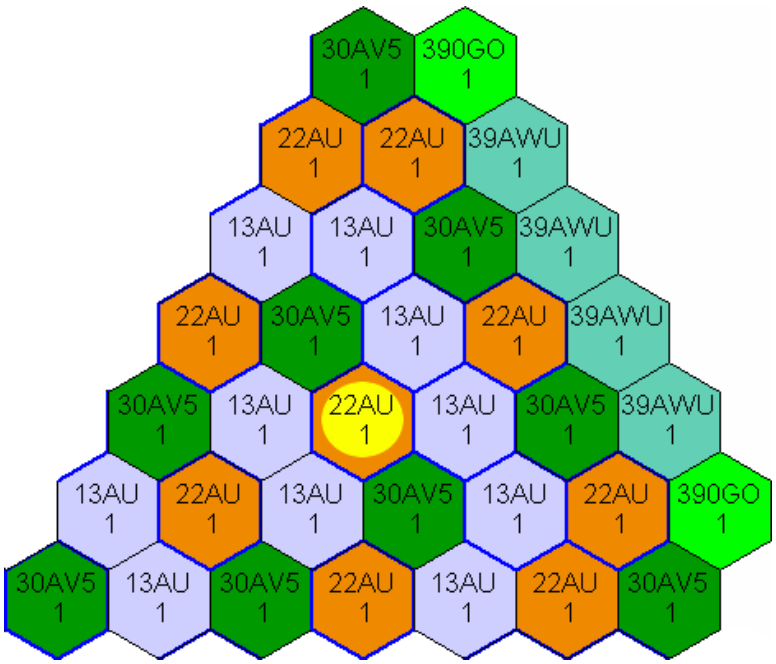

Figure 3.6: The loading pattern for cycle 1 of AER VVER-1000 benchmark has one-sixth symmetry across the core. The assembly with yellow highlight contains the maneuvering control rod group.

Typical power operation uses one group of control rods at 6 symmetric assembly locations to maintain criticality. Control rods are axially heterogeneous, where 30 cm at the rod tip is composed of Dy_2O_3-TiO_3 and the remainder B_4C. This feature was important to correctly modeling the core because NESTLE can only model one type of control rod for each fuel node. Fortunately, the depth of control rod insertion was shallow enough such that during most of the cycle only the uppermost fuel node was exposed to B_4C during the majority of the cycle while the other nodes in the upper core were exposed to the Dy_2O_3-TiO_3 section of the control rod.

3.6.2 Benchmark Calculations and Results

Plant data for Khmelnitsky-2 was input into NESTLE for over 335 operating points for a 10-month initial cycle. Each of the 163 fuel assembly consists of a single node in the XY plane. Two rings of nodes along the outer periphery formed the radial reflector. The active fuel length was divided into 20 equal length nodes.

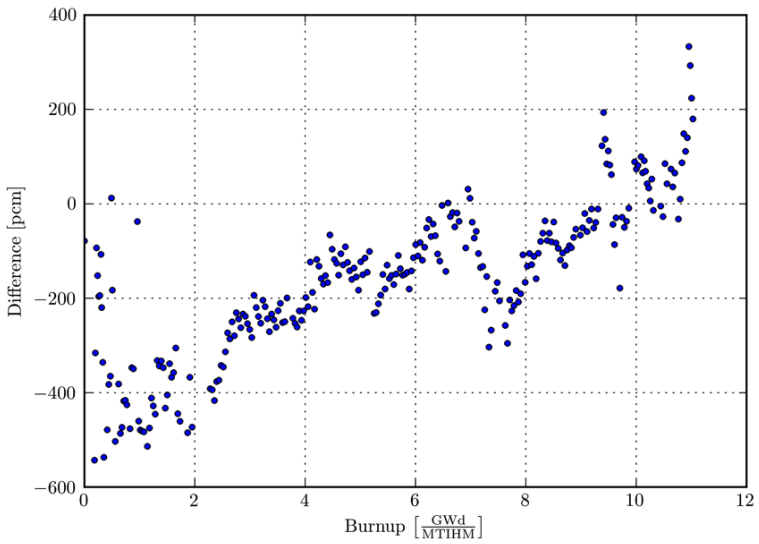

Figure 3.7: AER benchmark VVER-1000 core k_{eff} as calculated by NESTLE.

NESTLE performs two types of k_{eff} eigenvalue calculations: one where the boron letdown is input and k_{eff} is calculated, the other where k_{eff} is assumed to be unity and the boron letdown is calculated. Figure 3.8 compares the boron letdown as calculated by NESTLE to the measured boron values. Compared to other values computed by five different codes in the AER VVER-1000 benchmark, nearly all of the NESTLE calculated values deviate less than the maximum deviation, and most of the calculated values are within one standard deviation. Figure 3.7 shows the difference in pcm for core k_{eff} values calculated by NESTLE compared to the benchmark data. The greatest discrepancies in the range of 300 pcm to 500 pcm occur near the beginning of the cycle. This time interval corresponds to lower power operation and non-equilibrium fission product concentration, which may be a possible source of discrepancy, due to the approximations in the way short lived fission products are treated in NESTLE. After approximately 4 GWd/MTU, the discrepancy ranges mostly between ±200 pcm for the remainder of the cycle. This deviation is considered good agreement between expected and calculated values for a core follow calculation based on biases observed with typical commercial LWR simulators(27). The low discrepancies shown in Figures 3.8 and 3.7 are good indications that the core has

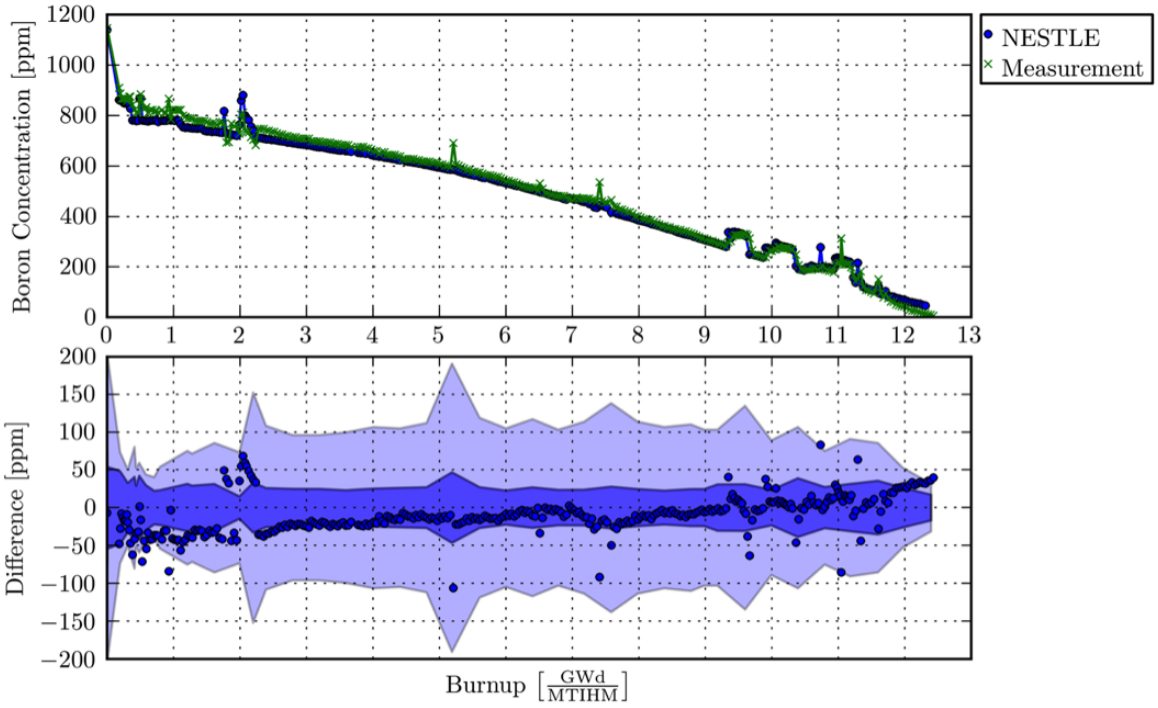

Figure 3.8: [Top] Critical boron concentration as calculated by NESTLE and reported in the AER VVER-1000 benchmark. [Bottom] Difference between NESTLE and AER VVER-1000 benchmark values. The darker shaded band is one standard deviation of the benchmark calculated values and the lighter shaded band is the maximum deviation.

been correctly modeled and that the calculated fuel and coolant temperatures are reasonable. It is likely that the inability to currently model axially heterogeneous control rods may explain some of the discrepancies seen in the k_{eff} calculation.

The benchmark proposal includes several tasks for lattice and core modeling. Benchmark task 2 specifies that the critical boron concentration be calculated for 3D core burnup calculations. Thermal hydraulic feedback and the criticality search function were used in NESTLE find the critical boron concentration for cycle 1. The boron concentration as computed by NESTLE and reported by the benchmark for the first cycle are shown in Figure 3.8. Also shown is the discrepancy between the NESTLE calculation and the benchmark reported values. The darker shaded band in the plot is the envelope formed by one standard deviation of these five calculations, and the lighter shaded band is the envelope formed by the maximum deviation. Figure

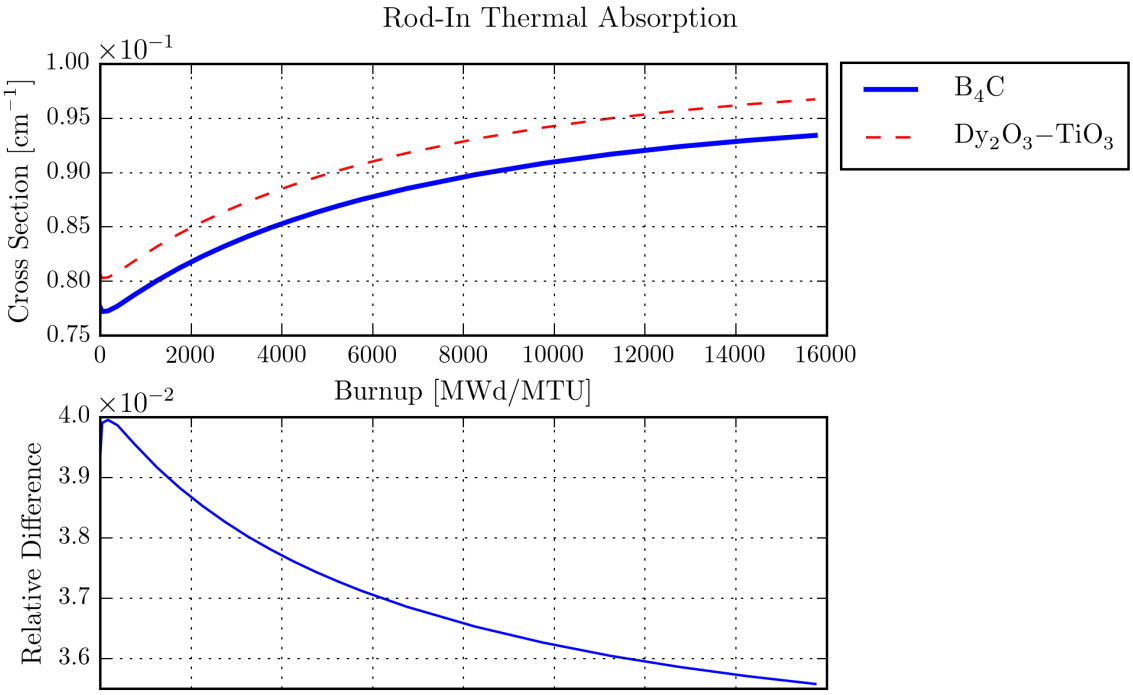

Figure 3.9: The homogenized macroscopic thermal absorption cross sections for the 22au lattice with B_4C and Dy_2O_3-TiO_3 control rods.

3.8 shows that the NESTLE calculated boron concentration is within one standard deviation at most burnup points and is within the maximum deviation at almost all burnup points.

The boron concentration results achieved with NESTLE show a larger discrepancy with the benchmark reported values near the beginning of the cycle and appear to decrease with burnup. It is possible that this is due to the fission product treatment, particularly samarium, early in the cycle.

Another source of model error is the heterogeneous control rods. The control rods are mostly composed of B_4C, but the tips (30 cm) are composed of Dy_2O_3-TiO_3. As previously discussed, NESTLE does not handle heterogeneous control rods, so only the Dy_2O_3-TiO_3 material was modeled. Because the rods are usually only shallowly inserted during operation, this is adequate at most burnup points, but model errors do

increase with deeper rod insertion when the B_4C sections of the control rods penetrate the upper regions of the core. The difference in the thermal absorption of the 22au lattice with B_4C and Dy_2O_3-TiO_3 control rods is shown in Figure 3.9.

3.6.3 Analysis of Core Power Distributions

An analysis of the core power distributions of cycle 1 was performed to resolve or explain the discrepancies observed in the core follow calculations. The benchmark reports assembly averaged power for each assembly at given core averaged burnups during cycle 1. The first of these occurs at 530.05 MWd/MTU (13.4 EFPD). Note that this is early in the cycle when the discrepancy in k_{eff} is near it's largest value. The values reported are based on Self Powered Neutron Detetor (SPND) measurements (where instrumented), reconstructed values, and calculated values. Figure 3.10 illustrates the NESTLE computed values compared to the calculated values reported in the benchmark.

In all assembly locations, the assembly averaged power as calculated by NESTLE is within ±2% of the calculated values reported in the benchmark and the RMS error is 0.75%. These values show generally good agreement. The greatest differences appear near the core periphery and near the core radial center of the core, while the smallest differences occur in the annular region between the center and periphery. Much effort and time was spend on improving the radial reflector (see Chapter 6), and based on the comparison of the radial power distributions, the radial reflectors do not appear to be the largest contributor to the modeling errors of cycle 1.

The benchmark also reported the axial offset for cycle 1. The axial offset is a single value that is a measure of the axial power distribution defined as:

$$AO = \frac{P_{\text{top}} - P_{\text{bot}}}{P_{\text{top}} + P_{\text{bot}}} \tag{3.1}$$

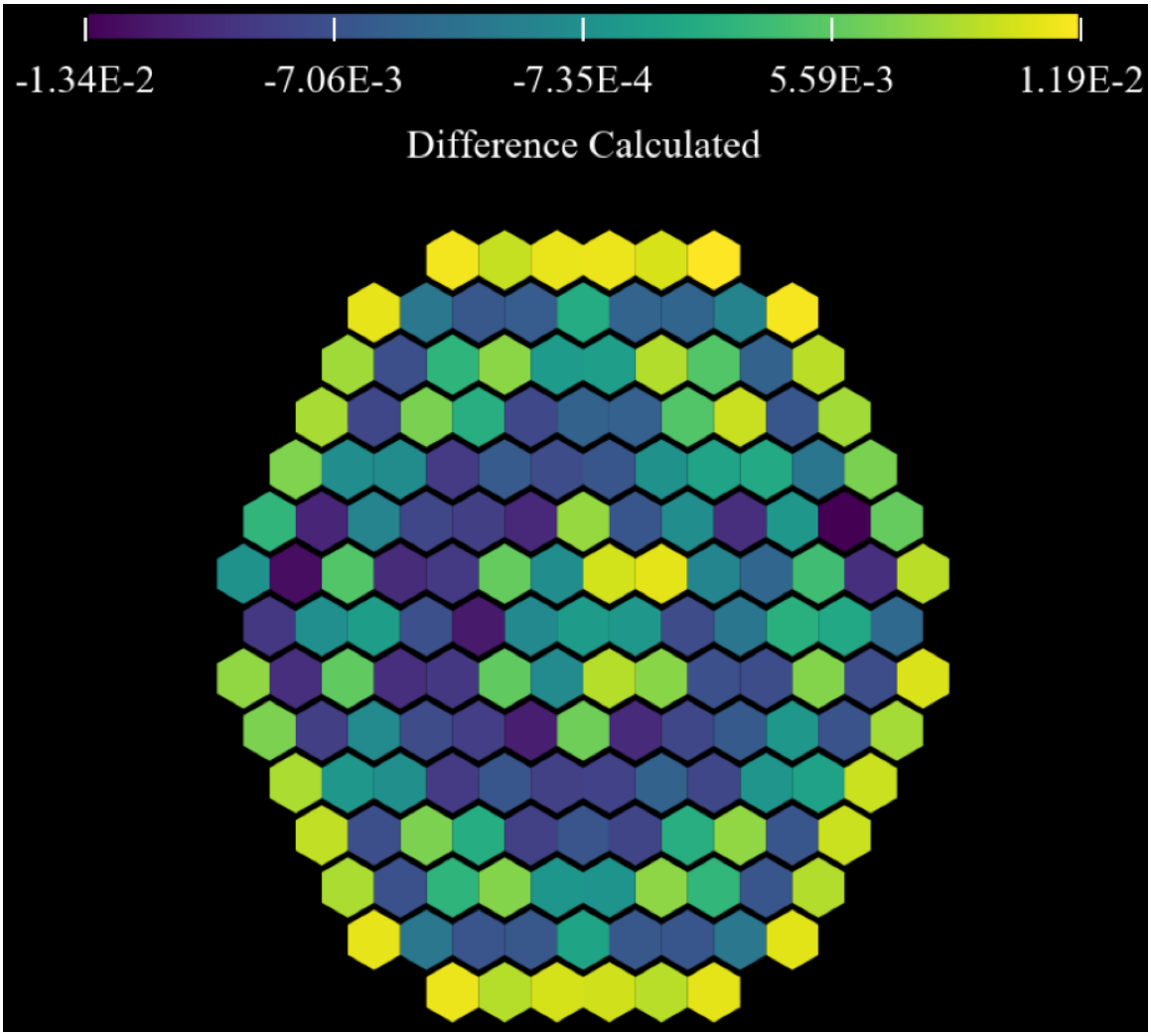

Figure 3.10: The absolute error in the radial power distribution as computed by NESTLE compared to the calculated values as reported in the AER VVER-1000 benchmark at a core average burnup of 530.05 MWd/MTU.

where P_{top} is the power produced in the top half of the core and P_{bot} is the power produced in the bottom half of the core. The axial offset was computed by NESTLE at each burnup state during the core-follow calculation. The benchmark reported values and the NESTLE computed values are shown in figure 3.11.

The axial offset was computed by NESTLE using the axial reflectors as specified by the benchmark. The axial reflector cross sections and assembly discontinuity factor (ADF)s (top and bottom) were computed by using one-dimensional

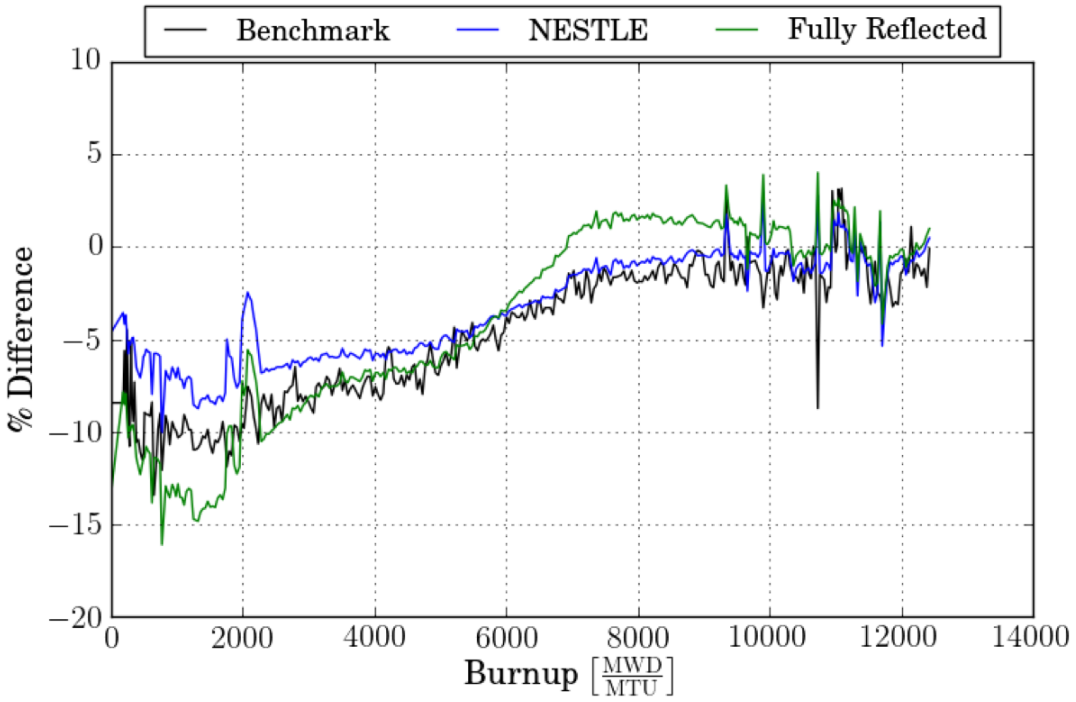

Figure 3.11: The axial offset values as reported by the benchmark (label: Benchmark), computed by NESTLE using the prescribed axial reflector models (label: NESTLE), and computed by NESTLE using a fully reflected boundary condition in place of axial reflectors (label: Fully Reflected).

lattice-reflector models. Early in the cycle, the axial offset computed by NESTLE is approximately 4% greater than the benchmark axial offset. Also early in the cycle, the discrepancy in k_{eff} is near it's largest value. As the core continues to burn the discrepancy between NESTLE and the benchmark axial offset values decreases.

Aa second calculation was conducted where the benchmark specified axially reflectors were replaced by fully reflected top and bottom boundary conditions. In this calculation, the axial offset is computed to be more negative than the benchmark in the early part of the cycle, and more positive in the latter part of the cycle. During the first half of the cycle, the NESTLE calculations with the benchmark specified axial reflectors and the fully reflected boundary conditions bracket the benchmark reported values.

Comparisons of these axial offset values indicate that early in the cycle the NESTLE calculation with the benchmark specified axial reflectors has too much power at the top of the core and not enough at the bottom of the core. The fully reflected model indicates that if the axial reflector were to modeled in a different manner, such that the total axial reflection were to increase, the axial offset discrepancy could be reduced. Since more of the power is generated at the bottom of the core during the first half of the cycle, the early discrepancy may be an indication that the core model would benefit most from an improved bottom axial reflector. The correlation between the early cycle k_{eff} discrepancy and the axial offset discrepancy may be an indication that k_{eff} agreement would improve with a better bottom and top axial reflector models. Improving the axial reflector models by using explicit reflector geometry and 2D models remains as work to be explored in the future.

3.7 Depletion with Temperature Adjustments

In section 3.6.2, spatial- and time-dependent thermal-hydraulic conditions from a whole-core 3D nodal simulator were generated with NESTLE for the AER VVER-1000 benchmark. The calculation employed actual design and operational data for the Khmelnitsky-2 Cycle 1 to determine the resulting internal thermal-hydraulic conditions applicable to fuel and moderator regions for all fuel assemblies and axial regions. This section describes an approach where calculated fuel and moderator temperature profiles are processed or averaged and then applied in high fidelity MCNP6 calculations of the SNF isotopic inventory for specific fuel assemblies.

The 3-dimensional plots in Figures 3.12 and 3.13 illustrate the range of fuel and coolant temperatures throughout the core at the beginning and end of the cycle. These plots demonstrate the variation in temperature distributions over the cycle interval. For one of the fuel assemblies evaluated in the benchmark, the effective fuel temperature profiles calculated fall within a range of 800 K to 1400 K and are time and space dependent. Likewise, the coolant or moderator temperature profiles

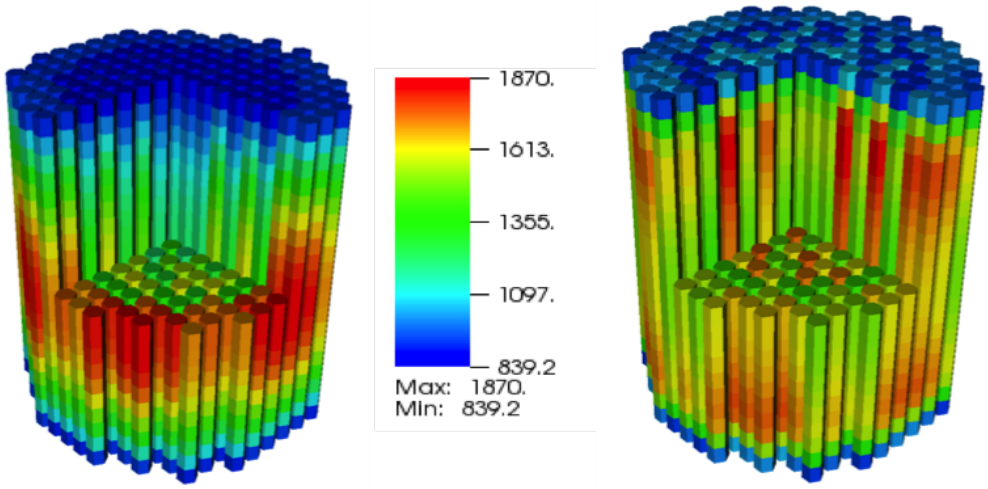

Figure 3.12: [Left] Beginning of cycle fuel temperature distribution (in degrees Fahrenheit). [Right] End of cycle fuel temperature distribution.

range from approximately 550 K to 590 K. The temperatures impact cross sections and ultimately impact the calculated SNF nuclide compositions. These values are generally not available for Monte Carlo modeling but they impact the spent fuel nuclide compositions. If the reactor operator does not provide these temperature data, then they must be obtained by independent means.

In thermal systems, the build-up rate of plutonium is strongly dependent on moderator conditions, such as moderator density and the S(α, β) scattering laws. For a PWR, a change in the coolant temperature will also result in a change of moderator density. As low as a 30 K difference in moderator temperature may result in over 1% discrepancy in ^{239}Pu concentration at high burnup. For a pressurized core, a change in the coolant temperature results in a change in the moderator density. Two of the AER VVER-1000 benchmark authors quantified the impact of moderator density history on the 390go lattice. The authors conclude that the moderator density changes can affect the ^{239}Pu concentration by greater than 10% at a burnup of 50-60 GWd/MTU. Therefore, calculating the localized conditions is a requirement for high-fidelity depletion calculations.

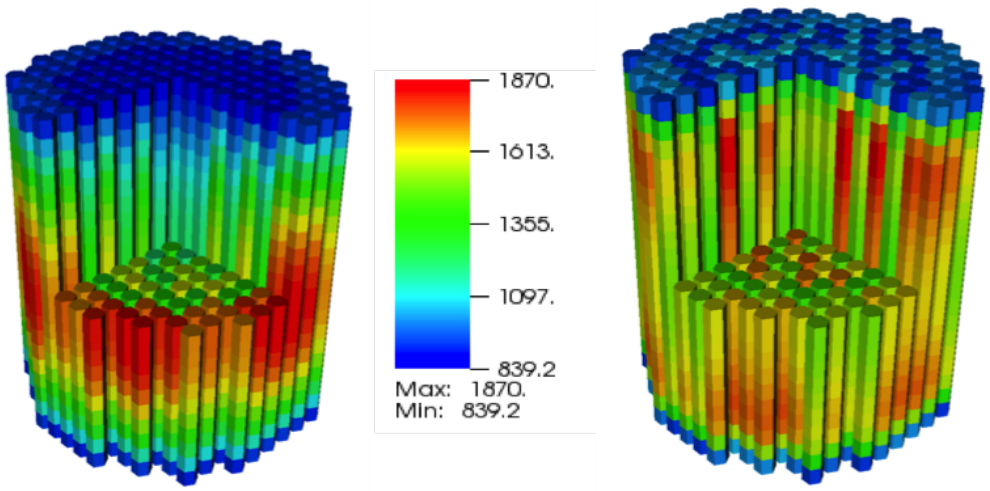

Figure 3.13: [Left] Beginning of cycle coolant temperature distribution (in degrees Fahrenheit). [Right] End of cycle coolant temperature distribution.

3.7.1 Monte Carlo Depletion with Thermal Adjustments

The observations outlined in the previous section confirmed and reinforced the importance of whole-core space- and time-dependent fuel and coolant temperature distributions generated on the basis of specific design specifications and actual operational conditions. Ideally, thermal-hydraulic feedback can be determined iteratively on the fly by coupling neutronics and thermal-hydraulic calculations, as it is done in NESTLE. In practice, however, we have concluded that iterative full-core Monte Carlo-based depletion with a fine space/time assignment of localized temperatures (or iterative thermal-hydraulic feedback) remains largely unmanageable at this point, primarily due to excessive computer time requirements, but in some cases due to lacking code-specific features required to handle the time-dependent parameters. The definition of a manageable calculation used in this context is one that requires several CPU days on a cluster equipped with 300 to 400 processors. In many cases, this approach requires from tens to hundreds of thousands of lines the input to describe the geometry and operating conditions.

In order to generate more manageable high-fidelity Monte Carlo-based depletion models, a hybrid deterministic/stochastic approach was investigated. First, the 3D deterministic nodal diffusion simulator NESTLE is used to determine space- and time-dependent thermal-hydraulic conditions for the AER VVER-1000 benchmark using actual plant data. Second, assembly- and time-averaged axial profiles of moderator and fuel temperatures are input into a high-fidelity MCNP6 depletion model of a selected fuel assembly (not full core). This approach provides a first-order estimation of the impact of using more detailed and realistic temperature profiles (versus isothermal profiles) on the calculated isotopic inventory of VVER-1000 fuel assemblies.

Figure 3.14 and Figure 3.15 plot the axial profiles for burnup-dependent effective fuel temperature and moderator temperature of a single representative assembly as a function of core average burnup. These temperature profiles readily and quickly emerged from the NESTLE evaluation of the AER benchmark, and they constitute the first step of the two-step hybrid approach described herein. The color legend in these plots ranges from dark blue to dark red to denote burnup, and the thick dark black lines in the plots represent the average temperature conditions of the fuel and moderator throughout the cycle. These assembly- specific and cycle-averaged temperature data are then input to a 3D fuel assembly Monte Carlo-based depletion model.

In the hybrid approach described, these axial- and assembly-dependent temperature profiles were then averaged over the cycle length to create (1) two temperature input profiles for use in MCNP6 assembly- level 3D high fidelity depletion calculations, (2) an axially varying profile, and (3) an axially isothermal (averaged) profile. The purpose of this exercise was to estimate, in a manageable fashion, the impact of using an axially varying temperature profile versus a constant (isothermal) temperature value upon SNF isotopic concentrations of VVER-1000 fuel assemblies. Therefore, the 3D assembly simulation was performed in two ways. First it was performed with axially uniform (constant) fuel and moderator temperature profiles.

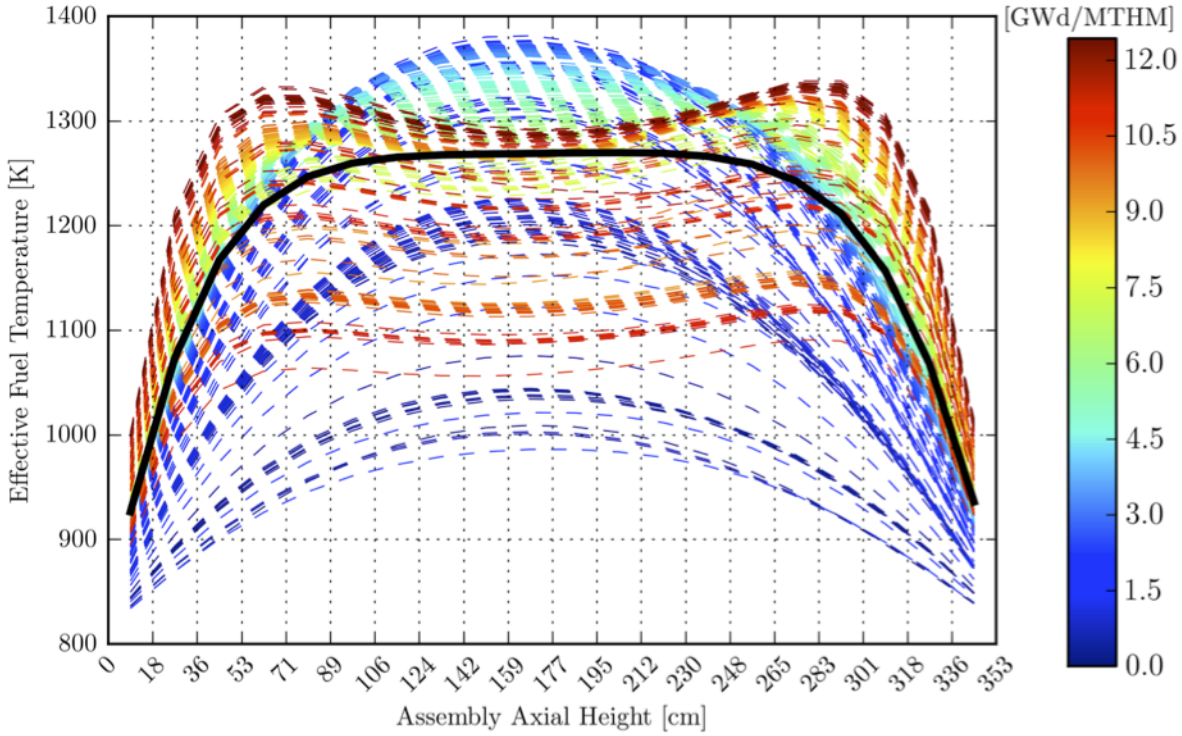

Figure 3.14: Effective fuel temperature profile versus core averaged burnup computed by NESTLE

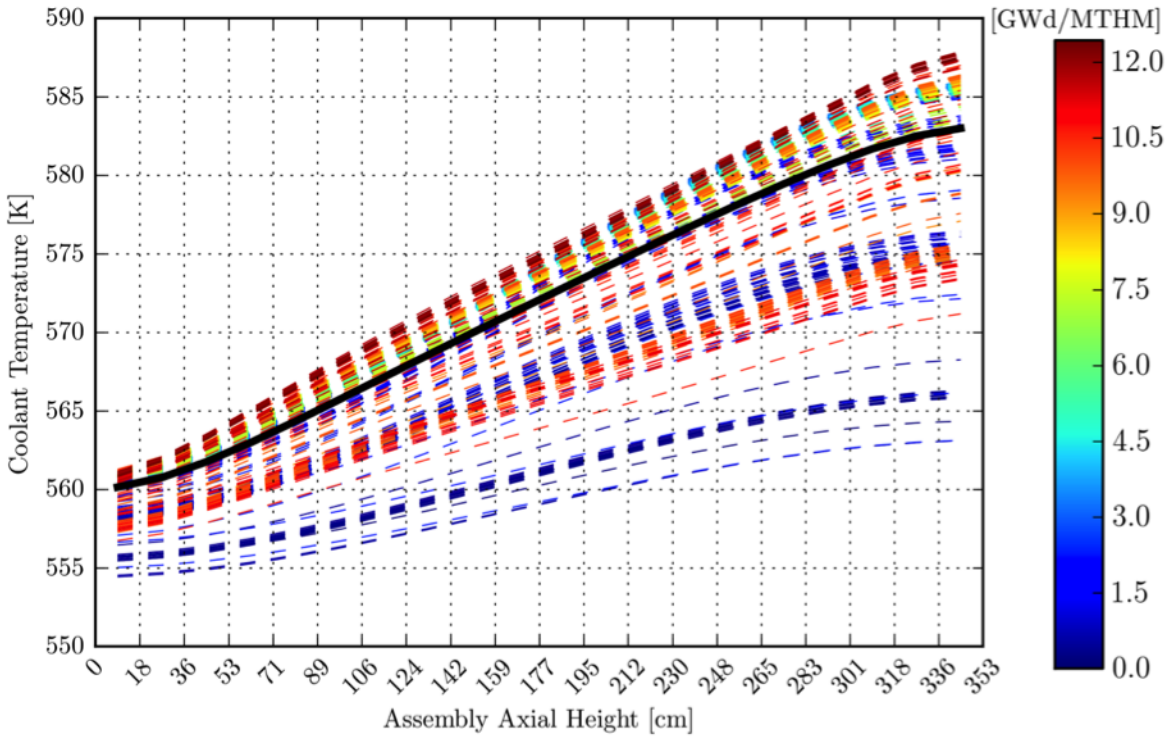

Figure 3.15: Moderator temperature profile versus core averaged burnup computed by NESTLE

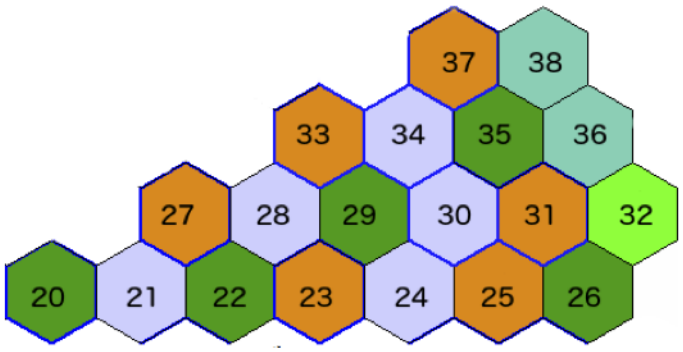

Figure 3.16: AER benchmark core layout in the 1/12th core symmetry illustrating the location of fuel assemblies. Assembly 21 (lower left, shown in purple) was selected for two-step hybrid calculations.

Then the calculation was repeated by using cycle-averaged axial varying temperature profiles. Based on the observations shown in Fig. 3.16, assembly 21 (type 13au) was selected for this study. This assembly is centrally located and not in the vicinity of strong flux gradients. It is located away from operational control rods and is not located at the outer edge of the core near the reflector. Thus it is expected to exhibit the operational features of a typical fuel assembly.

Table 3.3 tabulates the numerical values of the cycle-averaged axially varying profiles of fuel and moderator temperatures and the moderator density provided in contrast to axially flat (constant) profiles. These two temperature representations were employed with MCNP6 assembly models of assembly 21. The axial node 1 is the bottom node and 10 is the top node.

Assembly 21 was selected for analysis using MCNP6 with the depletion performed with CINDER-90. The average power of the assembly over the first operational cycle was 14.8 MW, with a cumulative exposure of this assembly of 281.63 effective full power days (EFPDs), had an end-of-cycle assembly average burnup of 10 GWd/MTU.

Figures 3.17, 3.18, Figure 3.19 summarize the representative results obtained for Assembly 21 at various axial heights, for axial nodes 1, 5, and 10, which are located at axial heights 17.75, 159.75, and 337.25 cm respectively. These

Table 3.3: Axially varying and constant profiles of fuel temperature, coolant, and density.

Axial Node	Center height (cm)	Fuel temp (K)	Coolant temp	Coolant density (g/cc)
1	17.75	1000	560	0.7516
2	53.25	1194	562	0.7480
3	88.75	1254	565	0.7429
4	124.25	1266	568	0.7374
5	159.75	1269	571	0.7318
6	195.25	1269	574	0.7261
7	230.75	1267	576	0.7204
8	266.25	1249	579	0.7147
9	301.75	1179	581	0.7095
10	337.25	988	593	0.7060
Node Averages		1195	572	0.7292

locations represent the lower, middle, and upper axial regions of the assembly. The plots in each of the above-noted figures compare EOC isotopic inventories of ^{235}U, ^{238}U, ^{239}Pu, ^{240}Pu, ^{241}Pu (top bar chart), as well as exposure-dependent inventory profiles for these isotopes (lower plot) extending through the EOC burnup for each specific axial node: 1, 5, and 10, respectively. The deviations shown are evaluated by comparing the calculated inventory of a given isotope under the assumption of the cycle-averaged axially varying temperature distribution (profile) relative to the averaged (constant) profile, whereby the relative discrepancy is calculated as (profile - constant)/(constant). The isotopic inventory results for the assembly and nodes selected indicate relative discrepancies that range between 1%- 3% at EOC. The largest differences occur at the low burnup top of the assembly, where the coolant density and temperature deviate the most from the average and where the fuel temperature is much lower than average. Although the relative discrepancies appear to be large early in the cycle, the absolute discrepancies are small. The absolute discrepancies actually increase with burnup, while the relative discrepancies decrease.

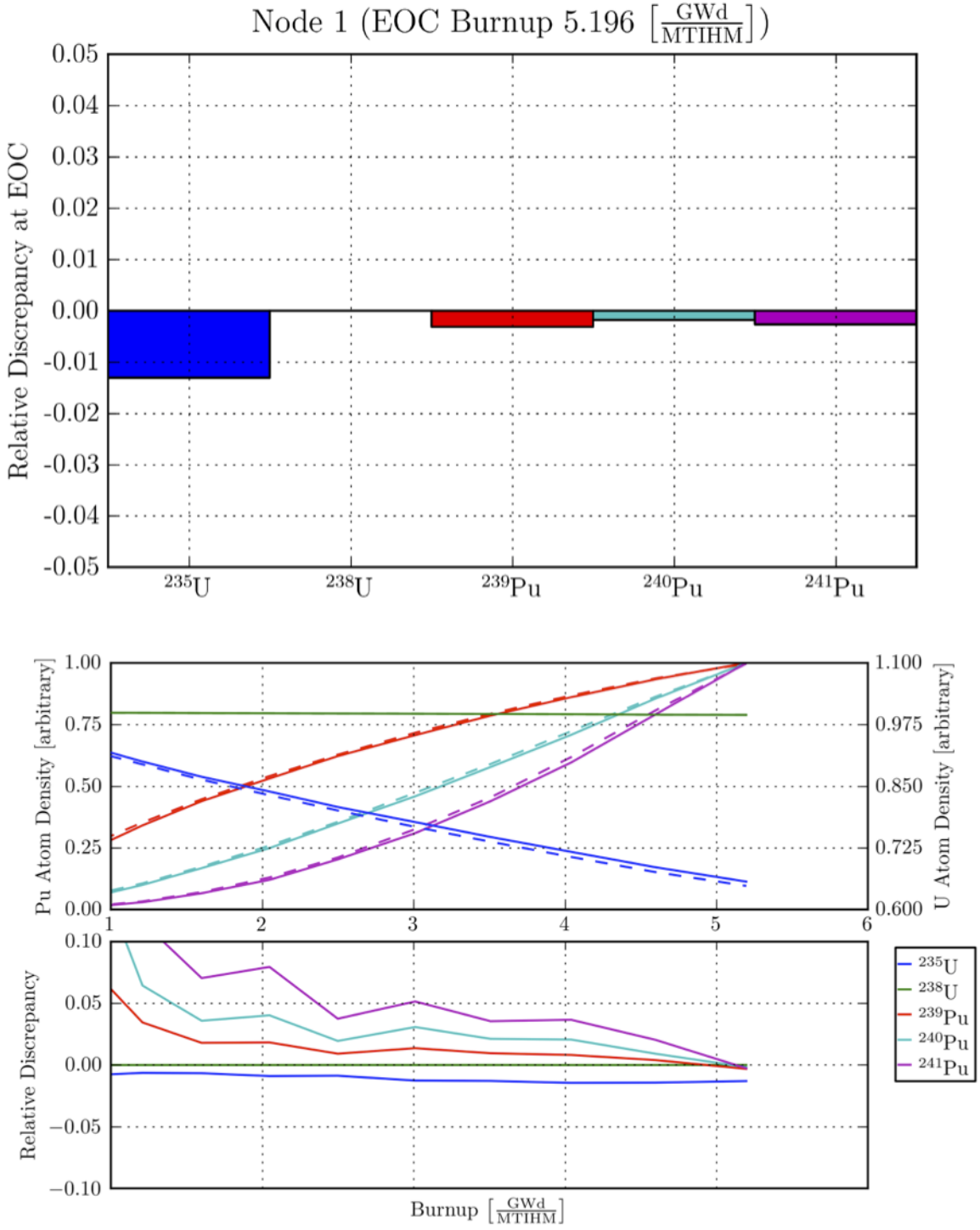

Figure 3.17: High fidelity MCNP depletion of Assembly 21, Node 1 (17.75 cm). Impact of using axially varying versus flat temperature profile upon U/Pu isotopic concentrations. EOC (top), burnup-dependent (bottom).

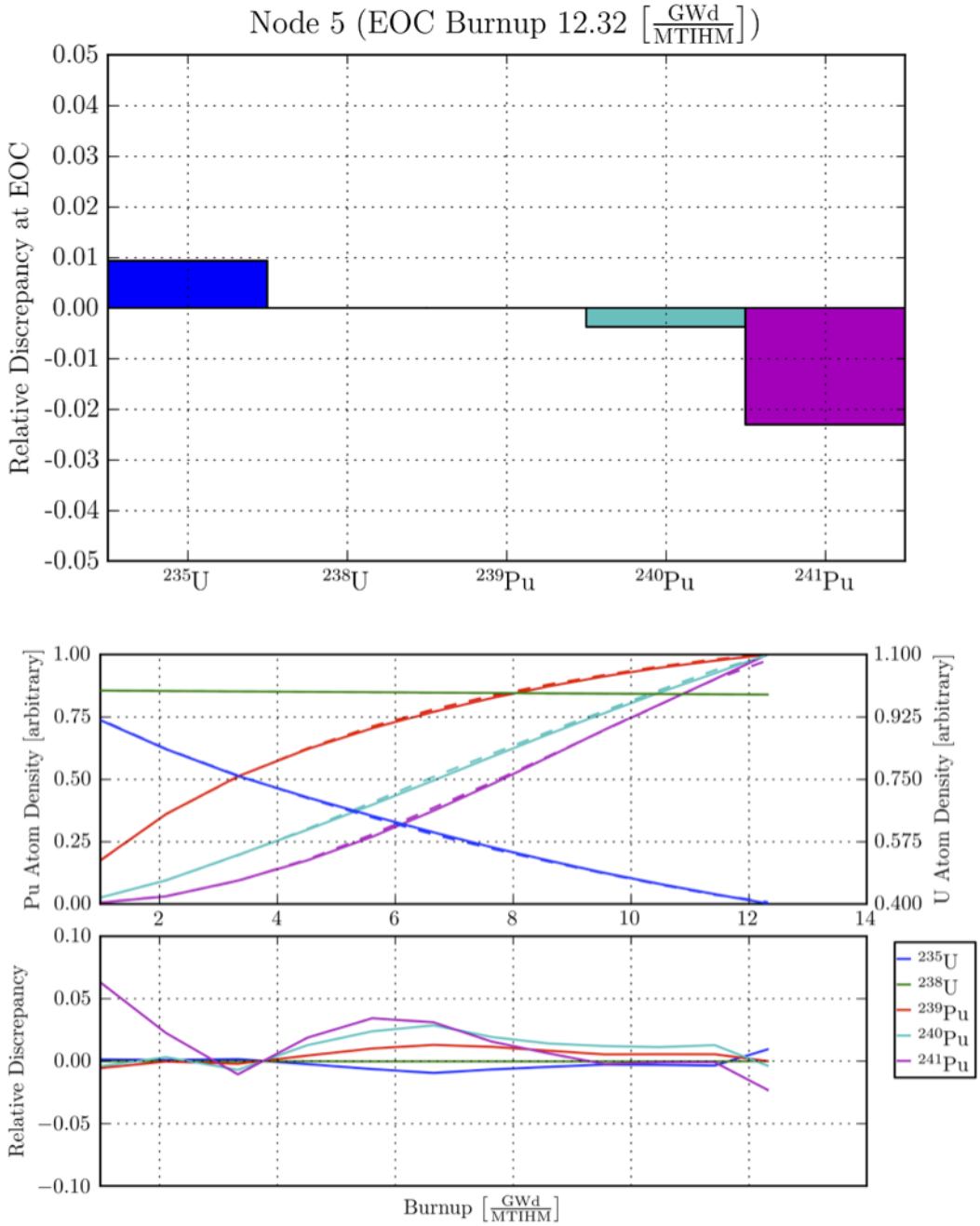

Figure 3.18: High fidelity MCNP depletion of Assembly 21, Node 5 (159.75 cm). Impact of using axially varying versus flat temperature profile upon U/Pu isotopic concentrations. EOC (top), burnup-dependent (bottom).

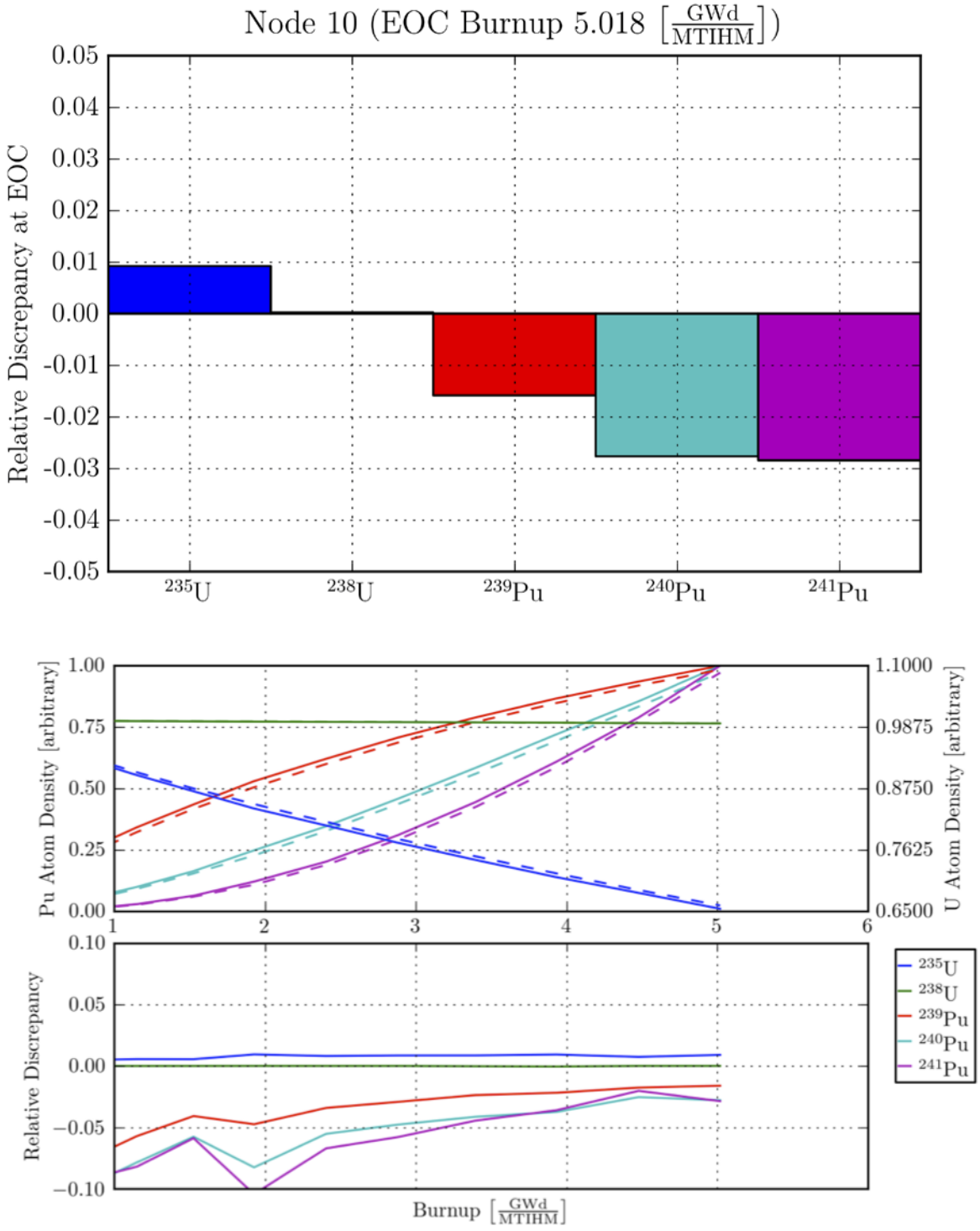

Figure 3.19: High fidelity MCNP depletion of Assembly 21, Node 5 (337.25 cm). Impact of using axially varying versus flat temperature profile upon U/Pu isotopic concentrations. EOC (top), burnup-dependent (bottom).

Chapter 4

Microscopic Depletion

4.1 Microscopic Depletion in NESTLE

One objective of this work is to extend and improve the depletion capabilities of NESTLE to adequately describe the nuclide inventory of spent nuclear fuel at the assembly and pin level. Depletion is a general term used to describe the evolution of nuclear fuel composition during power production, but this evolution does not occur as a single process, rather it is the result of many hundreds of transmutation, fission, and decay processes. These processes are described by the Bateman equations, which all nuclear evolution codes must solve. The Bateman equations can be concisely expressed as:

$$\frac{d}{dt}N_i(\vec{r},t) = \sum_j B_{ij}(\vec{r},t)N_j(\vec{r},t) \tag{4.1}$$

where B_{ij} is an element of the transition matrix

$$B_{ij} = \begin{cases} L_{ij}\lambda_j + \sum_r Y_{ij,r}\sigma_{j,r}(\vec{r},t)\phi(\vec{r},t) & \text{for } i \neq j \\ -\lambda_i - \sum_r \sigma_{i,r}(\vec{r},t)\phi(\vec{r},t) & \text{for } i = j \end{cases} \tag{4.2}$$

where N_i is the number density of nuclide i, λ_i is the decay constant of nuclide i, $Y_{ij,r}$ is the one-group yield of nuclide i for reaction r on nuclide j, $\sigma_{i,r}$ is the one-group microscopic cross section of nuclide i for reaction r, $L_{ij}\lambda_j$ is the fraction of all disintegrations of nuclide j that results in the creation of nuclide j, and $\phi(\vec{r},t)$ is the one-group scalar flux.

The primary function of NESTLE is to solve the few-group neutron diffusion equation:

$$-\vec{\nabla}\cdot D_g\vec{\nabla}\phi_g+\Sigma_{tg}\phi_g=\sum_{g'=1}^{G}\Sigma_{sgg'}\phi_{g'}+\frac{\chi_g}{k}\sum_{g'=1}^{G}\nu_{g'}\Sigma_{fg'}\phi_{g'} \tag{4.3}$$

where D_g is the diffusion coefficient, and the Σ are the macroscopic cross sections.

NESTLE is not a general nuclear evolution code, but it does use depletion cross sections as input to solve the neutron diffusion equation at various stages of burnup. Currently, NESTLE has two depletion models: a macroscopic model, and a hybrid macro/microscopic model.

The macroscopic model has been commonly used with NESTLE in particular and in general with industrial core modeling. The macroscopic model does not solve any of the Bateman equations directly, but relies on their solution during the lattice physics stage of the two-step process. During this stage, the nuclide concentrations are used to calculate the homogenized macroscopic cross sections at each burnup step. These cross sections are interpolated and used as input to solve the diffusion equations. With the exceptions of the fission product poisons ^{135}Xe and ^{149}Sm, NESTLE's macroscopic model never actually calculates any nuclide compositions directly. This should not be surprising as the primary results of a core simulation are reactivity, flux, and power distributions, not nuclide inventory. The calculation of nuclide compositions is only done as needed in service of these other results. The depletion model simply determines which macroscopic cross sections to interpolate based on the power computed in each node. Using this model, the only way

to estimate nuclide inventory is to assume the same compositions that were computed in the lattice physics calculation at a specified burnup, but these compositions do not account for the core conditions and so are of limited accuracy.

The hybrid macro/microscopic depletion model does solve simplified Bateman equations for a limited number of nuclides. The set of nuclides I includes: ^{234}U, ^{235}U, ^{236}U, ^{238}U, ^{239}Pu, ^{240}Pu, ^{241}Pu, ^{242}Pu, ^{241}Am, along with two lumped fission products and a burnable absorber. The number densities N_i^n for these nuclides (and pseudo-nuclides) i for node n are computed, and their products with the microscopic cross sections $\sigma_{i_{x,g}}^n$ of type x are summed with the background macroscopic cross section ${}^{\mathrm{BK}}\Sigma_{r,g}^n$:

$$\Sigma_{x,g}^n = {}^{\mathrm{BK}}\Sigma_{x,g}^n + \sum_i^I \sigma_{i_{x,g}}^n N_i^n \tag{4.4}$$

This model is capable of greater accuracy in determining the number densities of uranium and plutonium isotopes, but it does not directly compute the number densities of fission products measured in spent fuel assays.

4.1.1 Subregion Depletion

Currently, NESTLE does have some integration with ORIGEN, but this is limited to the subregion depletion capabilities. The subregion depletion feature can deplete elements within a node, such as fuel pins, by using additional lattice data passed from the lattice physics calculation. NESTLE's subregion depletion capability was originally developed (28) to estimate recycling of americium in boiling water reactors. Later the feature was revised to accommodate the latest release of ORIGEN (12), and was also extended to calculate the depletion of control rods (29).

The existing subregion depletion capabilities are based on precomputed neutron group flux disadvantage factors. Flux disadvantage factors are simply the ratio of one region's group flux to another region's. In this case, the disadvantage factors are the ratio of the group flux in a region of interest, such as a fuel material,

to the group flux of the entire homogenized lattice region.

$$\xi_{g,\text{region}} = \frac{\phi_{g,\text{region}}}{\phi_{g,\text{node}}} \tag{4.5}$$

To deplete a region during the core calculation, the group disadvantage factors are applied to the nodal flux to estimate the one-group flux within the region.

$$\phi_{\text{region}} = \sum_{g}^{G} \xi_{g,\text{region}} \phi_{g,\text{node}} \tag{4.6}$$

The subregion depletion feature as implemented in NESTLE uses a fully microscopic depletion model, and therefore requires microscopic cross sections. These microscopic cross sections are computed during lattice physics and are collapsed to the same group structure as the macroscopic cross sections. Before they are used in ORIGEN, both the local fluxes and the microscopic cross sections must be collapsed from few-group to one-group.

The disadvantage factors and the microscopic cross sections are interpolated based on the thermal and hydrodynamic core conditions. Both the disadvantage factors and microscopic cross sections use a simple one-dimensional serial interpolation scheme for core conditions. This scheme uses several correction terms for each perturbation to adjust the base case value.

$$\sigma_{i,x}(T_{\text{fuel}}, T_{\text{mod}}, \rho_{\text{mod}}, C_{\text{boron}}, CR) = \sigma_{i,x}(\text{base}) + \sum_{\text{p}}^{\text{perturbations}} \frac{\partial \sigma_{\text{i,x}}}{\partial \text{p}} \Delta \text{p} \tag{4.7}$$

For the base conditions with reflected boundaries, the nuclide concentrations calculated with NESTLE's subregion depletion have been shown to match those computed with the lattice physics concentrations to less than 1% for several nuclides of interest (see Figure 4.1). For thermal and hydraulic conditions outside the base case, the depletion interpolation scheme has not been rigorously verified.

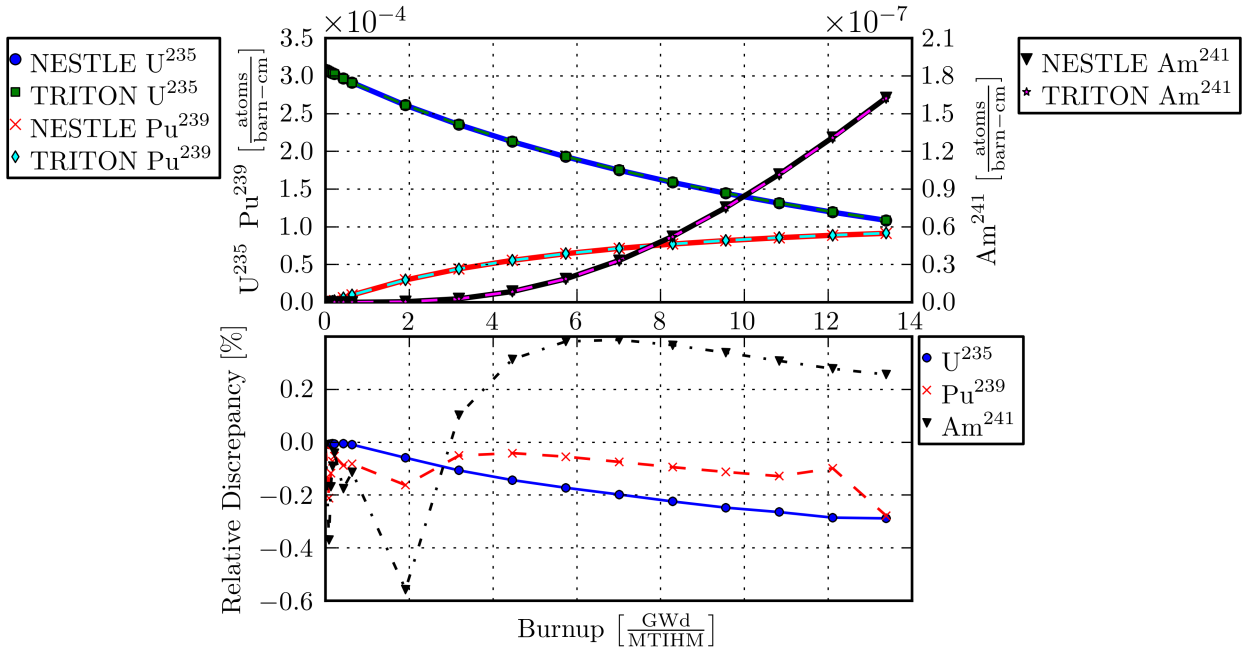

Figure 4.1: [Top] Depletion results comparison of ^{235}U, ^{239}Pu (left axis), and ^{241}Am (right axis) of material 1 between NESTLE-ORIGEN and TRITON-ORIGEN. [Bottom] Relative error in nuclide concentration.

This method does not include changes to the local flux due to the intranodal flux. In a nonhomogeneous finite core, the intranodal flux accounts for the smooth variation (tilting) of the nodal flux across a node due to neighboring nodes. The intranodal flux $\phi_g^{\text{Intra}}(r,\theta)$ is computed during the pin power reconstruction calculation so that lattice physics pin powers (calculated with reflective boundaries) can be corrected to the core conditions. The intranodal power $p^{\text{Intra}}(r,\theta)$ is expressed as in cylindrical coordinates(30):

$$p^{\text{Intra}}(r,\theta) = \sum_{g=1}^{G} \kappa_g \Sigma_{fg}^{\text{Intra}}(r,\theta)\phi_g^{\text{Intra}}(r,\theta) \tag{4.8}$$

where κ_g is the energy per fission for group g. Note that the intranodal flux must be computed during the pin power reconstruction.

$$\phi^{\text{pin}}(r,\theta) = \xi_g^{\text{pin}}(r,\theta)\phi_g^{\text{Intra}}(r,\theta) \tag{4.9}$$

The corrected pin group fluxes and cross sections consistent with the core thermal conditions will be available for post processing of the depleted isotopics of any pin.

4.2 Pin-Level Isotopic Tracking with NESTLE

This section provides preliminary results from the latest NESTLE coupling to ORIGEN API for generalized isotopic tracking as a practical alternative and manageable approach to generating SNF axial isotopic distributions at a fuel pin-level while simulating actual whole-core space- and time-dependent neutronics and thermal-hydraulic conditions.

The approach to implementing isotopic fuel pin depletion in NESTLE relies on few-group microscopic cross sections generated by the SCALE/TRITON depletion sequence. To obtain these cross sections, first the mixture of lattice fuel materials for which homogenized cross sections are calculated must be defined in the TRITON input file. The mixture may consist of any number of materials, including those of a single pin or of a group of pins. Furthermore, multiple homogenized mixtures may be defined for a single lattice, allowing for the depletion of multiple groups of pins in a single NESTLE calculation. During execution, TRITON generates the necessary few-group microscopic cross section set for each mixture defined, which is subsequently imported into NESTLE during the full-core diffusion calculation in order to facilitate depletion by coupling to the ORIGEN sequence in SCALE.

As NESTLE computes the few-group nodal flux solution for the full-core problem, it calls ORIGEN to deplete the homogenized mixture(s) using the computed mixture flux and the mixture cross sections. To obtain the group flux in the depletion mixture (individual fuel rods) from the computed nodal (average) flux, NESTLE applies disadvantage factors to the nodal flux. Disadvantage factors are burnup- and group-dependent and are defined as the ratio of mixture flux to the lattice/nodal flux. Additionally, because ORIGEN requires a one-group flux and a one-group cross section set as input, the few-group data obtained by NESTLE must first be collapsed

into a one-group structure. The output from ORIGEN returned to NESTLE consists of time-dependent isotopic concentrations which are saved by NESTLE and serve as the starting values of the next depletion step. At the conclusion of the NESTLE calculation, the isotopic concentration history for every depletion material is available.

In the case of the VVER-1000 model discussed herein, namely, the AER benchmark, a single depletion mixture was chosen within Assembly 27. The mixture consists of just one fuel material corresponding to six symmetric pins indicated with arrows in the 13 slice of the lattice in Fig. 4.2. This assembly was located near the central region of the core. Because the NESTLE model divides the core into 20 axial segments, the assembly consists of 20 depletion materials. There were 328 depletion steps performed in this calculation, requiring 6,560 calls to ORIGEN.

The results shown in Fig. 4.3 show the axial profiles of isotopic concentration for ^{235}U and ^{239}Pu, respectively, as a function of total days (not EFPD). These results demonstrate what is potentially a powerful feature that would enable analysts to calculate isotopic concentrations on any isotope tracked by ORIGEN for any selected fuel rod or section of a fuel rod.

Control Rod Depletion Using ORIGEN

Control rod depletion capabilities were implemented in NESTLE (29). After the previous integration with ORIGEN, depletion of movable control rod materials was an extension. This required NESTLE to track the shifting locations of control rod materials throughout the fuel cycle and treat cross sections appropriately at each burnup step based on the rods' local surroundings. Tracking of the control rod materials has been implemented in such a way as to allow the user as much flexibility as possible in defining the control rod material boundary.

Results from the control rod depletion calculation with NESTLE demonstrate a feature under development with the potential to provide the unique capability of accurately capturing history effects in depletion of control rods. Work will continue

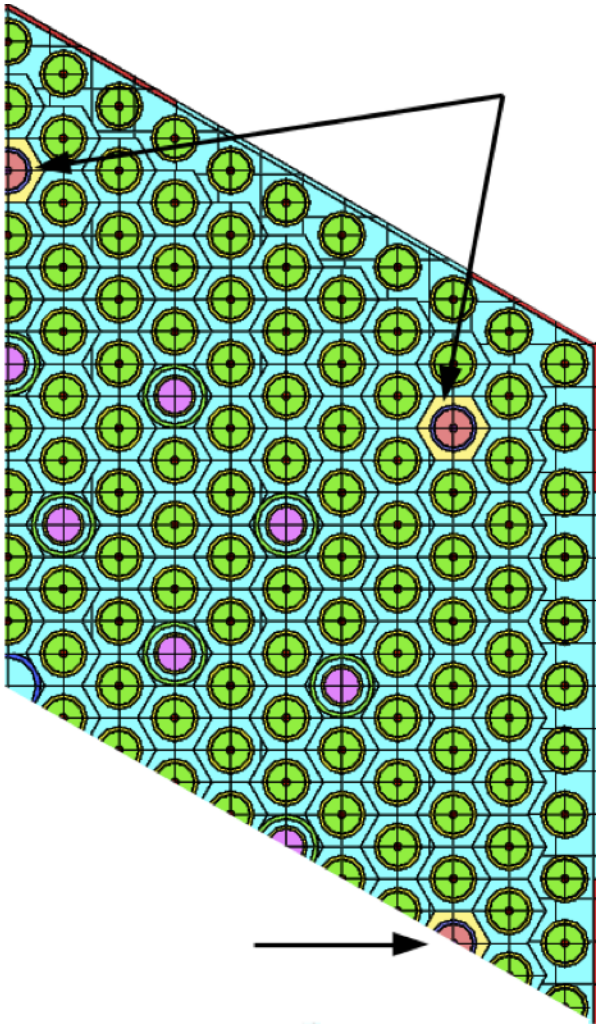

Figure 4.2: 13 slice of lattice type 22au (Assembly 27) with selected pins for depletion indicated by arrows.

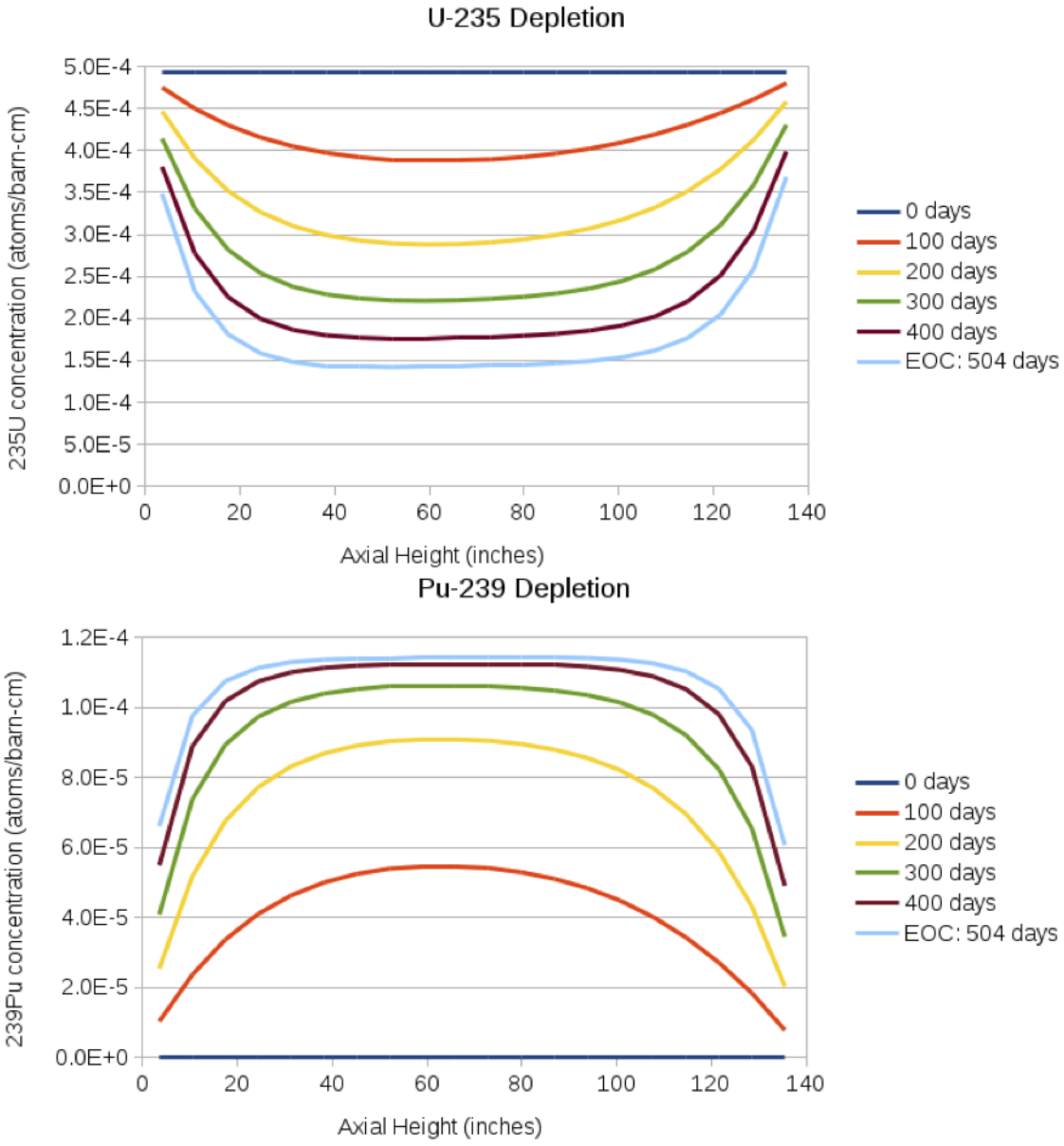

Figure 4.3: Time-dependent axial profile of isotope concentration in selected pins of lattice type 22au [Top] ^{235}U, [Bottom] ^{239}Pu.

in this area with independent code-to-code verification of NESTLE results and the development of a feedback mechanism in order to quantify the effect of depleting control rods on the fuel cycle

4.3 Code Development for Microscopic Depletion

4.3.1 Changes to NEWT for Microscopic Depletion

NEWT outputs many data that can be used for 2D reactor analysis. It did not output few group microscopic cross section data for homogenized regions (with the exceptions of ^{135}Xe and ^{149}Sm). The source code of the 2D transport code NEWT in SCALEv6.2b4 was changed so that the nuclide microscopic cross sections would be output for use as input to NESTLE.

To use the NESTLE microscopic depletion features, few-group cross sections are required for several nuclides including: ^{234}U, ^{235}U, ^{236}U, ^{238}U, ^{239}Pu, ^{240}Pu, ^{241}Pu, ^{242}Pu, ^{241}Am. The cross sections are for the absorption and fission processes for each nuclide at each burnup step and each branch case. Other data are also required for each isotope including the number densities, the delayed neutron yields, the prompt neutron spectra, the transient fission product yields, the number of neutrons per fission (ν), and the energy released per fission (κ).

Other data are required that are not specific to the tracked actinides. Pseudo-nuclides (lumped fission products and a burnable absorber) are also tracked and absorption cross sections for these pseudo-nuclides must be input. The microscopic depletion model also requires the few group 'background' absorption cross sections for all nuclides not included in the tracked nuclides. Finally, the delayed neutron importances and the lumped fission product yields are also required to use the microscopic depletion model.

The NEWT subroutine *cellwt2d* was modified so that when the individual nuclide data were being homogenized and condensed, the data would be printed to the NEWT output file. Although the tracked actinide data is of primary importance, data from every nuclide used in the transport solve is output so that derived data can be produced in post processing. For example, the 'background' absorption cross sections must be computed once the fuel nuclides are separated from the non-fuel nuclides (such as those present in the coolant and structural materials). This post-processing of data is handled by a collection of Python packages that produce a NESTLE cross section file.

4.3.2 Python Packages to Produce NESTLE Cross Section Data Files

A number of Python packages were developed to read the output files produced by the modified NEWT output files and produce files suitable as input for NESTLE. These Python packages perform the post-processing necessary to produce the data required by NESTLE and in the expected format.

TRITON produces a single output file that contains all of the data from each depletion step and all branch cases. In normal circumstances this output file will be large (> 50 MB), but with the additional data produced by the modified NEWT subroutine, the output file becomes very large (> 250 MB). The Python packages first read in the large output file and break it into sections for each branch case at each burnup step. The Python code determines which nuclides will be used in actinide nuclides, pseudo nuclides, and background nuclides. Few group cross section values are produced by homogenizing the materials, including possibly multiple fuel nuclides, appropriately using the multi-group material fluxes. The cross sections from all branch are fitted using polynomials to generate coefficients used as input in the microscopic cross section data files.

The Python packages also read a previously existing macroscopic cross section file. This is done in part to produce a microscopic cross section data file that is consistent with the macroscopic cross section file. Additionally, some data available in a macroscopic cross section data file can be used directly in the microscopic cross section data file, so repetitive data processing is avoided by using an existing macroscopic file.

4.3.3 Lumped Pseudo-Nuclides

A pseudo-nuclide is a surrogate of combined nuclide data that behaves similarly to a single physical nuclide. The purpose of using a pseudo-nuclide is to reduce or eliminate the number of calculations performed for the constituent nuclides. For example, a burnable absorber pseudo-nuclide for gadolinium could consist of the three absorptive isotopes ^{155}Gd, ^{156}Gd, ^{157}Gd. NESTLE's microscopic depletion model uses lumped pseudo-nuclides for a burnable absorber and for fission products. The methodology for creating pseudo nuclides is described in (31). To create an pseudo-nuclide effective microscopic cross section σ_{eff}, the macroscopic cross section is divided by an effective number density N_{eff}:

$$\sigma_{\text{eff}} = \frac{\sum_{i=1}^{n} N_i \sigma_i}{N_{\text{eff}}} \tag{4.10}$$

The effective number density is the weighted sum of the constituent number densities:

$$N_{\text{eff}} = \sum_{i=1}^{n} w_i N_i \tag{4.11}$$

where the weights are determined from the yield matrix.

$$w(j) - \sum_{i=1}^{n} w(i) * y(i,j) = 1 \tag{4.12}$$

The yield matrix is a square matrix that expresses the fraction produced by nuclide j of nuclide i through neutron absorption. For example, in the case of the burnable poison consisting of the three gadolinium isotopes, the yield matrix would be:

$$Y = \begin{bmatrix} {}^{155}\mathrm{Gd} \rightarrow {}^{155}\mathrm{Gd} & {}^{156}\mathrm{Gd} \rightarrow {}^{155}\mathrm{Gd} & {}^{157}\mathrm{Gd} \rightarrow {}^{155}\mathrm{Gd} \\ {}^{155}\mathrm{Gd} \rightarrow {}^{156}\mathrm{Gd} & {}^{156}\mathrm{Gd} \rightarrow {}^{156}\mathrm{Gd} & {}^{157}\mathrm{Gd} \rightarrow {}^{156}\mathrm{Gd} \\ {}^{155}\mathrm{Gd} \rightarrow {}^{157}\mathrm{Gd} & {}^{156}\mathrm{Gd} \rightarrow {}^{157}\mathrm{Gd} & {}^{157}\mathrm{Gd} \rightarrow {}^{157}\mathrm{Gd} \end{bmatrix} = \begin{bmatrix} 0 & 0 & 0 \\ 1 & 0 & 0 \\ 0 & 1 & 0 \end{bmatrix}$$

In this case the weights would be $w = 3$ for ^{155}Gd, $w = 2$ for ^{156}Gd, and $w = 1$ for ^{157}Gd. The physical interpretation of this is that each nuclide in the effective number density is weighted by the number of neutrons that can be absorbed by it and all other descendent nuclides contained in the pseudo-nuclide.

The lumped fission product pseudo-nuclide consists of all nuclides that are not included in the tracked actinides, the burnable absorber nuclide, ^{135}Xe, ^{149}Sm, or those nuclides in the background absorption.

4.3.4 Flux Normalization for Non-Local Fission Power

The NESTLE microscopic depletion model requires that the energy released per fission κ be input for each nuclide. The homogenized few-group fission cross sections are input for each fisssionable nuclide. The macroscopic cross section for fission power $\kappa\Sigma_f$ is computed from these microscopic data and the number densities of the fissionable nuclides. The macroscopic cross section for fission power is used to scale the group flux magnitude using the input power P:

$$\sum_{g=1}^{G} \phi_g \kappa \Sigma_{f,g} = P \tag{4.13}$$

In NESTLE's macroscopic model the group fluxes are only output of the calculation, but in the microscopic model the flux is used to deplete the tracked nuclides over the depletion step. Therefore, the flux magnitude is very important to

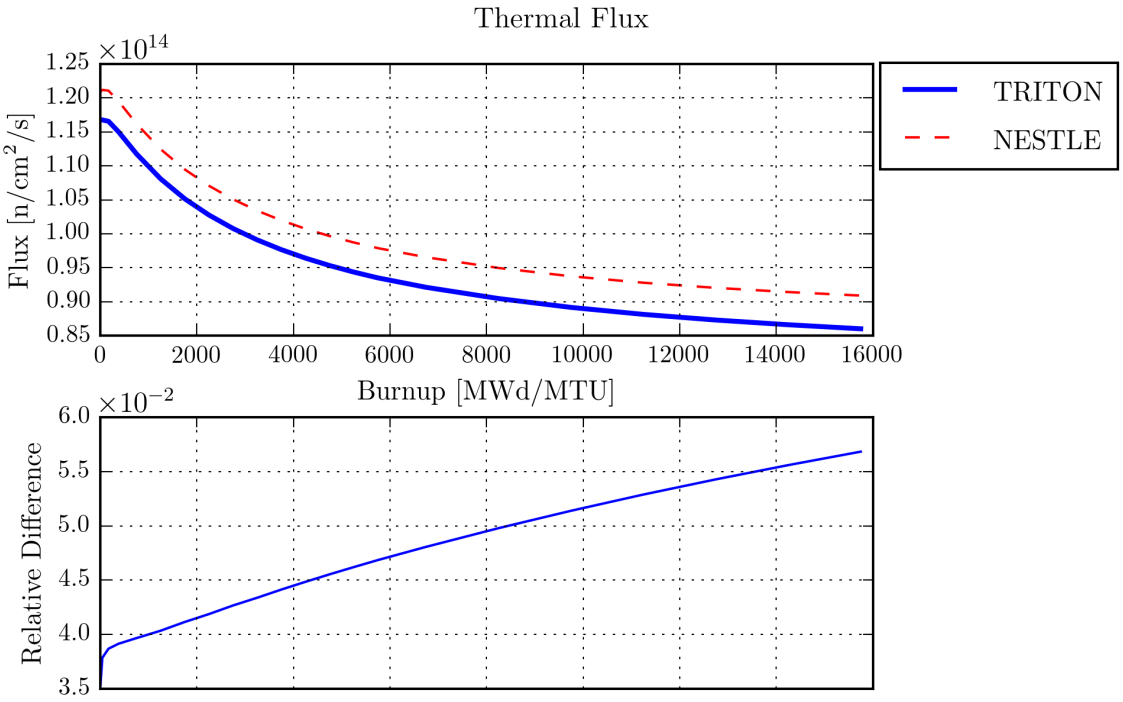

Figure 4.4: The thermal fluxes by TRITON and NESTLE. There is a significant discrepancy due to incorrect flux scaling that does not account for gamma-ray and neutron interactions in the coolant and structural materials.

obtaining the correct nuclide number densities in the microscopic model. Fission energy is mostly deposited at the site of fission, but additional energy may be deposited far from the fission site due to gamma-ray and neutron interactions in the coolant and structural materials. This additional power is relatively small but not insignificant (in the range of about 5% of the total power).

Initial uses of NESTLE's microscopic depletion model showed significant discrepancies with the fluxes computed by the lattice code TRITON. Figure 4.4 shows the differences between the thermal fluxes as computed by NESTLE and that computed by TRITON. The discrepancies in the fluxes caused significant errors in the calculation of the nuclide number densities during depletion.

In order to compute similar number densities to those calculated by TRITON, NESTLE required additional data to scale the flux appropriately. This additional data is the macroscopic cross section for non-local fission power $\kappa_{NL}\Sigma_{NL}$.

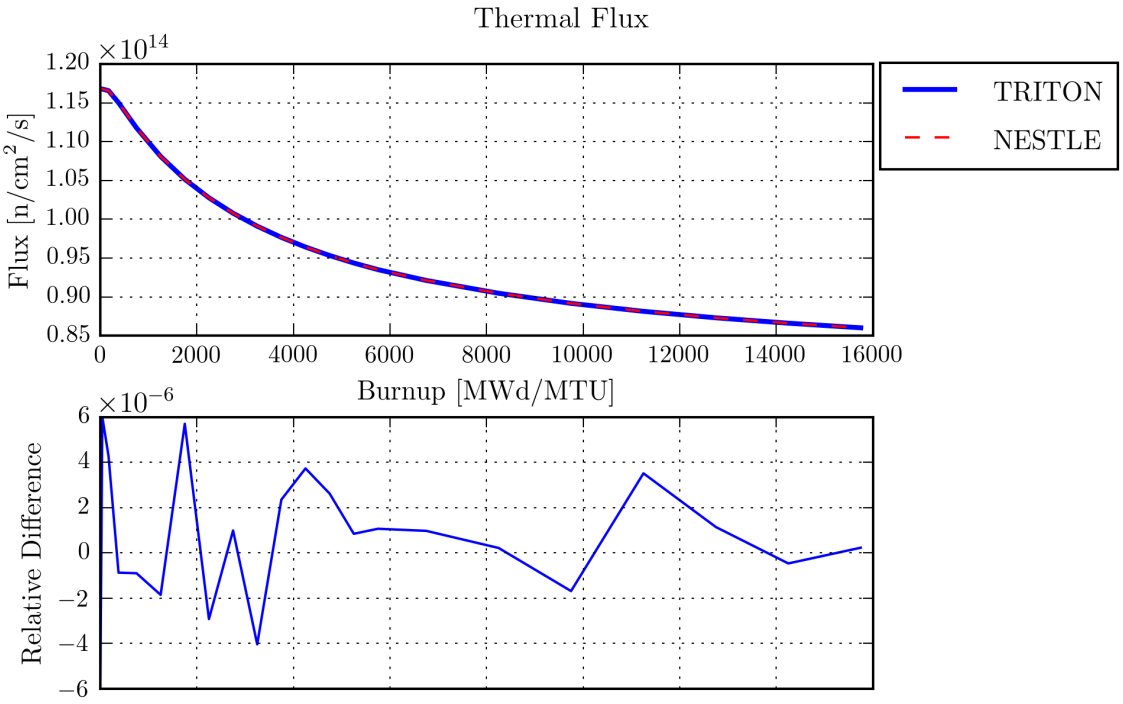

Figure 4.5: The thermal fluxes by TRITON and NESTLE with the additional $\kappa_{NL}\Sigma_{NL}$ data.

This data is not readily output from TRITON, but it can be computed by assuming the the flux magnitude as output by TRITON and correcting the NESTLE flux magnitude accordingly:

$$\kappa_{NL}\Sigma_{NL} = \kappa\Sigma_{f,g}\left(\frac{\phi_{g,\text{NESTLE}}}{\phi_{g,\text{TRITON}}} - 1\right) \tag{4.14}$$

The NESTLE source code was modified to accept the non-local fission power terms as input and use them to correct the flux scaling. The $\kappa_{NL}\Sigma_{NL}$ term must be computed and input by the user for each lattice in the NESTLE cross section file. After accounting for the additional non-local fission power, the fluxes output by NESTLE are in good agreement (on the order of 10^{-6} relative discrepancy) with those produced by TRITON.

Table 4.1: Branch conditions

Branch	Fuel Temperature K	Coolant Temperature K	Coolant Density g/cc	Boron Concentration ppm	Rod State None
0	1005.0	578.0	0.7167	525.0	Out
1	1005.0	578.0	0.7167	525.0	In
2	550.0	578.0	0.7167	525.0	Out
3	550.0	578.0	0.7167	525.0	In
4	2500.0	578.0	0.7167	525.0	Out
5	2500.0	578.0	0.7167	525.0	In
6	1005.0	550.0	0.7167	525.0	Out
7	1005.0	550.0	0.7167	525.0	In
8	1005.0	619.0	0.7167	525.0	Out
9	1005.0	619.0	0.7167	525.0	In
10	1005.0	578.0	0.7700	525.0	Out
11	1005.0	578.0	0.7700	525.0	In
12	1005.0	578.0	0.5910	525.0	Out
13	1005.0	578.0	0.5910	525.0	In
14	1005.0	578.0	0.7167	0.0	Out
15	1005.0	578.0	0.7167	0.0	In
16	1005.0	578.0	0.7167	1675.0	Out
17	1005.0	578.0	0.7167	1675.0	In

4.4 History Effects

4.4.1 History Effects Impact on Nuclide Concentration

The magnitude of the history effect for each nuclide for each branch (shown in Table 4.1) was computed by using TRITON. Typically for lattice physics calculations, depletion is only performed along the base case. Branch cases consist of neutron transport followed by homogenization, condensation, and computation of lattice parameters without further depletion. By depleting at the branch conditions, the nuclide compositions at each burnup state can be compared to the base case. For example, if branches 0 and 10 are compared, the history effect of high moderator density can be computed. For the case of ^{239}Pu, this effect will be similar to the effect shown in Figure 3.5.

The relative differences for each of the nuclides are shown in Figures 4.6 through 4.11 for the 30av5 lattice. This lattice type was selected because it had an average enrichment similar to that of the entire core. The history effects for the other lattices are of similar magnitude. In these figures, the nuclide number densities computed at the branch conditions are compared to the number densities computed at the base conditions.

Figures 4.6 through 4.11 demonstrate the envelope of variation for the history effects for the branch perturbations. Depending on the nuclide, the branch conditions, and the burnup, these effects can be can be greater than 30%. In the case of ^{235}U, which is present in the initial fresh fuel, the relative difference in the nuclide concentration is less than 1% until 5 GWd/MTU, but it continues to expand as the burnup continues. For ^{239}Pu, which is not initially present in the fresh fuel, the relative difference in nuclide concentration can be large from the start of the cycle. Although, these relative differences in ^{239}Pu concentration appear to stay relatively constant throughout the depletion interval. This behavior is noticeably different from the other plutonium isotopes (^{240}Pu, ^{241}Pu, and ^{242}Pu) which have largef relative differences near the beginning of the cycle, but the differences decrease as the burnup continues.

4.4.2 Microscopic Depletion Mitigation of History Effects

By using NESTLE's microscopic depletion model instead of the macroscopic depletion model, the history effects can be mitigated. The effects cannot be totally eliminated because the microscopic cross section data is obtained from the base case depletion only. The following plots demonstrate how effective the microscopic depletion model is in reducing the errors in nuclide concentrations. The plots show the relative error in nuclide number densities between the NESTLE computed branch case value and the corresponding TRITON branch case. As can be seen from the plots, the history effect is reduced to errors often less than 5% for the important fissionable nuclides.

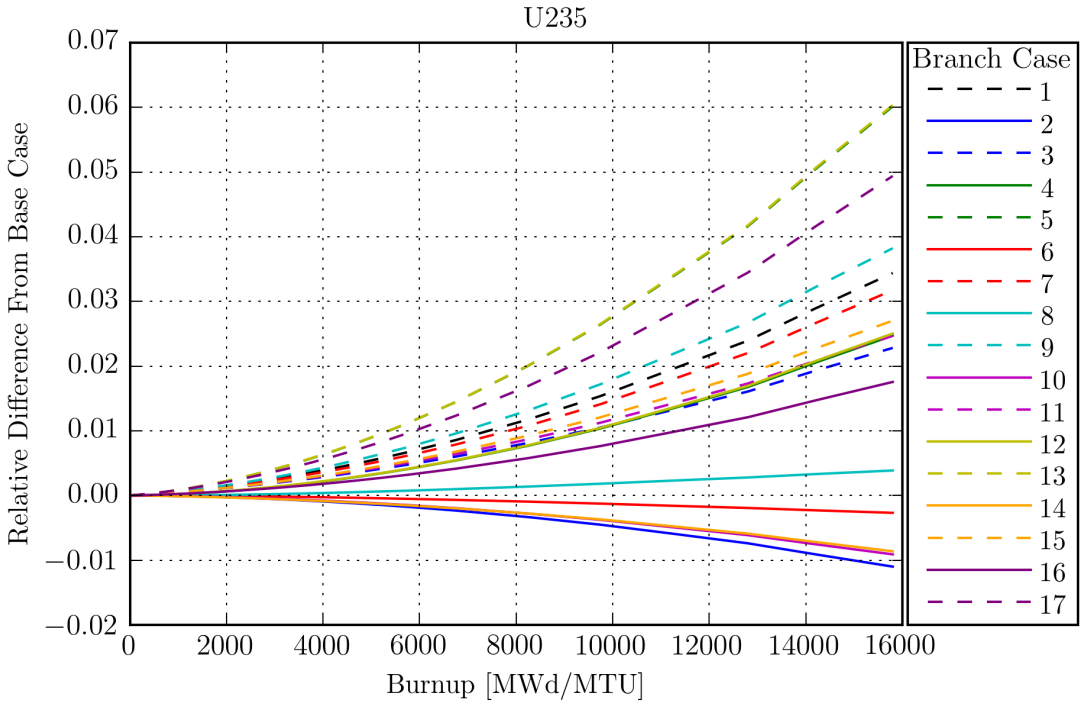

Figure 4.6: The history effects of branch conditions for ^{235}U in the 30av5 lattice.

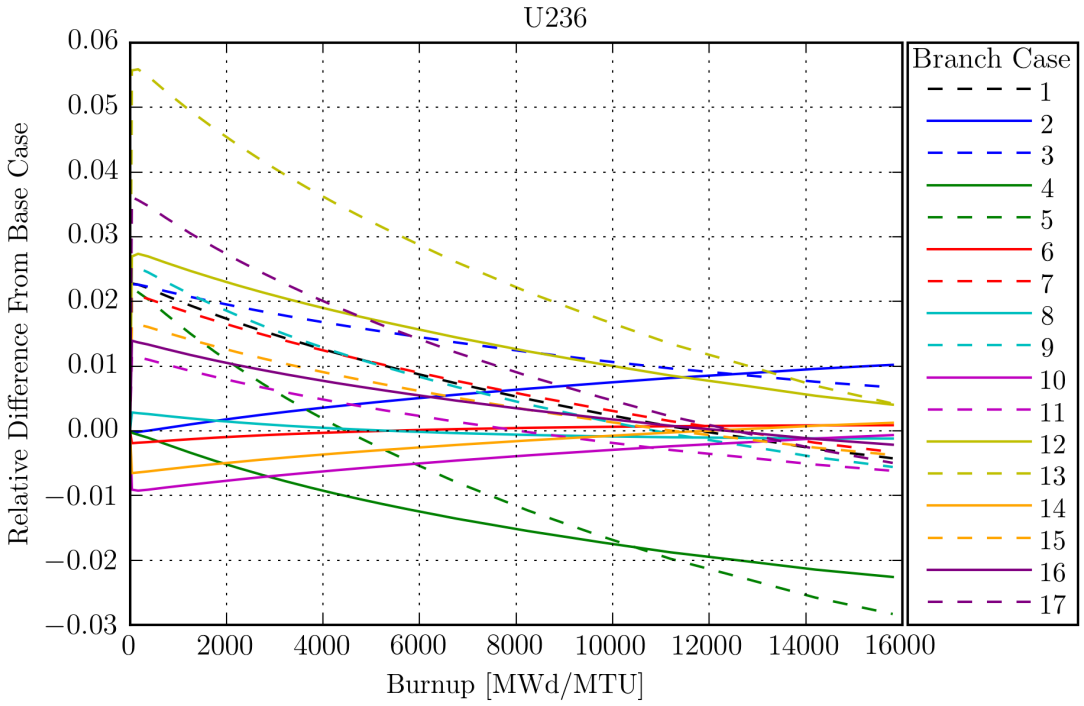

Figure 4.7: The history effects of branch conditions for ^{236}U in the 30av5 lattice.

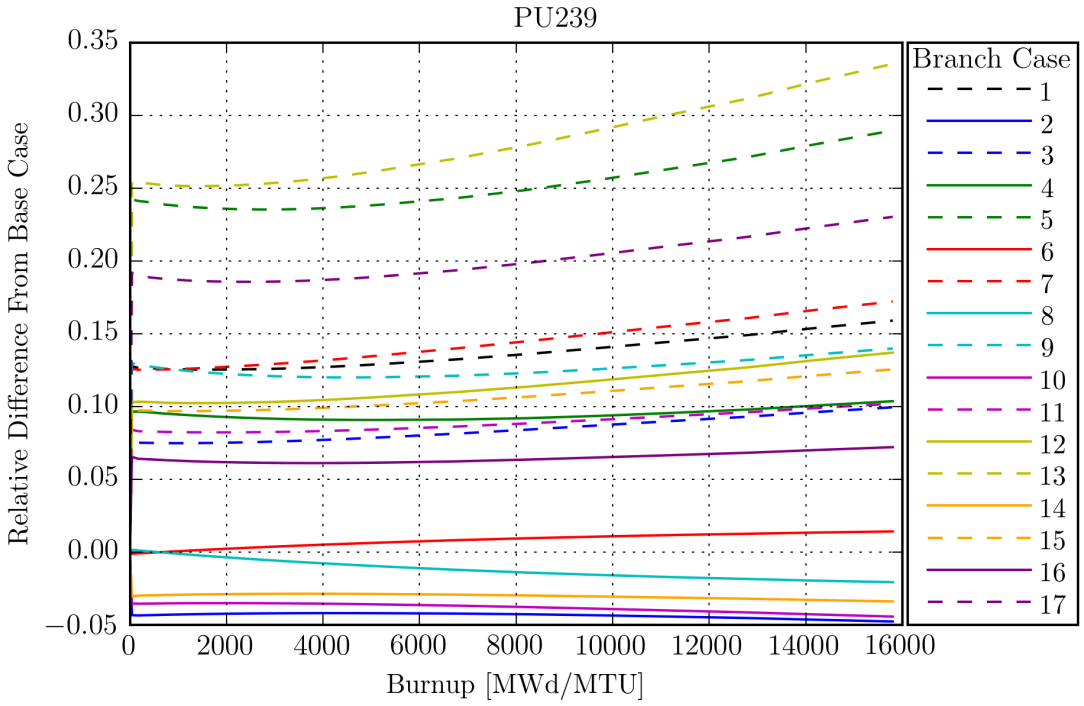

Figure 4.8: The history effects of branch conditions for ^{239}Pu in the 30av5 lattice.

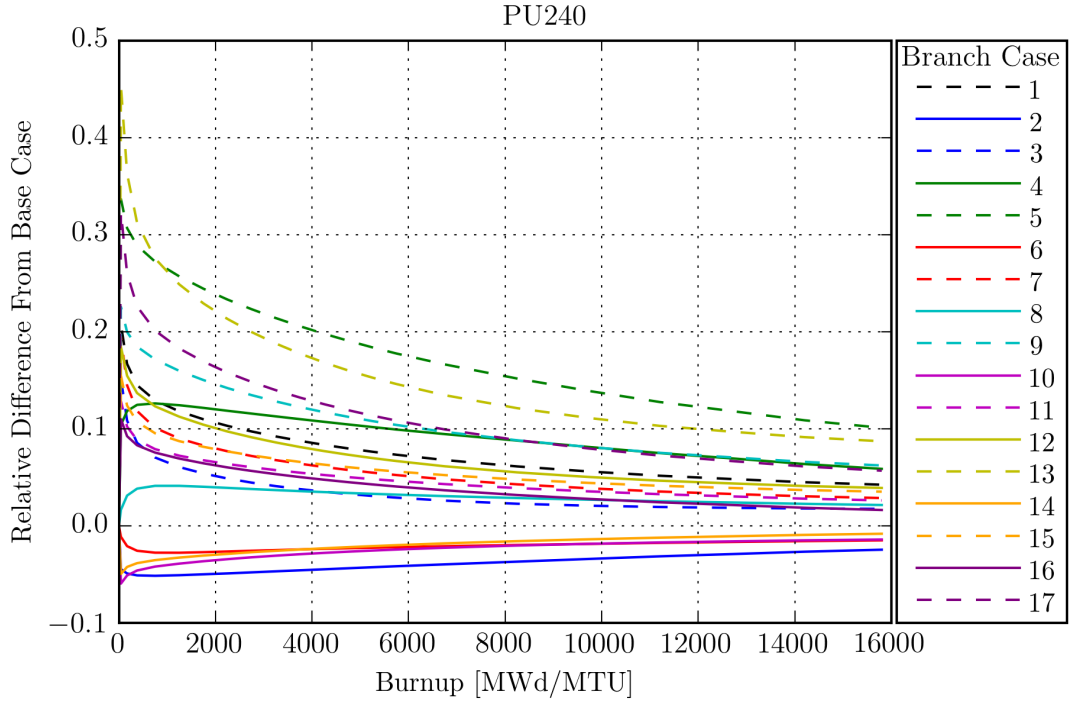

Figure 4.9: The history effects of branch conditions for ^{240}Pu in the 30av5 lattice.

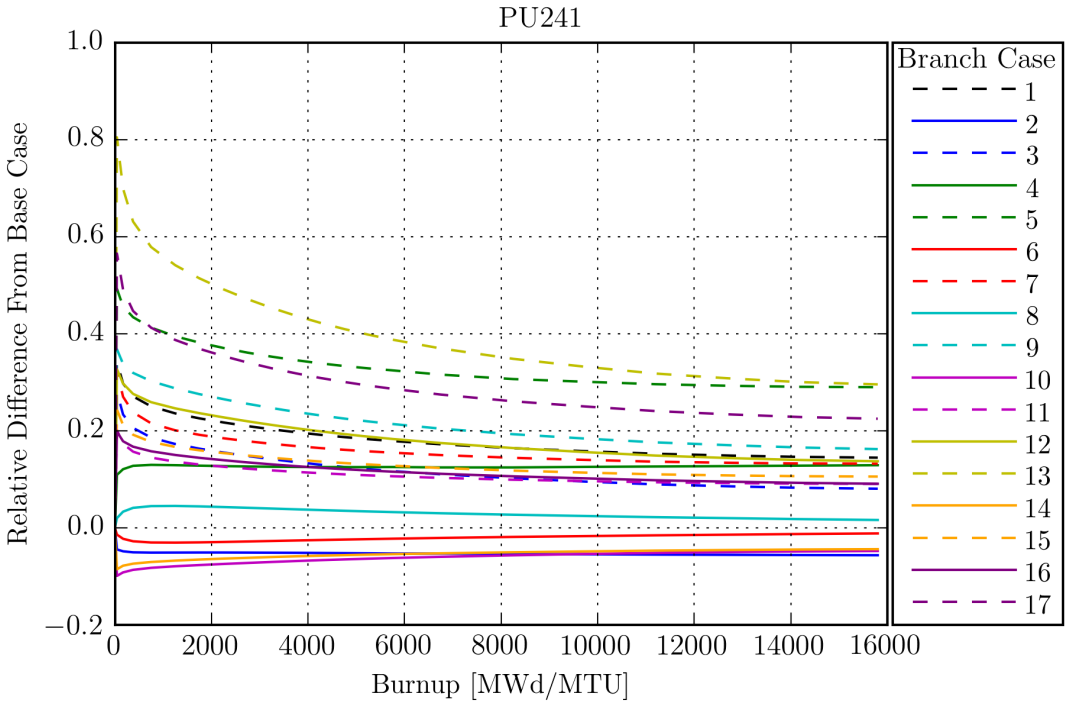

Figure 4.10: The history effects of branch conditions for ^{241}Pu in the 30av5 lattice.

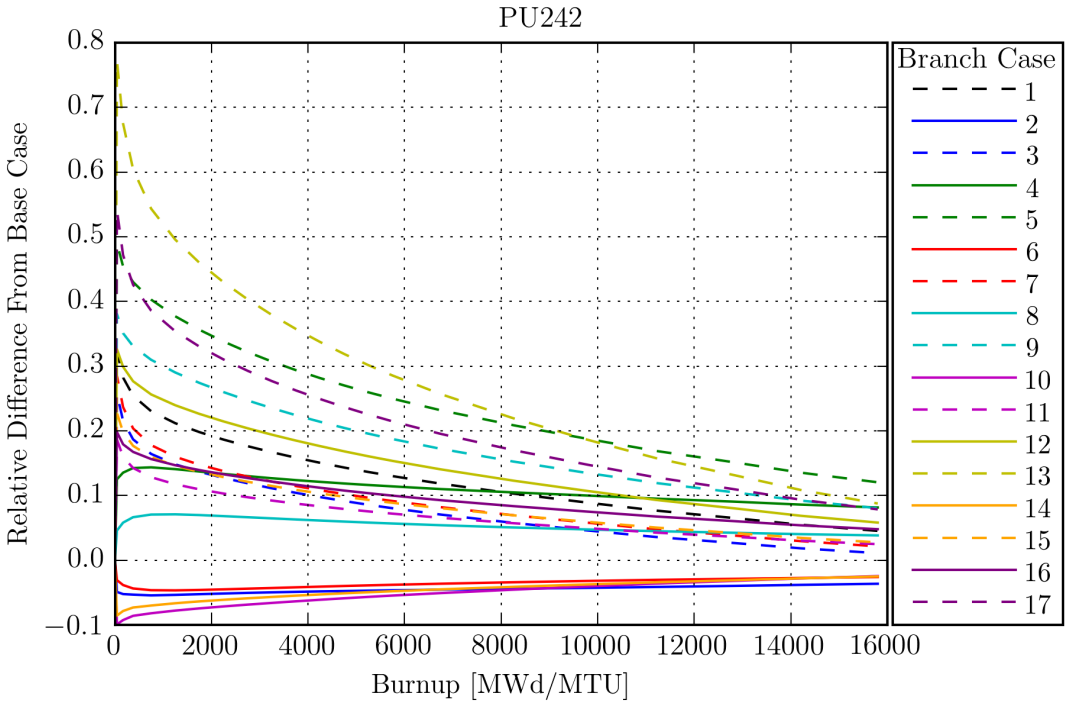

Figure 4.11: The history effects of branch conditions for ^{242}Pu in the 30av5 lattice.

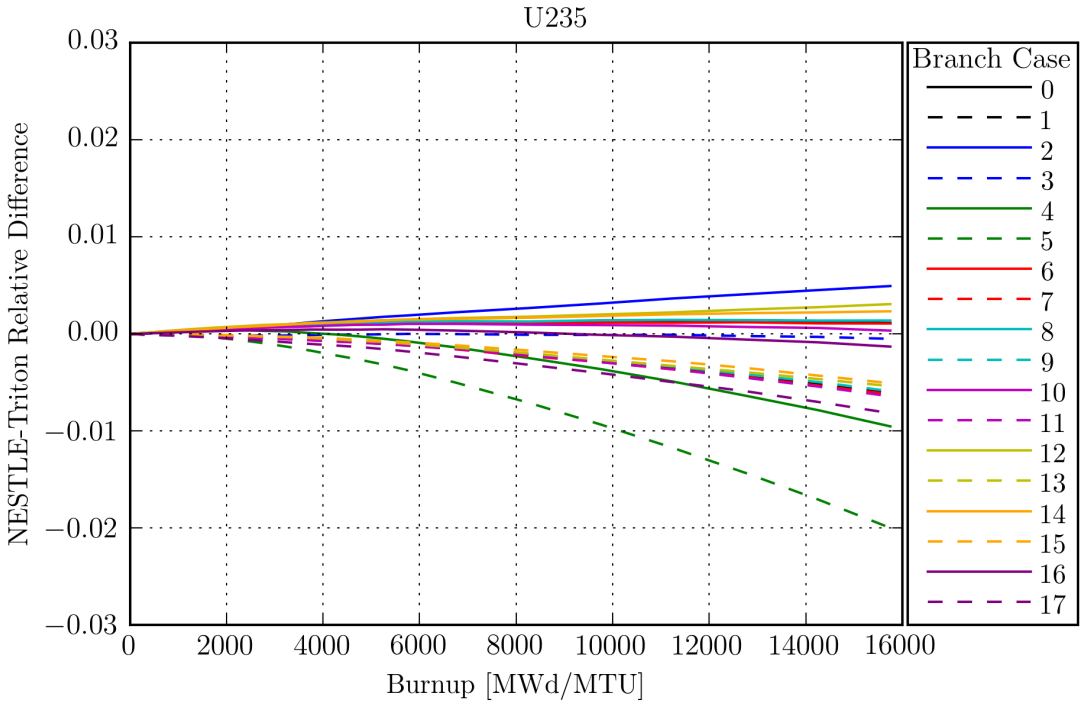

Figure 4.12: The relative differences between the NESTLE and TRITON computed nuclide number densities for ^{235}U in each branch for the 30av5 lattice.

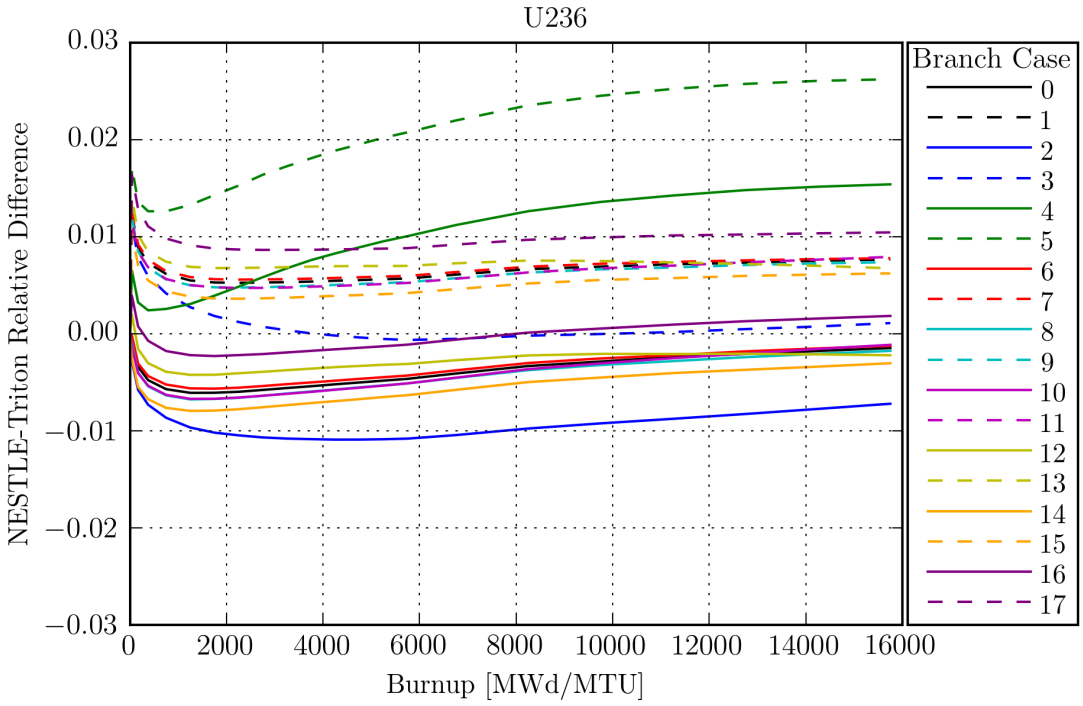

Figure 4.13: The relative differences between the NESTLE and TRITON computed nuclide number densities for ^{236}U in each branch for the 30av5 lattice.

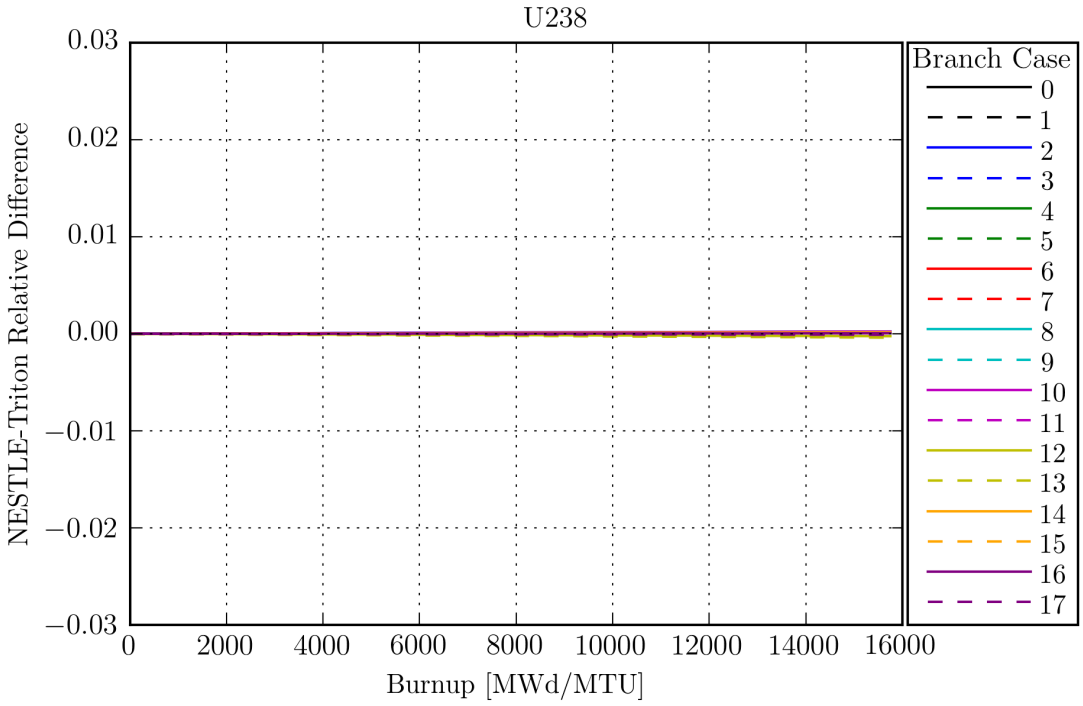

Figure 4.14: The relative differences between the NESTLE and TRITON computed nuclide number densities for ^{238}U in each branch for the 30av5 lattice.

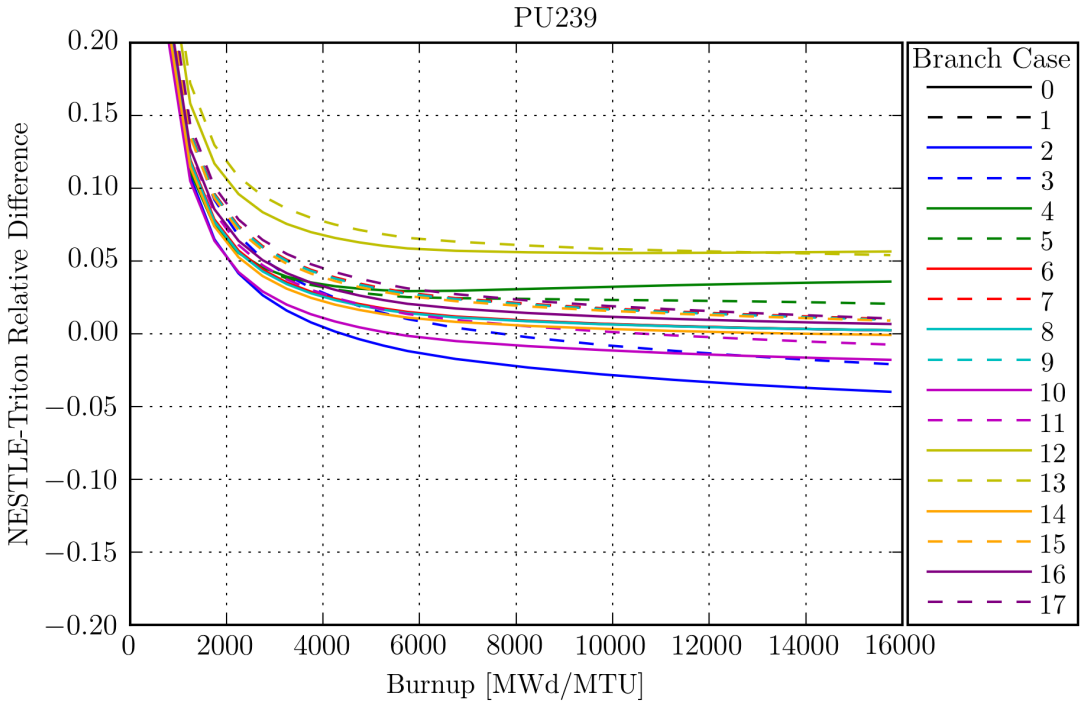

Figure 4.15: The relative differences between the NESTLE and TRITON computed nuclide number densities for ^{239}Pu in each branch for the 30av5 lattice.

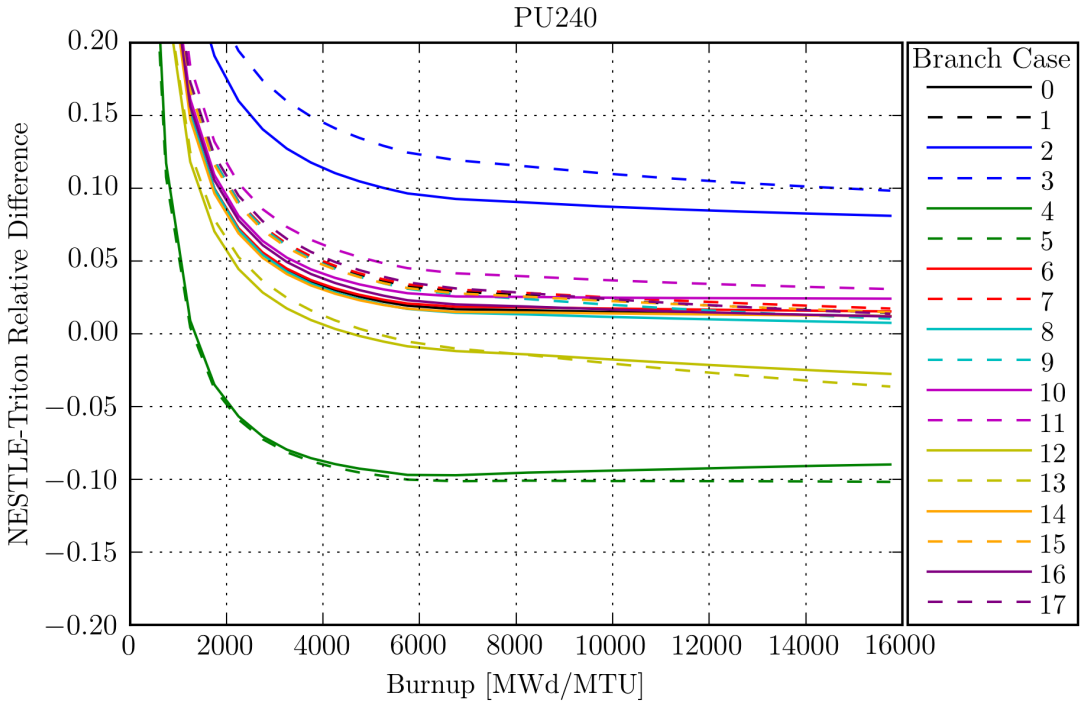

Figure 4.16: The relative differences between the NESTLE and TRITON computed nuclide number densities for ^{240}Pu in each branch for the 30av5 lattice.

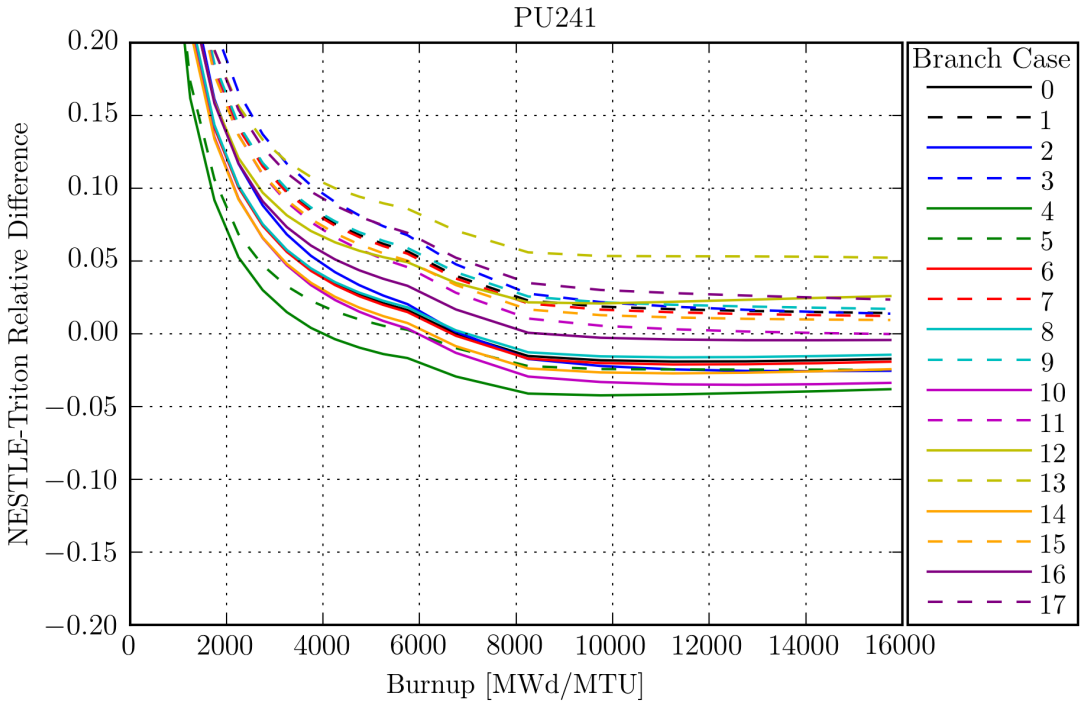

Figure 4.17: The relative differences between the NESTLE and TRITON computed nuclide number densities for ^{241}Pu in each branch for the 30av5 lattice.

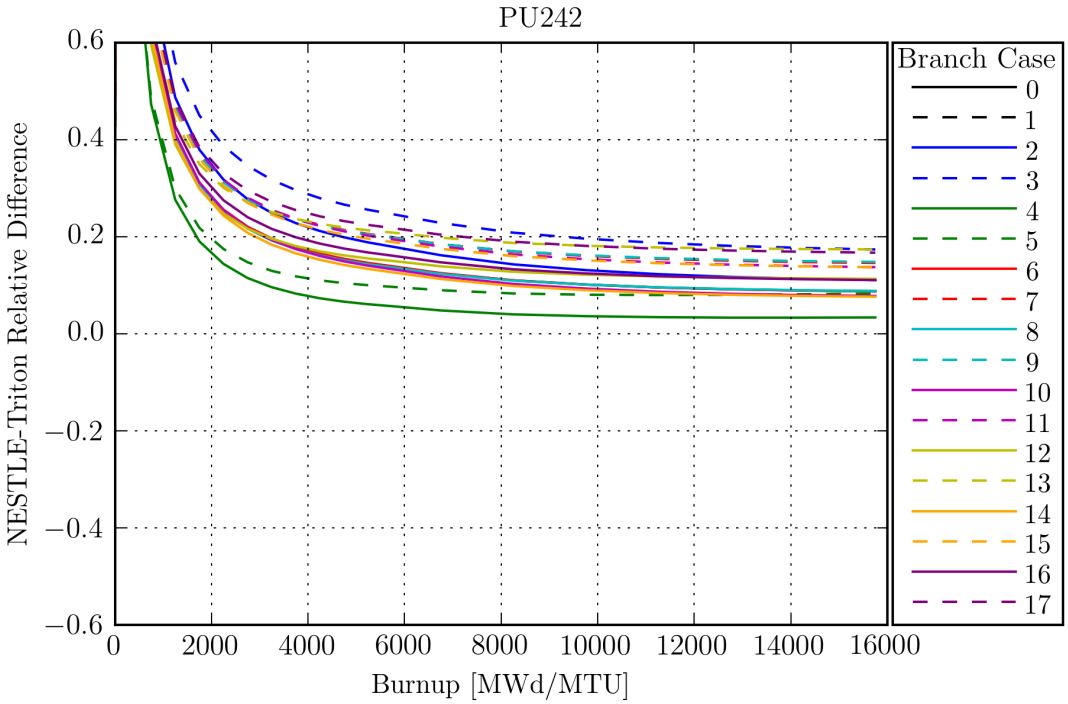

Figure 4.18: The relative differences between the NESTLE and TRITON computed nuclide number densities for ^{242}Pu in each branch for the 30av5 lattice.

Chapter 5

Verification of Pin Power Reconstruction Methods in NESTLE

5.1 Pin Power Reconstruction

NESTLE can be used to model either Cartesian geometries (for use with typical PWR, BWR fuel assemblies) or hexagonal geometries (for use with VVER and other triangularly pitched fuel assemblies). NESTLE is unusual in that the pin power reconstruction option historically has only been available in hexagonal geometries. Cartesian pin power reconstruction is currently under development. The method of solution of the nodal equations for hexagonal geometries uses a conformal mapping technique proposed by Chao and Tsoulfanidis (32).

5.1.1 Intranodal Power

As is typical of many nodal core simulators, NESTLE uses the power (in contrast to the flux) form factors f as computed by the lattice code. These form factors are multiplied by the intranodal power p^{Intra} to determine the reconstructed pin power p:

$$p(r,\theta) = p^{\text{Intra}}(r,\theta) f(r,\theta) \tag{5.1}$$

where the terms are functions of cylindrical coordinates r and θ with the origin at the the node center. The intranodal power is computed using the intranodal group fluxes ϕ_g^{Intra} and the group fission energy per unit path length $\kappa\Sigma_{\text{f}g}^{\text{Intra}}$:

$$p^{\text{Intra}}(r,\theta) = \sum_{g=1}^{2} \kappa\Sigma_{\text{f}g}^{\text{Intra}}(r,\theta)\phi_g^{\text{Intra}}(r,\theta) \tag{5.2}$$

Note that NESTLE uses a two-group formulation when computing the intranodal power. If the general nodal diffusion problem uses more than two energy groups, the fluxes and cross sections are first collapsed to two groups. To compute the intranodal power, the two-dimensional functional forms must be determined for both the intranodal group fluxes and the fission group cross sections.

5.1.2 Intranodal Flux

The two-group neutron diffusion equation over the homogeneous node can be written:

$$\overline{\overline{\nabla^2}} \begin{bmatrix} \phi_1 \\ \phi_2 \end{bmatrix} - \begin{bmatrix} \frac{\Sigma_{\text{R}1} - \chi_1\nu\Sigma_{\text{f}1}}{D_1} & \frac{-\chi_1\nu\Sigma_{\text{f}2}}{D_1} \\ \frac{-\Sigma_{\text{s}12} - \chi_2\nu\Sigma_{\text{f}1}}{D_2} & \frac{\Sigma_{\text{R}2} - \chi_2\nu\Sigma_{\text{f}2}}{D_2} \end{bmatrix} \begin{bmatrix} \phi_1 \\ \phi_2 \end{bmatrix} = 0 \tag{5.3}$$

with the number of neutrons per fission ν, group removal cross sections $\Sigma_{\mathrm{R}g}$, group scattering cross sections $\Sigma_{sgg'}$, group absorption cross sections Σ_{ag}, and group diffusion coefficient D_g. Equation (5.3) can be cast into diagonal form:

$$\overline{\overline{\nabla^2}} \begin{bmatrix} \Phi_u \\ \Phi_v \end{bmatrix} - \begin{bmatrix} u^2 & 0 \\ 0 & -v^2 \end{bmatrix} \begin{bmatrix} \Phi_u \\ \Phi_v \end{bmatrix} = 0 \tag{5.4}$$

where λ_g are the eigenvalues and $u^2 = -\lambda_1$ and $v^2 = \lambda_2$.

As shown by Chao and Shatil1a (33), the general solutions to equation (5.4) are linear combinations of plane waves along all directions. NESTLE performs numeric integration of the solution equations:

$$\begin{aligned} \Phi_u(r,\theta) = \int_0^{2\pi} & [A_u(\alpha)\sin(ur\cos(\theta-\alpha))+ \\ & B_u(\alpha)\cos(ur\cos(\theta-\alpha))]\ d\alpha+ \\ & \int_0^{2\pi} [C_u(\alpha)\cos(ur\sin(\theta-\alpha)) \\ & + D_u(\alpha)\sin(ur\sin(\theta-\alpha))]\ d\alpha \end{aligned} \tag{5.5}$$

$$\begin{aligned} \Phi_v(r,\theta) = \int_0^{2\pi} & [A_v(\alpha)\sinh(vr\cos(\theta-\alpha))+ \\ & B_v(\alpha)\cos(vr\cosh(\theta-\alpha))]\ d\alpha+ \\ & \int_0^{2\pi} [C_v(\alpha)\cosh(vr\sin(\theta-\alpha)) \\ & + D_v(\alpha)\sinh(vr\sin(\theta-\alpha))]\ d\alpha \end{aligned} \tag{5.6}$$

by determining the direction-dependent superposition coefficients A,B,C,D along three discrete angles α. To determine the values of the superposition coefficients, twelve constraints are used for each group: six corner fluxes and six surface fluxes along the node perimeter. To determine these values, six corner point discontinuity factor (CDF) and six assembly discontinuity factor (ADF) are input from the lattice

physics calculation. These discontinuity factors are defined at a point or along a surface in the usual way $d = \frac{\phi_{Hetero}}{\phi_{Homog}}$ and provided as input from the lattice physics calculation.

For each of the six hexagonal surfaces of length R, the flux along the surface is approximated by a quadratic polynomial:

$$\phi_g(s) = a_0 + a_1 s + a_2 s^2 \qquad -R/2 < s < R/2 \tag{5.7}$$

CDFs at $-R/2$ and $R/2$ determine $\phi_g(-R/2)$ and $\phi_g(R/2)$, while the surface ADF determines the average flux value along the surface. These constraints are sufficient to determine the a_n along each hexagonal surface.

The flux in the region of each of the hexagon corners is approximated by a polynomial function:

$$\begin{aligned}\phi_g(x,y) =& c_{0g} + c_{1g}(x - x_c) + c_{2g}(y - y_c) + c_{3g}(x - x_c)^2 + \\ & c_{4g}(y - y_C)^2 + c_{5g}(x - x_C)(y - y_c)\end{aligned} \tag{5.8}$$

where the corner is located at (x_c, y_c). The c_n are fitted to preserve both the volume averaged fluxes of the three nodes surrounding the corner and the average fluxes along each surface composing the corner, both of which are determined by the nodal solution and using the surface ADFs. The CDF at the corner determines the flux at (x_c, y_c) producing a continuous flux. Equations (5.7) and (5.8) are used at each of the six corners to approximate the integrals of the direction-dependent superposition coefficients in equations (5.5) and (5.6).

5.1.3 Intranodal Cross Section

To solve for the intranodal power in equation (5.2), the spatial variation of the fission energy per unit path length, $\kappa\Sigma_{fg}$, must also be determined. The cross section function used in NESTLE is the same as that presented by Chao and Shatil1a (33). The node

averaged cross section and the cross section along each of the six surfaces are used to determine the intranodal cross section:

$$\kappa\Sigma_{fg}(r,\theta) = C_{0_g} + \sum_{n=1}^{3} C_{1n_g}\gamma_n + \sum_{n=1}^{3} C_{2n_g}\gamma_n^2 + C_{3_g}(-\gamma_1^3 + \gamma_2^3 - \gamma_3^3) \tag{5.9}$$

where:

$$\gamma_n = r\cos(\theta - \alpha_n) \tag{5.10}$$

$$\alpha_n = (n-1)(\pi/3) \tag{5.11}$$

Although there are only seven average cross sections (one volume and six surface averaged values) to determine the eight C coefficients in equation (5.9), the three C_{1n_g} are not linearly independent. This is because only two independent straight lines exit in a two-dimensional plane. Therefore, one of the C_{1n_g} is arbitrarily chosen, and the other seven coefficients are determined by the seven averaged cross sections.

5.2 Analysis

A set of test problems were used to verify the pin power reconstruction calculation in NESTLE. The problems compare the pin power results of 2D infinite lattices (single lattices with reflected boundary conditions), and the second set compares the pin power results of a 2D core section with a reflector region. These test problems use lattice and configurations as specified by a VVER-1000 benchmark based on an operational nuclear power(17; 18). The five lattice types for the initial (cycle 1) core as specified by the benchmark are used as the basis for both sets of test problems. All test problems are at the beginning of cycle (BOC), so no depletion calculations are performed. Test problems use constant temperatures and densities; no thermal-hydraulic cross section feedback is included.

Parameters of the five lattices are specified in 3.1. Each lattice contains 312 fueled pin locations, 18 control rod locations, and 1 central instrument tube location. Pin enrichments range from 1.3% to 4.0%, and three of the five lattices contain integral gadolina burnable absorbers (95% UO2, 5% Gd_2O_3). The temperatures, densities and concentrations were modeled according to the benchmark: fuel temperature 1005 K, coolant temperature 578 K (at 15.7 MPa pressure), and boron concentration 525 ppm. In all models, the control rods are withdrawn, leaving only water in the control rod locations.

The lattices were modeled using SCALE New ESC-based Weighting Transport (NEWT) v6.2b4 with the available 252-group ENDF/B-VII.1 cross section library(10). NEWT is a 2D S_N polygon-mesh deterministic transport module with arbitrary geometry model definitions. NEWT does not directly report form factors or corner discontinuity factors in its output for hexagonal geometries, so form factors were calculated with a post-processing script based on the zone power in each pin. CDFs were calculated using the *fluxplane* option, which allows for calculation of the average scalar flux along any line segment in the geometry. Group flux values were computed for 1 cm line segments on each side of the corners, and the values for the two segments composing each corner were averaged. These averaged group corner flux values were then divided by the lattice homogenized group fluxes to obtain the CDFs. NESTLE uses the NEWT results as input (form factors, CDFs, and homogenized cross sections), and also as the basis of comparison.

5.3 Results

For the reflected lattice test problems, NESTLE's reconstructed pin powers are compared to the pin powers computed by NEWT for each lattice type. Table 5.1 shows a comparison of the minimum and maximum discrepancies and the RMS deviations between NESTLE and NEWT pin powers. The discrepancies are expressed

Table 5.1: Minimum difference, maximum difference, and RMS deviations of pin power factors for the infinite lattices.

Lattice	Minimum Difference [%]	Maximum Difference [%]	RMS Deviation [%]
13au	0.312	0.270	0.154
22au	-0.517	0.603	0.301
30av5	-0.410	0.481	0.238
30awu	-0.730	0.868	0.431
390go	-0.885	0.981	0.501

in absolute percent, not relative. For example, if NEWT were to compute a pin power factor at 0.900 and NESTLE were to compute a pin power factor at 0.901, the discrepancy is +0.1%.

From the results shown Tab. 5.1 , NESTLE computes the pin powers factors within a range of 0.981% as compared to NEWT for all cases. The RMS deviation ranges from 0.154% for the 13au lattice to 0.501% for the 390go lattice. There are two major differences between the five lattice types: lattice averaged enrichment and the location of gadolinia burnable absorbers. The only difference between lattices 13au and 22au are their enrichments. Therefore, the difference in the RMS deviation between the two lattices must be entirely related to enrichment. For all five lattices, there appears to be a trend in increasing RMS deviations with increasing lattice averaged enrichment. Lattices 390go and 39awu have the same lattice averaged enrichments, but differ with the location and number of gadolina pins. The placement of the gadolina pins in the 390go lattice is near the center, while 390awu has some gadolina pins near to the assembly corners. Therefore, the difference in RMS deviation between these two lattices must be due to pin location and not enrichment.

The spatial distributions of the pin power factors are shown in Figure 5.1. In the figures, circle color indicates discrepancy magnitude; black text indicates positive difference; white text indicates negative difference. Because the lattices possesses a 6-fold rotational symmetry, it is sufficient to show results in one sextant. The discrepancy distributions show that, in four of the five lattices, NESTLE under

predicts the pin power factors as compared to NEWT in the lattice interior, and it over predicts the pin power factors near the lattice periphery. The same pattern is observed in all these lattices where exactly the same pins in the inner seven rows show a negative discrepancy, and the other pins (those mostly in the outer three rows) show a negative discrepancy. The exception to this pattern is the 13au lattice, where the exact same pins show a similar distribution but reversed in magnitude. Again, the only difference between lattices 13au and 22au are their enrichments, so an enrichment related effect must be the origin of this inflection. The presence of gadolina pins does not appear to have a local effect on the discrepancy distributions; the discrepancies for individual gadolina pins are similar to those of the neighboring pins. In contrast, the location of pins types does have a global effect on the magnitude of the discrepancy distribution. For the 390go and 39awu lattices that share an average enrichment, the distributions are similar but the magnitude is greater for the 390go lattice. In this case, the different magnitudes of the discrepancy distributions must be driven by pin location, not enrichment.

5.4 Conclusions

NESTLE's reconstructed pin powers generally compare well with the pin powers computed by NEWT for the reflected lattices. The results are consistent with similar published results that tested the same pin power reconstruction method, which stated that for assemblies away from the edge of the core pin powers were reconstructed within 0.2% RMS and 1.0% maximum(34). The observed increase in RMS deviation with increased enrichments may be due to the changes in the neutron energy spectrum. The accuracy of the two-group formalism may be more limited for higher enrichments. The pattern of the spatial distributions of discrepancies, typically overpredicting pin power for exterior pins and underpredicting pin power for interior pins, may be due to errors in reconstructing the intranodal flux. The fluxes along each of the assembly hexagonal surfaces are approximated by a quadratic polynomial,

which limits the accuracy of the reconstructed intranodal flux. The precision of the CDFs may also contribute to errors in reconstructing the intranodal flux. Recall that NEWT does not output the CDFs, rather they are computed after the simulation completes by averaging fluxes along 1 cm line segments on each side of the corners. Because discrepancies are greatest at the corner pins, errors in the CDFs may be the larger effect. The location gadolina pins not have a local effect on the pin power discrepancies because the pin power form factors are not the source of error, instead the error is due to the reconstruction of the intranodal flux.

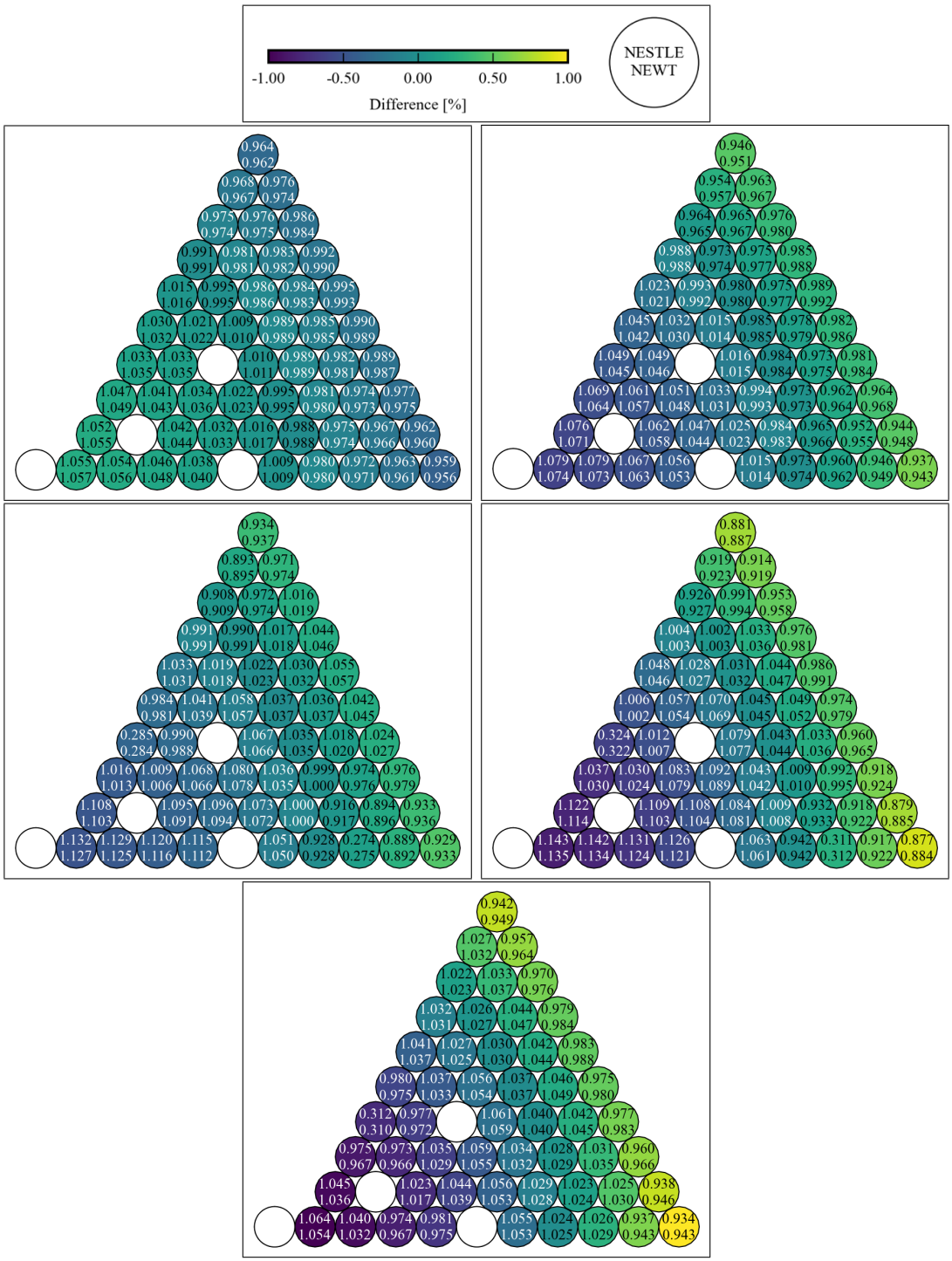

Figure 5.1: NESTLE and NEWT pin powers for the lattice assemblies used in the VVER for verification of pin power reconstruction algorithms. Circle color indicates discrepancy magnitude; black text indicates positive difference; white text indicates negative difference. [Upper Left] Lattice 13au. [Upper Right] Lattice 22au. [Middle Left] Lattice 30av5. [Middle Right] Lattice 39awu. [Lower] Lattice 390go.

Chapter 6

Radial Reflector Model

6.1 Radial Reflectors

The proper development of core periphery discontinuity factors constitutes a crucial step for the accurate modeling and simulation when employing an advanced nodal diffusion simulator. In cores with hexagonal assemblies, such as in the VVER-1000, most fuel assemblies share two faces with the radial reflector, and some even three faces. For this reason, use of a two-dimensional (2D) reflector model will more accurately capture the neutron physics near the core periphery. This section illustrates key points related to the use of 2D discontinuity factors in the reflector region. First, by using an algorithm that applies the methodology proposed by Mittag, Petkov, and Grundmann (35) after correcting some minor typographical errors in the original publication, then by employing the SCALE transport module NEWT to compute the appropriate quantities, and finally by illustrating the impact of 2D discontinuity factors have on pin power reconstruction. Large and even negative discontinuity factors are an acceptable fact of this methodology when the diffusion approximation breaks down because of the localized problem's features and the large flux gradients involved.

6.1.1 Background

In western-style LWRs with square pitched assemblies, most peripheral fuel assemblies share one face with the radial reflector region, and only a few corner assemblies share two boundaries. For these cores, a one-dimensional reflector model can be used to obtain assembly powers accurate to within approximately 4% in most cases (36)(37). In cores with hexagonal assemblies, the situation is different. Only a few hexagonal reflector nodes share only one face with peripheral fuel nodes, most share two faces, and some even share three faces. Because of this feature of the geometry, the one-dimensional reflector model is less accurate for hexagonal cores. In general, using a two-dimensional reflector model will have a greater impact on assembly power accuracy near the periphery for a VVER-1000 core that it would for a western-style LWR core.

Some codes, including NEWT, can calculate the homogenized few-group macroscopic cross sections for a region of the model. As previously described, advanced nodal methods additionally require group discontinuity factors on each node face. Computing these discontinuity factors for the zero net current case is straightforward. It is more difficult to compute discontinuity factors with net currents on the node faces, such as in a reflector region. While NEWT can compute discontinuity factors, it does not do so when a non-zero net current is present on the node faces. To calculate its overall flux solution, NEWT computes the group fluxes and partial currents along many grid lines in the geometry. By using the *fluxplane* feature of the code, group fluxes and currents for any line coincident with the gridlines in the geometry are written to the output file. This feature is useful for calculating two-group discontinuity factors after the NEWT computation is complete.

6.1.2 Radial Reflector Two-Group Discontinuity Factors

A method to compute discontinuity factors for non-multiplying material in two-dimensional hexagonal reactor geometry has been presented by Mittag, Petkov, and Grundmann(35). The method is based on expanding the group fluxes using:

$$\phi(x,y) = \sum_{n=1}^{N} C_{g,n}^{+} e^{\mu_g (k_{n,x} x + k_{n,y} y)} + C_{g,n}^{-} e^{-\mu_g (k_{n,x} x + k_{n,y} y)} \tag{6.1}$$

where $N = 3$, $k_{n,x} = \cos\theta_n$, $k_{n,y} = \sin\theta_n$, $\theta_n = \pi(n-1)/N$. The constants μ_g are based on the homogenized group cross sections, and $C_{g,n}^{\pm}$ are coefficients to be determined. The method is a two-group formulation and would require significant modifications for groups other than two. A derivation of the method is presented in the reference, and is not repeated here. Instead the method is presented as a matrix algorithm, where some minor typographic errors from the original publication have been corrected:

1. From the transport solution, obtain the net currents $J_{g,s}^{\text{Net}}$ and the heterogenous fluxes $\phi_{g,s}^{\text{Het}}$ along each side of the hexagon. The net currents are defined to be positive when the current direction is outward from the hexagon, and negative when the current direction is inward. Currents reported by NEWT are positive in the $+x$ and $+y$ directions. Therefore, the following equation must be used:

$$J_{g,s}^{\text{Net}} = J_{g,s}^{x+} \cos\theta_s + J_{g,s}^{y+} \sin\theta_s \tag{6.2}$$

   where θ_s defines the outward normal for each side; in this case $\theta_s = \left[0, \frac{\pi}{3}, \frac{2\pi}{3}, \pi, \frac{4\pi}{3}, \frac{5\pi}{3}\right]$ for sides = [East, Northeast, Northwest, West, Southwest, Southeast].

2. The two-group homogenized cross sections are used to define three parameters:

$$\mu_1 = \sqrt{\Sigma_{\text{R},1}/D_1} \tag{6.3}$$

$$\mu_2 = \sqrt{\Sigma_{\mathrm{a},2}/D_2} \tag{6.4}$$

$$\alpha = \frac{\Sigma_{\mathrm{s},1\to 2}}{\Sigma_{\mathrm{a},2} - D_2\mu_1^2} \tag{6.5}$$

where Σ_{a} is the group absorption macroscopic cross section, Σ_{s} is the group to group scattering macroscopic cross section, D is the diffusion coefficient, and $\Sigma_{\mathrm{R},1} = \Sigma_{\mathrm{a},1} + \Sigma_{\mathrm{s},1\to 2}$ is the fast group removal macroscopic cross section.

3. Compute the 6×6 matrices $\mathbf{M}_g$:

$$\mathbf{M}_g = \begin{bmatrix} m^+_{g,0} & m^-_{g,0} & M^+_{g,1,2} & M^-_{g,1,2} & M^+_{g,1,3} & M^-_{g,1,3} \\ M^+_{g,2,1} & M^-_{g,2,1} & m^+_{g,0} & m^-_{g,0} & M^+_{g,2,3} & M^-_{g,2,3} \\ M^+_{g,3,1} & M^-_{g,3,1} & M^+_{g,3,2} & M^-_{g,3,2} & m^+_{g,0} & m^-_{g,0} \\ m^-_{g,0} & m^+_{g,0} & M^+_{g,4,2} & M^-_{g,4,2} & M^+_{g,4,3} & M^-_{g,4,3} \\ M^+_{g,5,1} & M^-_{g,5,1} & m^-_{g,0} & m^+_{g,0} & M^+_{g,5,3} & M^-_{g,5,3} \\ M^+_{g,6,1} & M^-_{g,6,1} & M^+_{g,6,2} & M^-_{g,6,2} & m^-_{g,0} & m^+_{g,0} \end{bmatrix} \tag{6.6}$$

where

$$m^{\pm}_{g,0} = \pm\mu e^{\pm\mu_g d/2} \tag{6.7}$$

$$M^{\pm}_{g,s,n} = \frac{k^s_{n,x}}{k^s_{n,y}} \left(e^{\pm\mu_g d/2(k^s_{n,x} + k^s_{n,y}/\sqrt{3})} - e^{\pm\mu_g d/2(k^s_{n,x} - k^s_{n,y}/\sqrt{3})} \right) \tag{6.8}$$

with

$$k^s_{n,x} = \cos\left(\theta_n - \theta_s\right) \tag{6.9}$$

$$k^s_{n,y} = \sin\left(\theta_n - \theta_s\right) \tag{6.10}$$

$$\theta_s = \frac{2\pi(s-1)}{6} \tag{6.11}$$

$$\theta_n = \frac{\pi(n-1)}{3} \tag{6.12}$$

and d is the distance between parallel sides of the regular hexagon (equivalent to the pitch of a regular hexagonal lattice).

4. For the fast and thermal groups, solve the matrix equations:

$$\overrightarrow{J_1^{\text{Net}}} = -\frac{D_1\sqrt{3}}{d}\mathbf{M}_1\overrightarrow{C_1} \tag{6.13}$$

$$\overrightarrow{J_2^{\text{Net}}} = -\frac{D_2\sqrt{3}}{d}\mathbf{M}_2\overrightarrow{C_2} + \frac{\alpha D_2}{D_1}\overrightarrow{J_1^{\text{Net}}} \tag{6.14}$$

for the 1×6 group coefficient vectors $\overrightarrow{C_g}$

5. Using the coefficient vectors $\overrightarrow{C_g}$, solve the matrix equations:

$$\overrightarrow{\phi_1^{\text{Hom}}} = \frac{\sqrt{3}}{\mu_g d}\mathbf{F}_1\overrightarrow{C_1} \tag{6.15}$$

$$\overrightarrow{\phi_2^{\text{Hom}}} = \frac{\sqrt{3}}{\mu_g d}\mathbf{F}_2\overrightarrow{C_2} + \alpha\overrightarrow{\phi_1^{\text{Hom}}} \tag{6.16}$$

for the fast and thermal homogeneous fluxes $\overrightarrow{\phi_g^{\text{Hom}}}$, where the 6×6 matrix:

$$\mathbf{F}_g = \begin{bmatrix} f_{g,0}^{+} & f_{g,0}^{-} & F_{g,1,2}^{+} & F_{g,1,2}^{-} & F_{g,1,3}^{+} & F_{g,1,3}^{-} \\ F_{g,2,1}^{+} & F_{g,2,1}^{-} & f_{g,0}^{+} & f_{g,0}^{-} & F_{g,2,3}^{+} & F_{g,2,3}^{-} \\ F_{g,3,1}^{+} & F_{g,3,1}^{-} & F_{g,3,2}^{+} & F_{g,3,2}^{-} & f_{g,0}^{+} & f_{g,0}^{-} \\ f_{g,0}^{-} & f_{g,0}^{+} & F_{g,4,2}^{+} & F_{g,4,2}^{-} & F_{g,4,3}^{+} & F_{g,4,3}^{-} \\ F_{g,5,1}^{+} & F_{g,5,1}^{-} & f_{g,0}^{-} & f_{g,0}^{+} & F_{g,5,3}^{+} & F_{g,5,3}^{-} \\ F_{g,6,1}^{+} & F_{g,6,1}^{-} & F_{g,6,2}^{+} & F_{g,6,2}^{-} & f_{g,0}^{-} & f_{g,0}^{+} \end{bmatrix} \tag{6.17}$$

with

$$f_{g,0}^{\pm} = \frac{\mu_g d}{\sqrt{3}} e^{\pm\mu_g d/2} \tag{6.18}$$

$$F_{g,s,n}^{\pm} = \frac{\pm 1}{k_{n,y}^{s}} \left(e^{\pm\mu_g d/2(k_{n,x}^{s} + k_{n,y}^{s}/\sqrt{3})} - e^{\pm\mu_g d/2(k_{n,x}^{s} - k_{n,y}^{s}/\sqrt{3})} \right) \tag{6.19}$$

6. Compute the group discontinuity factors for each side:

$$d_{g,i}\phi_g^{\text{Hom}}(\frac{\Delta x_i}{2}) = d_{g,i+1}\phi_g^{\text{Hom}}(\frac{\Delta x_{i+1}}{2}) \tag{6.20}$$

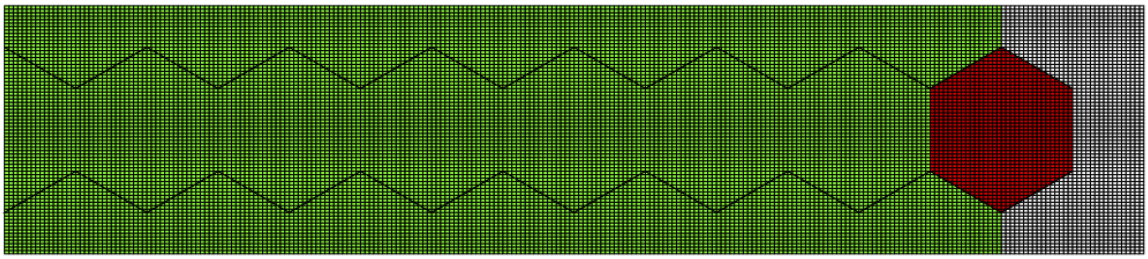

Figure 6.1: A NEWT model designed to test the two-dimensional hexagonal reflector discontinuity factor method. The fuel is shown in green, the reflector in red.

This method does not guarantee positive homogeneous fluxes. If the flux gradient across the reflector node is large, the homogeneous fluxes, and therefore the discontinuity factors, may be negative on the faces not adjacent to fuel nodes. These negative values can be attributed to a failure of the diffusion approximation, which is inaccurate in regions of large flux gradients. Although negative discontinuity factors may appear disconcerting for a nodal model, they can be acceptable if the average homogeneous flux in the reflector region remains positive, and if the the faces with negative factors define the outer boundary of the nodal problem where the flux is nearly zero.

6.1.3 Radial Reflector Two-Group Discontinuity Factor Test Problem

The algorithm presented above was coded in Python. To verify the code, a test problem was constructed with NEWT using fuel and reflector mixtures at infinite dilution. The model geometry is shown in Figure 6.1. The hexagonal pitch is 23.4 cm. All boundaries have reflected boundary conditions, except the boundary to the right of the reflector, which has a vacuum boundary condition. NEWT computed the homogenized two-group cross sections and the heterogeneous flux and currents along the six faces of the reflector node. Using these values as input, the Python code determined the homogeneous fluxes and discontinuity factors on the six faces.

The discontinuity factors calculated by the Python code are shown in Table 6.1. The test problem is symmetric across its central x-axis, and as expected, so are the discontinuity factors. Note that discontinuity factor on the East face is negative for the thermal group and positive but relatively large for the fast group. Likewise, the Northeast and Southeast thermal group discontinuity factors are also relatively large. Because discontinuity factors are simply a ratio of fluxes, and it is nonphysical for a

Table 6.1: Discontinuity factors for the hexagonal reflector region test problem.

Reflector Face	Fast Group	Thermal Group
East	2.363017	-0.388521
Northeast	1.056869	2.234352
Northwest	1.103021	0.912144
West	1.148919	1.027277
Southwest	1.103021	0.912144
Southeast	1.056869	2.234352

flux to have a negative value, a negative discontinuity initially appears impossible or at least an error. Although fluxes are physical quantities, discontinuity factors are not, rather they are mathematical corrections that are used to attempt to preserve the continuity of the heterogeneous flux across an artificial boundary. Therefore, discontinuity factors are actually a measure of the discrepancy between a more exact transport calculation and a less approximate diffusion calculation.

By design the diffusion approximation neglects some of the physics present in the neutron transport equation. The neglected physics does not play a significant role in determining the flux solution, so long as assumptions of the diffusion approximation are valid. While negative valued flux solutions of the diffusion equation may exist, these solutions have no physical meaning. If the only solution to the diffusion equation is negatively valued, the assumptions of the diffusion approximation have been violated.

In the case of negatively valued discontinuity factors in the reflector region, the assumption that is violated is that the flux gradient is small over the diffusion length. In these regions, the diffusion flux solution will fall off more rapidly than the transport solution. Lacking the full physics of the transport solution, eventually the diffusion flux solution will become negative, while the transport solution will likely remain positive. Long before the diffusion flux solution becomes negatively valued, the discrepancy between the diffusion and transport solutions will increase. This explains why some reflector discontinuity factors on the outer edges may be negative, have a magnitude significantly larger than 1.0, or both.

While the purpose of the Python code is to determine the reflector discontinuity factors, in the process the code also determines the coefficient vector $\overrightarrow{C_g}$. These coefficients can be used in equation (6.1) to plot the two-group homogeneous flux as determined by the diffusion approximation. Because the NEWT model used infinitely dilute fuel and reflector mixtures for regions with no detailed geometry, the spatial shape of the two-group homogeneous flux should be an excellent approximation to the two-group transport flux spatial shape computed by NEWT. The heterogeneous (transport) and homogeneous (diffusion) spatial flux shapes for the fast and thermal groups is shown in Figure 6.2.

The absolute difference between the heterogeneous and homogeneous fluxes across the reflector node has a maximal discrepancy on the order of 10^{-4}. This small difference demonstrates that the coefficients computed by the Python code are accurate. The maximal difference occurs near the vertices of the East face for the thermal flux, where the homogeneous flux actually becomes negative. Again, we note that this is due to the failure of the diffusion approximation in a region with a large flux gradient. This also explains the negative discontinuity factor for the thermal group along the East face. While the homogeneous fast flux stays positive on the East boundary, it is much less than the heterogeneous fast flux. This explains the relatively large discontinuity factor for the fast group along the East face. The relatively large thermal discontinuity factors along the Northeast and Southeast faces

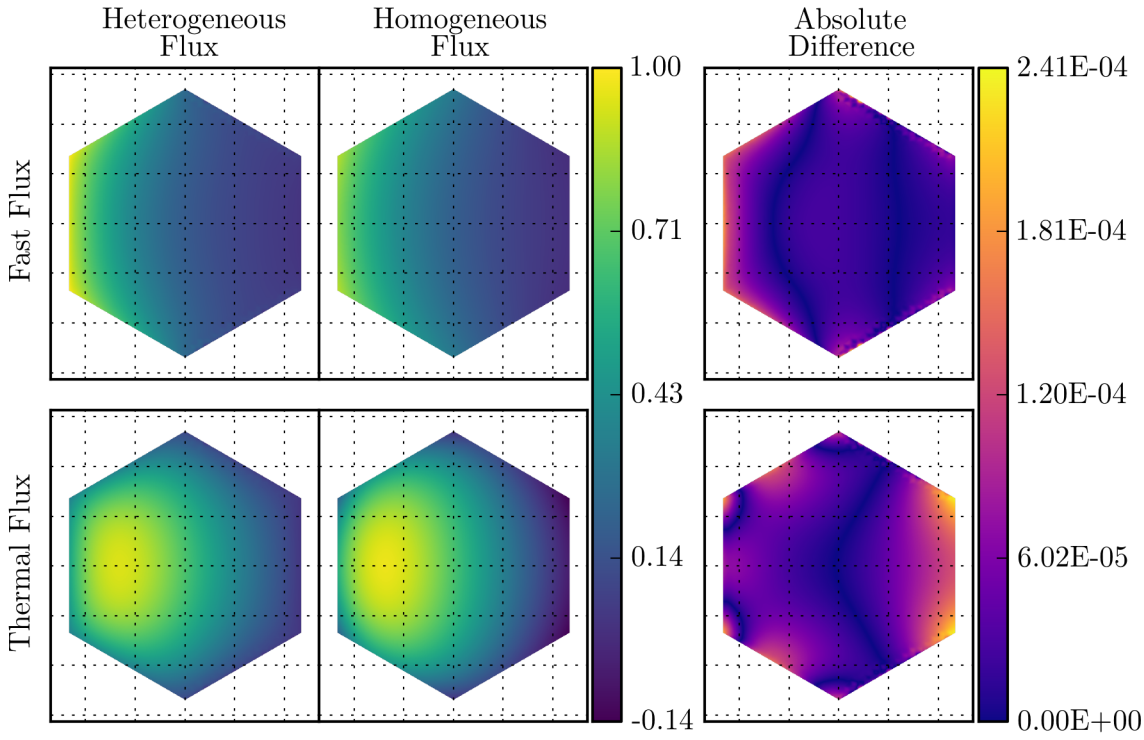

Figure 6.2: The heterogeneous (transport) and homogeneous (diffusion) spatial flux shapes and their absolute difference for the fast and thermal energy groups. The flux units are arbitrary and scaled to 1.0.

are due to similar conditions: a small but positive homogeneous flux. If the reflector material composition were different such that the flux gradient were even greater, or if the reflector region were larger, it's possible that these homogeneous fluxes and discontinuity factors could drop below zero as well.

The excellent agreement between the homogeneous and heterogeneous spatial flux shapes verifies the Python code through Step 4 of the method outlined in Section 6.1.2. To verify Step 5 of the method, the the average value of the homogeneous flux along each face as computed by equation (6.1) can be compared to the average value as computed by equations (6.15) and (6.16) in the matrix algorithm. The ratios of equation (6.1) averaged over 5000 points along each hexagon face to the homogeneous fluxes computed by the matrix algorithm is very nearly 1.0. These ratios are shown in Table 6.2. Based on the results of this test problem, the Python

code has verified to calculate expected discontinuity factors. Further confirmation will be seen in the improved flux distribution of the peripheral fuel nodes in the nodal core model results.

Table 6.2: Ratios of the average homogeneous fluxes along each face as computed numerically by equation (6.1) averaged over 5000 points to the average homogeneous fluxes as computed by the matrix algorithm.

Reflector Face	Fast Group	Thermal Group
East	1.000123	0.99986
Northeast	0.999930	1.00057
Northwest	0.999982	1.00014
West	0.999987	1.00011
Southwest	0.999982	1.00014
Southeast	0.999930	1.00057

6.2 Pin Power Reconstruction

6.2.1 Impact of 2D Reflector on Pin Power Reconstruction

To demonstrate the impact of a 2D reflector model on a pin power calculation, a 1/12 2D VVER-1000 core model was built using a fuel design based on the the benchmark core calculation as documented by T. Lötsch (18). The model was simulated using the SCALE 6.2 KENO-VI Monte Carlo code. Using 1×10^5 histories per generation, with 1000 generations (200 disregarded for fission convergence), the simulation computed the fission densities in each pin region in the core section. The percent deviations of the fission densities are shown in figure 6.3. The majority of the pins are converged to less than 1% deviation, the notable exceptions are two types of pins: the U-Gd integral burnable poison pins, and those pins near the core periphery. Those pins with the greatest percent deviation are the burnable poison pins near the periphery. In all cases, the pins are converged to a percent deviation of 1.9% or less. The pin power factors are shown in figure 6.4.

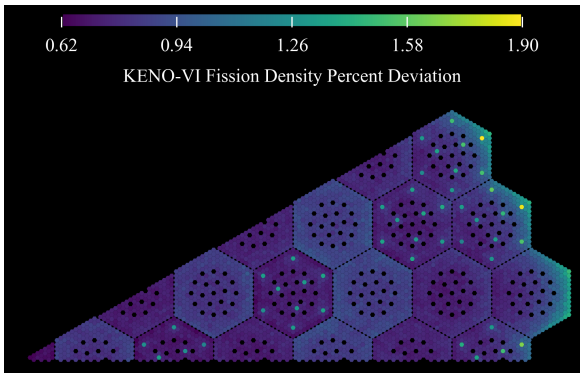

Figure 6.3: The percent deviation in the fission density calculation for each pin as computed by KENO-VI.

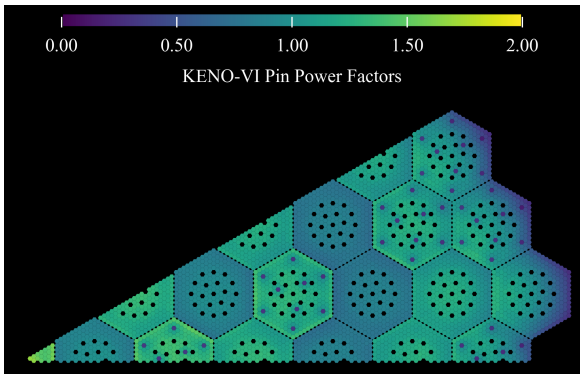

Figure 6.4: The relative pin power factors as computed by KENO.

Similar VVER-1000 models were also constructed using the SCALE 6.2 NEWT S_N transport code. Each of the 5 lattice types were modeled as single infinite assemblies with reflected boundaries and the cross sections and discontinuity factors were condensed, homogenized, and prepared for input into the NESTLE nodal core simulator. Two types of reflector models were simulated using NEWT: a 1D (slab) reflector model, and a 2D reflector model using a one-twelth core section model similar to the KENO-VI model. These reflector cross sections were also condensed, homogenized, and prepared for input into the NESTLE nodal core simulator. When the results of the NESTLE pin power reconstruction were compared with the KENO results, the 2D reflector model showed a significant improvement over the 1D reflector model. The comparison of the NESTLE results with the KENO results are shown in

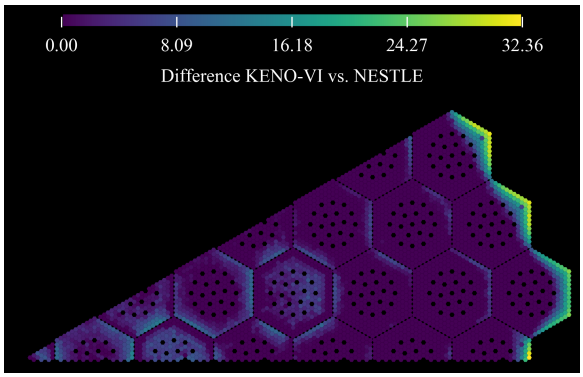

Figure 6.5: The percent difference in pin power between the KENO and NESTLE calculations using 1D cross sections and 1D discontinuity factors.

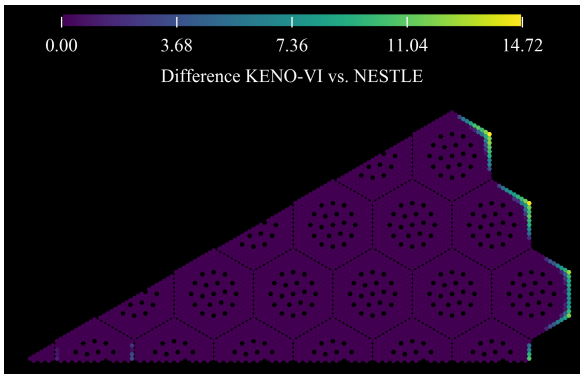

Figure 6.6: The percent difference in pin power between the KENO and NESTLE calculations using 2D cross sections and 2D discontinuity factors.

figures 6.5 and 6.6. For both the 1D and 2D models, the maximum discrepancy in pin power reconstruction is seen along the core periphery, but the magnitude of the maximum discrepancy for the 2D model is approximately half that of the 1D model. It should be noted that in a typical core configuration, these pins are some of the lowest powered pins in the core. Therefore they are the pins that are of the least concern since they are furthest from their thermal limits.

Chapter 7

Nuclide Sensitivity to Operational Conditions

The final step of this work is to explore the sensitivity of spent nuclear fuel nuclide inventory to operational parameters such as power, inlet temperature, and coolant flow rate. To accomplish this, the NESTLE inputs are perturbed and the whole core outputs are compared to the reference conditions. Speed is an advantage of using a nodal diffusion simulator like NESTLE over transport or Monte Carlo methods. A nodal diffusion code like NESTLE can complete the calculations in a few minutes using a single CPU, while Monte Carlo codes would take many hours or several days to complete using many CPUs.

7.1 Perturbation of Inputs

Before the operational parameters are varied, reference conditions must be established. These reference conditions are based on the conditions for cycle 1 of the AER benchmark. The reference cycle will run to the same total core burnup (12.5 GWd/MTU). The power through the cycle remains constant at 100% of the nominal cycle power. Likewise the flow conditions are 100% of the nominal flow

Table 7.1: Perturbation of inputs.

Case	Flow Rate %	Inlet Temperature $^\circ F$	Power %	Boron Concentration %	Rod Position
Base	100.0	548.0	100.0	100.0	Average
Boron -10%	100.0	548.0	100.0	90.0	Average
Boron -5%	100.0	548.0	100.0	95.0	Average
Boron +5%	100.0	548.0	100.0	105.0	Average
Boron +10%	100.0	548.0	100.0	110.0	Average
Flow -10%	90.0	548.0	100.0	100.0	Average
Flow -5%	95.0	548.0	100.0	100.0	Average
Flow +5%	105.0	548.0	100.0	100.0	Average
Flow +10%	110.0	548.0	100.0	100.0	Average
Power -10%	100.0	548.0	90.0	100.0	Average
Power -5%	100.0	548.0	95.0	100.0	Average
Power +5%	100.0	548.0	105.0	100.0	Average
Power +10%	100.0	548.0	110.0	100.0	Average
Inlet -10$^\circ F$	100.0	538.0	100.0	100.0	Average
Inlet -5$^\circ F$	100.0	543.0	100.0	100.0	Average
Inlet +5$^\circ F$	100.0	553.0	100.0	100.0	Average
Inlet +10$^\circ F$	100.0	558.0	100.0	100.0	Average
Rod Min	100.0	548.0	100.0	100.0	Minimum
Rod Max	100.0	548.0	100.0	100.0	Maximum
Rod In	100.0	548.0	100.0	100.0	Full In
Rod Out	100.0	548.0	100.0	100.0	Full Out

conditions, the control rods are parked at the average insertion, and the inlet temperature is constant at the average inlet temperature value. The boron letdown for these conditions is established by running NESTLE's criticality search.

Five operational parameters are varied: boron concentration, flow rate, inlet temperature, power, and rod position. Each is parameter is perturbed over a range of variability. Establishing this range is subjective and based on the range of normal and off-normal conditions that may be expected during operation. For the boron concentration, flow rate, and power, conditions are perturbed by $\pm$ 5% of the nominal value and $\pm$ 10% of the nominal value. The inlet temperature is varied by $\pm$ 5 deg F and $\pm$ 10 deg F. The rod position is varied by parking the control banks at the maximum and minimum insertion positions listed in the AER benchmark. Two extreme rod positions are also examined: the rods fully removed from the core, and the rods fully inserted in the core.

This is a single parameter study, so the operational parameters are varied individually. For each perturbation, criticality ($k_{\text{eff}} = 1$) is not re-established because this would require a variation in an additional parameter such as flow rate, rod position, or soluble boron concentration. By not re-establishing criticality, the effect of each perturbation can be examined individually without the confounding effects of criticality control. Future work could include the variation of multiple parameters and the variation of parameters while the core remains critical.

7.2 Core ^{239}Pu Distributions

Because ^{239}Pu is a significant plutonium isotope for operational and security purposes, this nuclide was selected for perturbation studies. All of the microscopic depletion model nuclides were output from the simulations, and any of them were available for analysis.

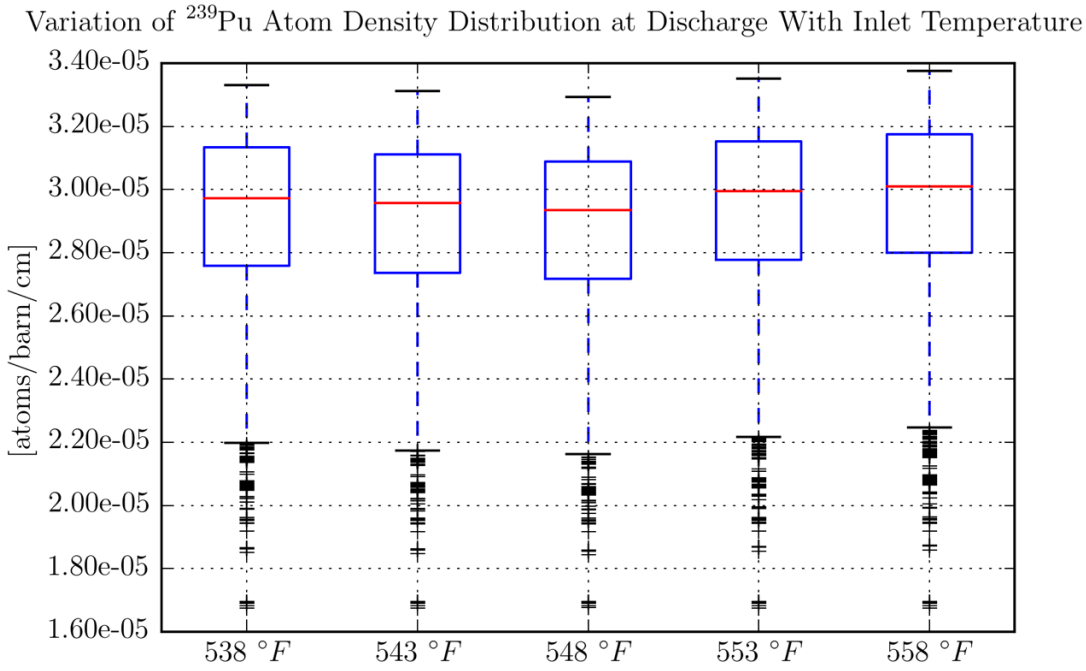

Figure 7.1: Box plot for the core distributions of ^{239}Pu at discharge burnup of 12.5 [MWd/MTU] with varying coolant inlet temperatures.

Figures 7.1-7.3 show five box plots for the base and perturbed cases. Box plots are one way of illustrating a distribution of values. The spacing between the components of the plot represent the dispersion and skewness of the data. Here the central box represents the interquartile range where the middle 50% of values reside. The red line represents the median value and divides the interquartile range into quartiles. The whiskers on the plot span 1.5 the width of the interquartile range. Outliers, those values outside the whiskers, are plotted as hashes.

The base case distribution in Figures 7.1-7.3 is asymmetric. The upper whisker is much closer to the interquartile range than the bottom whisker, demonstrating a negatively skewed distribution. There is a long tail toward lower ^{239}Pu atom concentrations. Based on the the VVER-1000 lattices depletion studies, such as those shown in Figure 3.4, ^{239}Pu continues to burn in as the core is depleted. But, as more ^{239}Pu is produced, more of it is also destroyed through fission and absorption until the total atom concentration of ^{239}Pu nearly reaches equilibrium around 30 GWd/MTU.

At the core averaged burnup of 12.5 GWd/MTU (discharge), the total concentration of ^{239}Pu will be increasing at a rate nearly as rapidly as at lower burnups. Because at this core averaged burnup, greater ^{239}Pu concentrations are correlated with greater burnup, the distributions can be interpreted in terms of burnup. The upper whisker contains the highest burnup regions of the core, which generally would be located near the radial center and axial middle of the core. The lower whisker and the long tail represent the lower burnup regions near the radial and axial periphery.

The box plots in Figure 7.1 for the perturbations with inlet temperature show changes in the ^{239}Pu distributions. As the inlet temperature is increased from the base case the distributions are shifted toward higher concentrations. Because the inlet temperature has a significant effect on the coolant density, these changes are like due to the moderator density effect noted in Figure 3.5. The box plot demonstrates while the median, box, and whiskers generally shift to higher concentrations, a group of outliers with the lowest concentrations remain unchanged. As the inlet temperature is reduced, there is also a positive shift in the ^{239}Pu distribution, although this effect is smaller than the positive increase in temperatures. The increase in the median ^{239}Pu concentration is not easily explained, but it may be related to an increase in reactivity due to the decrease in the temperature.

Figure 7.2 illustrates the changes in the core ^{239}Pu distributions with power level. A similar trend is seen in these perturbations as those for inlet temperature. The increasing power leads to a greater median ^{239}Pu concentration, while decreasing power has a smaller effect on increasing the median ^{239}Pu. Generally the nuclide compositions of SNF is considered to be dependent primarily on the total burnup of the fuel, and mostly independent of the power level at which it was produced. In this core wide case, there are at least two feedback mechanisms that would have some impact on the composition: temperatures and ^{135}Xe equilibrium concentration. A higher core power leads to greater temperatures in the fuel and coolant. In consideration of this, it is not surprising that the trends for higher power operation are similar to the trends for higher inlet temperature. The higher power operation would

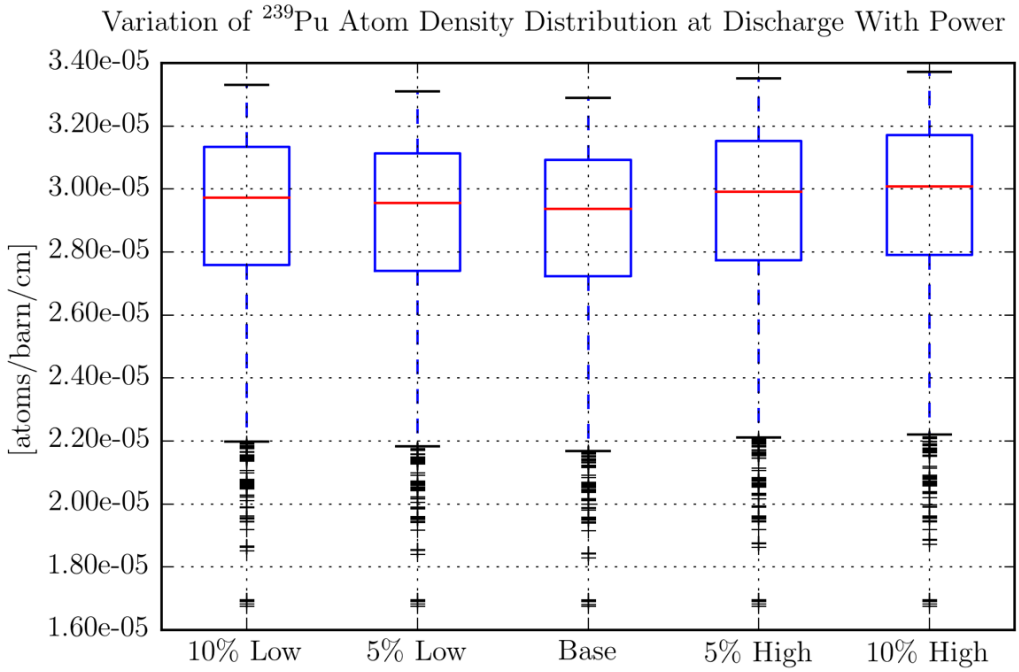

Figure 7.2: Box plot for the core distributions of ^{239}Pu at discharge burnup of 12.5 [MWd/MTU] with varying total power.

also produce a greater concentration of ^{135}Xe. The ^{135}Xe concentration increases non-linearly with increasing power level. In local regions, the greater concentrations of ^{135}Xe and the associated increase in thermal absorption should affect on the production of the plutonium isotopes.

Figure 7.3 shows the variations the core ^{239}Pu distributions with rod position. Three (Full Out, Min Insertion, and Max Insertion) of the four perturbations appear similar to the base case. In these cases, the median ^{239}Pu concentration does not significantly change, but small changes can be seen in the number of outliers. This is most likely because these three control rod positions are relatively similar. For typical operation, the control rods are inserted only partially, so the minimum ($\approx 10\%$) and maximum ($\approx 30\%$) insertions produce distributions similar to the case with the rods fully removed (0%). The "Full In" case produces a greater median

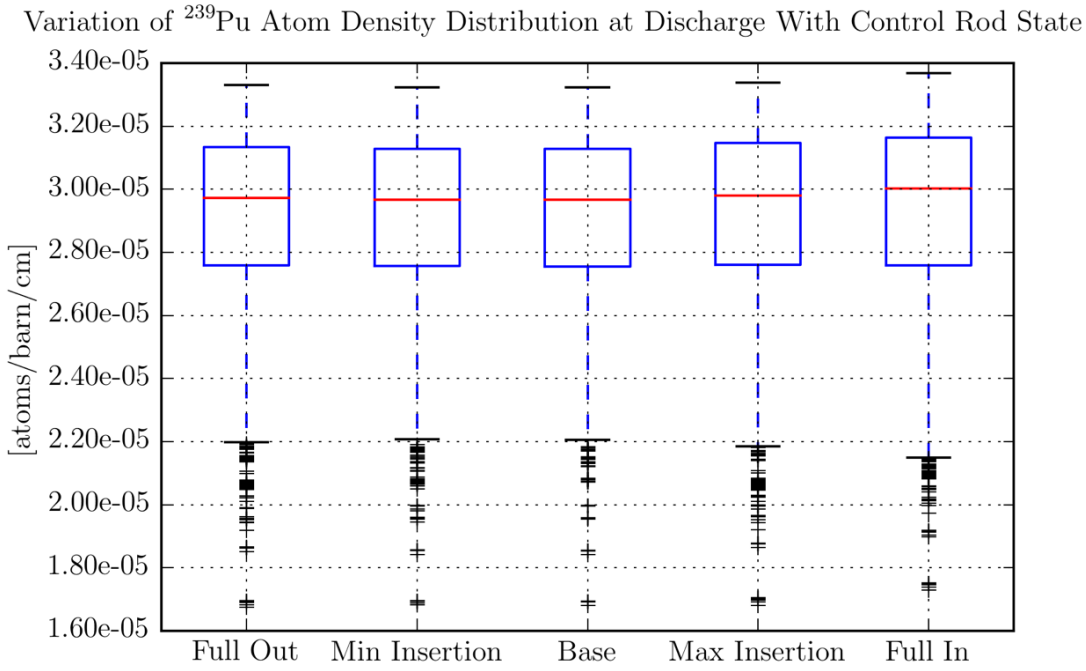

Figure 7.3: Box plot for the core distributions of ^{239}Pu at discharge burnup of 12.5 [MWd/MTU] with varying parked control rod locations.

^{239}Pu concentration, but also increases the overall dispersion of the distribution as shown by the increased span of both the upper and lower whiskers. The distribution becomes more negatively skewed than the base case.

Figures 7.4 and 7.5 show the changing ^{239}Pu distributions due to boron and flow perturbations. The box plots show that for the magnitude of perturbations considered, the effect is very minimal. This is not too surprising in the case of soluble boron because it is distributed throughout the entire core, and it's presence does not have a significant impact on the thermal hydraulic feedback mechanisms of temperature or density. As a reactivity control, its effect is to increase thermal absorption, and therefore it does impact the neutron spectrum, but not so much in these cases that the ^{239}Pu distributions are affected. Perturbation on the flow rate were expected to have an effect on the ^{239}Pu distributions that would be similar to the effect observed with inlet temperature and power. This was expected because like the inlet temperature and power, the coolant flow should directly affect coolant

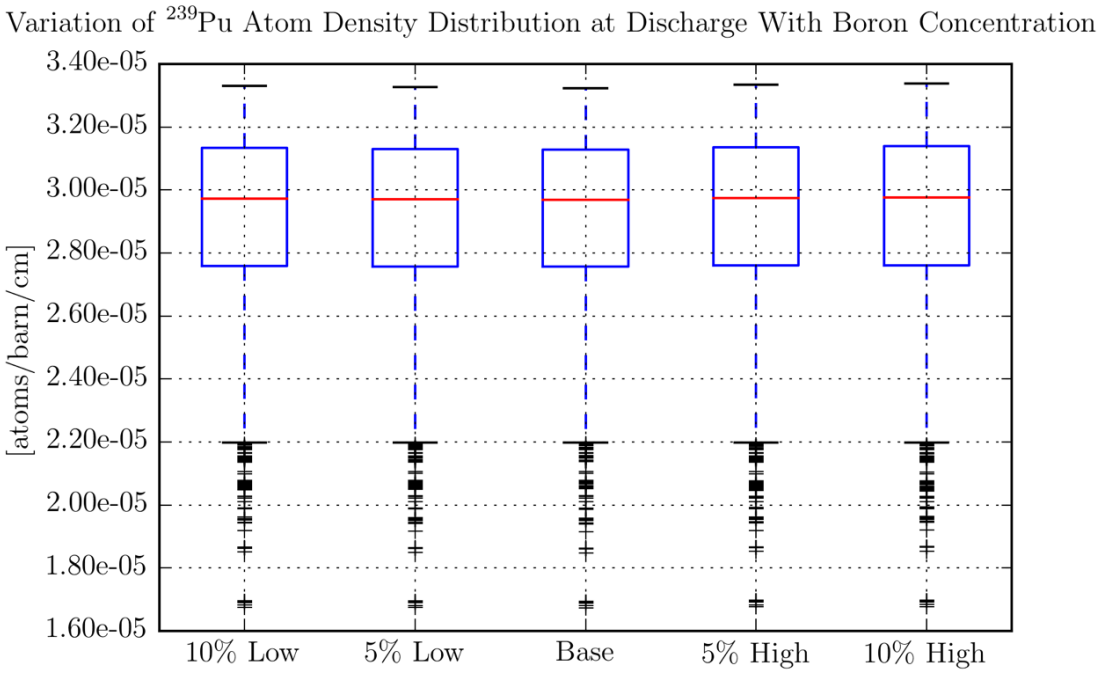

Figure 7.4: Box plot for the core distributions of ^{239}Pu at discharge burnup of 12.5 [MWd/MTU] with varying total boron concentrations.

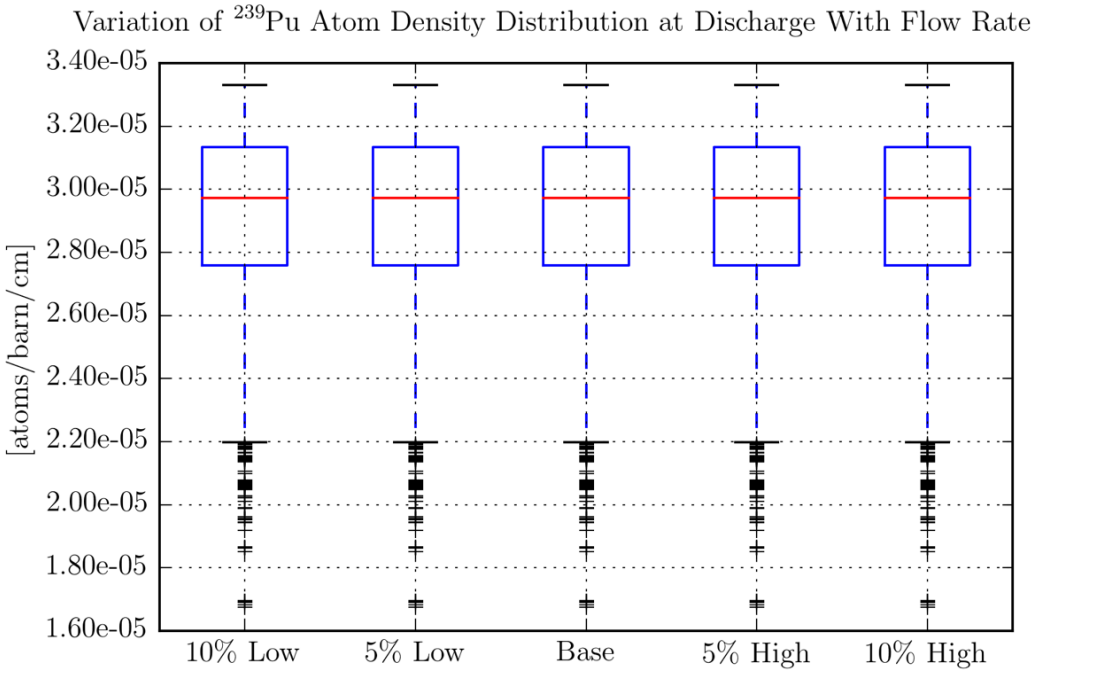

Figure 7.5: Box plot for the core distributions of ^{239}Pu at discharge burnup of 12.5 [MWd/MTU] with varying coolant flow rates.

temperature and density and fuel temperature. No significant effects were observed by perturbing the flow, perhaps because the magnitude of the perturbations were not large enough the cause significant changes in the ^{239}Pu distributions. Future studies will use perturbations of larger magnitude for boron and flow in an attempt to qualify the effects.

These perturbation studies demonstrate the capability of the microscopic depletion model in understanding the effect core operational parameters have on nuclide production. Future studies will consider a larger range of operational parameters with greater magnitudes. In the studies presented herein, only single parameter perturbations were performed. Future studies will include perturbations of multiple parameters. These initial studies ignored criticality to avoid using additional criticality control. Future studies will select a manner of criticality control (control rods, boron, power, or flow speed) and maintain a critical core during depletion. These studies will compare fuel at discharge when reactivity can no longer be maintained, rather than at a specific burnup. This is a manner of reactor operation more consistent with typical operation. The studies presented herein only examined the total core distribution of ^{239}Pu and intentionally avoided spatial analysis. Future studies will examine how the nuclides distributions change in relation to their location in the core (for every assembly, node, fuel type, or pin). Finally, these studies were limited to ^{239}Pu, but many examinations of SNF rely on measuring ratios of isotopes. Therefore, future sensitivity studies will examine the ratios of various uranium and plutonium isotopes.

Chapter 8

Conclusions

This work explored the use of microscopic depletion modeling of a VVER-1000 with the NESTLE nodal core simulator to determine nuclide compositions. The accuracy of power reconstruction was also considered so that pins could be selected for individual depletion calculations. To complete this work, a new acceptably accurate model of an operational VVER-1000 was created and improved. By improving the radial reflector model, the the effect of two-dimensional ADFs was quantified on pin power reconstruction. This effect had not been previously demonstrated. The lattice physics code NEWT was modified such that the appropriate two-group nuclide data was output during its calculation. Additionally, NEWT was modified such that CDFs could be computed by using the *fluxplane* feature of the code. NESTLE was modified in several ways, most importantly to allow for input of non-local power due to fission. Thousands of lines of code were written to manage the data processing between NESTLE and NEWT. Finally, the perturbation effects of several operational parameters (flow, inlet temperature, power, and rod insertion) on ^{239}Pu nuclide composition were demonstrated. All of this work furthers the development of NESTLE not just as a nodal core simulator, but as a SNF computational tool.

8.1 VVER-1000 Core Modeling

An core-follow calculation based on a VVER-1000 operational benchmark has been presented. Lattices of the benchmark were modeled using several different codes. Nuclide composition results for these lattice results were found to be in close agreement with the benchmark reported results, but at high burnups (≈60 GWd/MTU), there may be a few percent difference in nuclide concentrations. The discrepancy in core k_{eff} values calculated by NESTLE compared to the benchmark ranges mostly between ±200 pcm over the course of the cycle 1 depletion. Based on the comparison of the radial power distributions, the radial reflectors do not appear to be the largest contributor to the modeling errors. It is likely that NESTLE's inability to model axially heterogeneous control rods may explain some of the discrepancies seen in the k_{eff} calculation. The correlation between the early cycle k_{eff} discrepancy and the axial offset discrepancy may be an indication that k_{eff} agreement would improve with a better bottom and top axial reflector models.

8.2 Microscopic Depletion Model

The use and improvement of NESTLE's microscopic depletion capabilities has been demonstrated. The subregion depletion capabilities in NESTLE are based on precomputed neutron group flux disadvantage factors, which does not include changes to the local flux due to core conditions. Preliminary implementation of pin-level isotopic tracking and control rod depletion using ORIGEN coupled to NESTLE has been shown. These features, while potentially very useful, are not fully implemented to account for thermal hydraulic conditions. NESTLE's microscopic depletion model does compensate for thermal hydraulic conditions, although the model requires a large amount of additional data. These data are produced by source code modifications to the 2D transport code NEWT, processed by several modules of specifically constructed Python code, and interpreted by a modified version of

NESTLE. The NESTLE source code was modified to accept the non-local fission power terms as input and use them to correct the flux scaling. The magnitude of history effects for each uranium and plutonium nuclide for each branch was computed by using TRITON, and may produce a relative discrepancy of greater than 30%, depending on the nuclide, the branch conditions, and the burnup. These effects can often be mitigated the level of 5% or less for the uranium and plutonium nuclides using NESTLE's microscopic depletion model.

8.3 Pin Power and Radial Reflectors

A set of test problems were used to verify the pin power reconstruction calculation in NESTLE. Pin powers factors are computed within a range of ≈1% relative error as compared to NEWT for all cases. Spatial variations in the pin power discrepancies are observed, along with an increase in RMS error that correlates with average pin enrichment. Corrections to the 2D reflector discontinuity factor method of Mittag, Petkov, and Grundmann have been presented and the method has been illustrated in an algorithm. The results of the algorithm in a simple test problem have been shown, along with the impact of 2D discontinuity factors on pin power reconstruction. The pin power results demonstrate the impact of using 2D discontinuity factors for the radial reflectors.

8.4 Sensitivity of Nuclide Composition

Five operational parameters are varied: boron concentration, flow rate, inlet temperature, power, and rod position. Each is parameter is perturbed over a range of variability. The parameters with the greatest effects on ^{239}Pu distributions were the inlet temperature and core power. This likely due to their direct impact on the coolant temperature density. The two perturbations were found to produce similar effects with increasing inlet temperature and increasing power.

For control rod perturbations, three (Full Out, Min Insertion, and Max Insertion) of the four cases produced ^{239}Pu distributions that were very similar to the base case. The "Full In" case produced a greater median ^{239}Pu concentration, and also increased the overall dispersion of the distribution. In the boron and flow perturbation cases, no significant variation in ^{239}Pu distributions were observed. This is perhaps due to the limited magnitude of the perturbations that were simulated for these studies.

8.5 Future Work

This work has provided the basis for several areas that warrant further investigation. To obtain better agreement with the VVER-1000 benchmark, the NESTLE code can be improved by implementing a heterogeneous control rod model. This improvement would provide for more accurate modeling of an axially zoned the B_4C/ Dy_2O_3-TiO_3 control rod used in the VVER-1000 . Improvement of the axial reflector models by using explicit 2D reflector geometry and 2D computed ADFs should also improve agreement between the NESTLE model and the benchmark results. Although the accuracy of the pin power reconstruction features has been demonstrated, individual pins have not been independently depleted. A follow-on study of the sensitivity of the pin nuclides using the depletion interface ORIGAMI could be easily and quickly accomplished.

The NESTLE microscopic depletion model can be improved in several ways. Currently the model only contains two simple chains and two lumped fission products. This model could be expanded to include other minor actinides such as curium and neptunium along with their production and destruction mechanisms. Several important individual fission product isotopes, such as neodymium and cesium, could also be included. For the models created for this work, only one lumped fission product was used. Models that include a second lumped fission product, one that accounts for fission products that burn in quickly and saturate, would improve the

accuracy of the nuclide composition, especially early in the cycle. In some cases, the NESTLE input format only allowed for a single burnup-averaged value to be input for each nuclide. In the case of ν the average number neutrons released per fission, using a burnup and branch interpolated value rather than a single value could improve the k_{eff} agreement between the macroscopic and microscopic models. Recently a full hybrid microscopic depletion model was implemented in the code DYN3D(38). A full Integration of NESTLE with ORIGEN would allow for very detailed analysis of spent fuel nuclide composition. This could be accomplished by using the newly implemented ORIGEN API and would allow for improved subregion depletion and control rod depletion features.

Bibliography

[1] T. Bahadir, S.-Ö. Lindahl, and S. P. Palmtag, "Simulate-4 Multigroup Nodal Code with Microscopic Depletion Model," in *Proceedings of the International Conference on Mathematics and Computational Methods Applied to Nuclear Science and Engineering*, (Palais des Papes, Avignon, France), Sept. 2005. x, 10, 11, 12

[2] H. Thoburn, "Russia building nuclear reactors – and influence – around the globe," Apr. 2015. 1

[3] T. P. Makarova, B. A. Bibichev, and V. D. Domkin, "Destructive analysis of the nuclide composition of spent fuel of WWER-440, WWER-1000, and RBMK-1000 reactors," *Radiochemistry*, vol. 50, no. 4, pp. 414–426, 2008. 2, 18

[4] U. S. Department of Energy, "Supplement Analysis: Proposed Shipment of Commercial Spent Nuclear Fuel to DOE National Laboratories for Research and Development Purposes," Tech. Rep. DOE/EIS-0203-SA-07, Office of Nuclear Energy, U. S. Department of Energy, Dec. 2015. 2

[5] D. Mueller. personal communication, March 2016. 3

[6] J. Scaglione. personal communication, March 2016. 3

[7] F. Hoareau, M. Fliscounakis, D. Couyras, M. Guillo, and Y. Pora, "A Pin by Pin Microscopic Depletion Scheme using an Homogeneous Core Calculation with Pin-Power Reconstruction," in *Proceedings of ICAPP '09*, (Tokyo, Japan), May 2009. 11

[8] S. Børresen, G. Anton, A. Noel, and T. Simeonov, "SNF implementation for on-line spent fuel calculations in on-line core monitoring system GARDEL.," in *Proceddings of the 8th International Conference on WWER Fuel Performance*, (Helena, Bulgaria), Sept. 2009. 12

[9] M. D. DeHart and S. M. Bowman, "Reactor Physics Methods and Analysis Capabilities in SCALE," *Nuclear Technology*, vol. 174, pp. 196–213, 2011. 13

[10] B. Reardon, "SCALE: A Comprehensive Modeling and Simulation Suite for Nuclear Safety Analysis and Design," Tech. Rep. ORNL/TM-2005/39, Oak Ridge National Laboratory, Mar. 2011. 13, 20, 78

[11] N. Luciano, K. E. Ottinger, P. E. Collins, C. Gentry, N. George, A. J. Pawel, K. Kenner, S. Hart, O. Chvala, and G. I. Maldonado, "The NESTLE 3D Nodal Core Simulator: Modern Reactor Models," in *Proceedings of the International Conference on Mathematics and Computational Methods Applied to Nuclear Science and Engineering*, (Nashville, Tennessee, USA), Apr. 2015. 14, 21, 24, 30

[12] P. E. Collins, N. Luciano, and G. I. Maldonado, "Modernization and Expansion of Isotopic Depletion Capabilities within the NESTLE 3D Nodal Simulator," *Transactions of the American Nuclear Society*, vol. 119, pp. 1327–1329, Nov. 2013. 15, 22, 51

[13] S. Skutnik, F. Havlůj, D. Lago, and I. Gauld, "Development of an Object-Oriented Origen for Advanced Nuclear Fuel Modeling Applications," in *Proceedings of the International Conference on Mathematics and Computational Methods Applied to Nuclear Science and Engineering*, (Sun Valley, Idaho, USA), May 2013. 15, 22

[14] M. D. DeHart, "Advancements in generalized-geometry discrete ordinates transport for lattice physics calculations," in *PHYSOR-2006: American Nuclear Society's Topical Meeting on Reactor Physics - Advances in Nuclear Analysis and Simulation*, American Nuclear Society - ANS; La Grange Park (United States), Sept 2006. 16

[15] I. Gauld, N. Sly, and F. Michel-Sendis, "OECD NEA Benchmark Database of Spent Nuclear Fuel Isotopic Compositions For World Reactor Designs," in *Proceedings of PHYSOR 2014*, (Kyoto, Japan), Sept. 2014. 18

[16] F. Michel-Sendis, I. Gauld, M. Bossant, and N. Soppera, "A new oecd/nea database of nuclide compositions of spent nuclear fuel," in *Proceedings of the PHYSOR 2014 International Conference*, (Kyoto, Japan), Oct. 2014. 18

[17] T. Lötsch, V. Khalimonchuk, and A. Kuchin, "Proposal of a Benchmark for Core Burnup Calculations for a VVER-1000 Reactor Core," in *Proceedings of the 19th AER Symposium on VVER Reactor Physics and Reactor Safety*, (St. Constantine and Elena resort, Bulgaria), Sept. 2009. 18, 21, 77

[18] T. Lötsch, V. Khalimonchuk, and A. Kuchin, "Corrections and Additions to the Proposal of a Benchmark For Core Burnup Calculations for a VVER-1000 Reactor," in *Proceedings of the 20th AER Symposium on VVER Reactor Physics and Reactor Safety*, (Hanasaari, Espoo, Finland), Sept. 2010. 18, 21, 77, 92

[19] T. Lötsch, V. Khalimonchuk, and A. Kuchin, "Solutions for the Task 1 and Task 2 of the Benchmark for Core Burnup Calculations for a VVER-1000 Reactor," in *Proceedings of the 21st AER Symposium on VVER Reactor Physics and Reactor Safety*, (Dresden, Germany), Sept. 2011. 18, 21

[20] I. Ovdiienko, A. Kuchin, V. Khalimonchuk, and M. Ieremenko, "Effect of Burnup History By Moderator Density on Neutron-Physical Characteristics of WWER-1000 Core," in *Proceedings of the 8th International Safety Assurance of NPP with WWER Scientific and Technical Conference*, (Podolsk, Moscow Region, Russia), May 2013. 18, 28

[21] J. Goorley *et al.*, "Initial MCNP Release Overview - MCNP version 1.0," Tech. Rep. LA-UR-13-22934, Los Alamos National Laboratory, Mar. 2013. 20

[22] J. Leppänen, "PSG2 / Serpent a Continuous-energy Monte Carlo Reactor Physics Burnup Calculation Code. Methodology Users Manual," Tech. Rep. 1, VTT Technical Research Centre of Finland, Otaniemi, Espoo, Nov. 2015. 20

[23] J. Leppänen, "Serpent – a Continuous-energy Monte Carlo Reactor Physics Burnup Calculation Code," tech. rep., VTT Technical Research Centre of Finland, Mar. 2013. 20

[24] W. Haeck, "VESTA User's Manual - Version 2.1.0," Tech. Rep. DSU/SEC/T/2011-81, Instit de Radioprotection et de Sûreté Nucléaire, Fontenay-aux-Roses, France, Nov. 2012. 21

[25] Studsvik, "CASMO-4, A Fuel Assembly Burnup Program Methodology," Tech. Rep. Studsvik/SOA-95/2, Studsvik Scandpower, May 1995. 26

[26] S. Scandpower, "HELIOS System 1.6," tech. rep., Studsvik Scandpower AS, May 2000. 26

[27] G. I. Maldonado, "On-Line versus Off-Line Core Tracking Trends at Laguna Verde," in *Proceedings of Advances in Nuclear Fuel Management III*, (Sun Valley, Idaho, USA), May 2003. 32

[28] J. D. Galloway, *Boiling Water Reactor Core Simulation with Generalized Isotopic Inventory Tracking for Actinide Management* . PhD thesis, University of Tennessee, Knoxville, Knoxville, Tennessee, USA, Aug. 2010. 51

[29] K. E. Ottinger, P. E. Collins, N. P. Luciano, and G. I. Maldonado, "SMR Fuel Cycle Optimization and Control Rod Depletion Using NESTLE and LWROPT," in *Proceedings of Advances in Nuclear Fuel Management V*, (Hilton Head Island, South Carolina, USA), pp. 1–14, Apr. 2015. 51, 55

[30] P. J. Turinsky, "NESTLE: Few-Group Neutron Diffusion Equation Solver Utilizing The Nodal Expansion Method for Eigenvalue, Adjoint, Fixed-Source Steady-State and Transient Problems," tech. rep., North Carolina State University, July 2003. 53

[31] Z. Weiss, "A consistent definition of the number density of pseudo-isotopes," *Annals of Nuclear Energy*, vol. 17, no. 3, pp. 153–156, 1990. 60

[32] Y. A. Chao and N. Tsoulfanidis, "Conformal Mapping and Hexagonal Nodal Methods —I: Mathematical Foundation," *Nuclear Science And Engineering*, vol. 121, pp. 202–209, Oct. 1995. 73

[33] Y. A. Chao and Y. A. Shatilla, "Conformal Mapping and Hexagonal Nodal Methods —II: Implementation in the ANC-H Code," *Nuclear Science And Engineering*, vol. 121, pp. 210–225, Oct. 1995. 75, 76

[34] M. Knight, P. Hutt, and L. I, "Comparison of PANTHER Nodal Solutions in Hexagonal-z Geometry," *Nuclear Science And Engineering*, no. 121, pp. 254–263, 1995. 80

[35] S. Mittag, P. T. Petkov, and U. Grundmann, "Discontinuity factors for non-multiplying material in two-dimensional hexagonal reactor geometry," *Annals of Nuclear Energy*, vol. 30, pp. 1347–1364, Sept. 2003. 83, 85

[36] Y. Tahara, T. Kanagawa, and H. Sekimoto, "Two-Dimensional Baffle/Reflector Constants for Nodal Code in PWR Core Design," *Journal Of Nuclear Science And Technology*, vol. 37, pp. 986–995, Nov. 2000. 84

[37] E. Z. Müller, "Environment-Insensitive Equivalent Diffusion Theory Group Constants for Pressurized Water Reactor Radial Reflector Regions," *Nuclear Science And Engineering*, no. 103, pp. 359–376, 1989. 84

[38] Y. Bilodid, D. Kotlyar, E. Shwageraus, E. Fridman, and S. Kliem, "Hybrid microscopic depletion model in nodal code DYN3D," *Annals of Nuclear Energy*, vol. 92, pp. 397–406, 2016. 108

Appendix

Modifications to NEWT

The source code to the transport code NEWT was modified for two purposes. The first purpose was to output the necessary microscopic depletion homogenized and condensed cross sections and neutronic parameters. These data are computed in the subroutine *cellwt2d*. An example of the output is shown in Figure 1.

The second modification changed the tolerance of locating short lines for the *fluxplane* feature. The *fluxplane* feature allows for calculation of the average flux along a given line in the problem geometry. This change was necessary for computation of CDFs by averaging two 1 cm lines along the lattice boundary at each hexagon vertex. An example of the output is shown in Figure 2.

```
-----------------------------------------------------------------------------------------------
Nuclide              :  92235
Description          :  u235 9228 endf-7 rel0 rev7 mod7                  12/18/12
Density [atoms/b/cm] :  6.73488E-04
Mixture              :    111
Volume  [cm3]        :  1.31017E+02
Group       Flux        Absorption       Fission          Nu         Chi Prompt     Chi Delayed
-----   ------------   ------------   ------------   ------------   ------------   ------------
    1    8.55257E-02    1.24504E+01    8.45559E+00    2.44852E+00    1.00000E+00    1.00000E+00
    2    1.45448E-02    3.23889E+02    2.75424E+02    2.43670E+00    1.47361E-13    2.26559E-11
Kappa     :  3.10857E-11
     Delayed Neutron Spectrum (fission weighted)
    Group          Decay Constant Fraction
                   (Lambda, 1/s)  (Beta)
-------------------------------------------------
      1             1.24395E-02    2.18422E-04
      2             3.06362E-02    1.41988E-03
      3             1.11448E-01    1.26877E-03
      4             3.02194E-01    2.57824E-03
      5             1.17322E+00    7.57819E-04
      6             3.07480E+00    2.61072E-04
              Total Beta           0.65042E-02
     Delayed Neutron Spectrum (adjoint weighted)
    Group          Decay Constant Fraction
                   (Lambda, 1/s)  (Beta)
-------------------------------------------------
      1             1.24395E-02    2.21710E-04
      2             3.06362E-02    1.44126E-03
      3             1.11448E-01    1.28788E-03
      4             3.02194E-01    2.61706E-03
      5             1.17322E+00    7.69229E-04
      6             3.07480E+00    2.65003E-04
              Total Beta           0.66021E-02
-----------------------------------------------------------------------------------------------
```

Figure 1: Additional output from NEWT used as input for NESTLE's microscopic depletion.

```
For fluxplane n_corner_1
Line:    0.0000000000000000       13.509996299037221      -0.83571428571428852       13.027496431214463
Fraction:   0.96500007309404179
Line:  -0.83571428571428852       13.027496431214463       -1.4624999999999897       12.665621530347401
Fraction:    3.5000076427635259E-002
Sum:    1.0000001495216770
begbetwn:  T
endbetwn:  T
endpts(j)%beg:   0.83571428571428275       13.027496431214466
endpts(j)%end:    0.0000000000000000       13.509996299037221
planedata(i)%p1%x, planedata(i)%p1%y:    0.0000000000000000       13.509995999999999
planedata(i)%p2%x, planedata(i)%p2%y:   0.86602499999999993       13.009995999999999
begbetwn:  F
endbetwn:  T
endpts(j)%beg:    1.4624999999999901       12.665621530347401
endpts(j)%end:   0.83571428571428275       13.027496431214466
planedata(i)%p1%x, planedata(i)%p1%y:    0.0000000000000000       13.509995999999999
planedata(i)%p2%x, planedata(i)%p2%y:   0.86602499999999993       13.009995999999999
```

Figure 2: Additional output from NEWT showing tolerance acceptance for the *fluxplane* feature.

Vita

Nicholas Luciano is from Englewood, Florida. His interest in nuclear engineering began when he was a student assistant at the Neely Nuclear Research Center at the Georgia Institute of Technology.

After he received his B.S. in Physics from Georgia Tech, he worked as a physics associate at the Collider-Accelerator Department at Brookhaven National Laboratory. In Brookhaven's main control room, Nick operated several particle accelerators, including the Relativistic Heavy Ion Collider and the Alternating Gradient Synchrotron, two of the world's largest hadron accelerators. He was part of a team that built and tested a prototype hydrogen jet luminescence monitor for 100 GeV ion beam profile measurements. It was also in the main control room that he met his future wife, Jennifer Niedziela.

Nick left Brookhaven to join the Spallation Neutron Source at Oak Ridge National Laboratory (ORNL) staff as a control room shift supervisor. While working at SNS, he assisted the ion source group in developing a new hydrogen ion extraction and transport system. Nick began taking part-time classes in nuclear engineering at the University of Tennessee, and soon after, Jennifer moved to SNS as a graduate student in physics at UT. Soon after, both Nick and Jen left their jobs at SNS to become full-time graduate students at UT.

During his graduate studies, Nick spent a summer in Lynchburg, VA working on the mPower small modular reactor project, and worked on numerous reactor modeling projects at ORNL. Nick has accepted a full time staff position at ORNL, where he is part of the Nuclear Security Modeling Group.

Nick and Jen were married in 2012, and live in Oak Ridge Tennessee with their children.